Effects of Hydrogen Plasma Treatment on the Electronic, Optical, Mechanical and Chemical Properties of Mo, Rh, Au, HOPG and Graphene
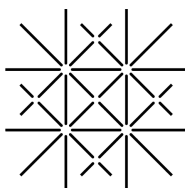
Baran Eren

aus Bursa (Republik Türkei)

Basel, 2013

UNI
BASEL

Genehmigt von der Philosophisch-Naturwissenschaftlichen Fakultät

auf Antrag von:

Dr. Laurent Marot
Prof. Dr. Martino Poggio
Prof. Dr. Ernst Meyer

Basel, den 18.06.2013

Prof. Dr. Jörg Schibler, Dekan

Abstract

Interaction of ionic and atomic species of hydrogen isotopes (protium, deuterium and tritium) with transition metals and carbon materials is an important subject of research in the condensed matter physics and material science fields. Other than the fundamental aspects of physics, the topic also has a special importance in magnetic confinement fusion and nanoelectronics applications. With the aim of providing some insight to this topic, this thesis reports experimental investigations on the electronic, optical, mechanical and chemical properties of several material systems including molybdenum/deuterium, rhodium/deuterium, gold/protium and hydrogenated layered carbon. Introduction of hydrogen into initially pure metals and onto layered carbon materials is achieved by plasma treatment.

The next generation fusion reactor (ITER) will include plasma facing, electromagnetic radiation reflecting components which will be made of either molybdenum or rhodium. Hydrogen in transition metals may act as an electron donor or an acceptor, changing the electronic band structure of its host. It can also result in increased number of lattice distortions, defect sites and inelastic scattering events reducing the optical transitions. Both directly imply that optical properties of these metals are changed. In this thesis, it is shown that deuterium acts as an electron acceptor in molybdenum, but an electron donor in rhodium. Both cases are investigated with various experimental techniques including photoelectron spectroscopy, spectroscopic ellipsometry, spectroscopic reflectometry, spectrophotometry, specific resistivity and direct surface morphology imaging techniques. Rhodium/deuterium system is not stable in air due to a catalytic reaction between deuterium and oxygen, whereas molybdenum/deuterium system is stable because deuterium is strongly bound to defect sites. In the case of molybdenum, the research is extended to investigations on the partial delamination of the coated films and kinetic roughening of the surface caused by high ion flux. Further research on thin film buckling was performed using gold coatings, where intense partial delamination from the substrate was observed even after exposure to protium plasma with a low ion flux. This mechanical deformation is attributed to high compressive stress exerted on the gold films as a result dynamic protium inventory exceeding the protium solubility of the film.

The wall materials of some of the fusion reactors currently in operation consist of graphite. Therefore, interactions of graphite with hydrogen plasma have been investigated extensively in the fusion community. A recent interest is utilizing hydrogen plasma in milder conditions for chemical modifications of graphite and graphene without chemical or physical sputtering. Hydrogenated graphite and graphene were also investigated in this thesis. It is shown with scanning probe techniques, photoelectron spectroscopy and Raman spectroscopy that hydrogenation of graphite changes its surface corrugation, valence band structure, surface electron density and vibrational modes. Moreover, it is shown that hydrogenation can be achieved locally and work function changes of the graphene surface can be mapped with Kelvin probe force microscopy.

The outcomes of the thesis are aimed to aid the fusion community in terms of material choice for the light reflecting components considered to be used in the new generation reactors, as well as the carbon community in terms of helping the comprehension of properties of hydrogenated graphene.

Contents

List of Figures

List of Tables

Introduction

This thesis is devoted to understanding of the electronic, chemical, optical and mechanical properties of transition metals such as molybdenum (Mo), rhodium (Rh) and gold (Au) and layered carbon materials treated with low temperature hydrogen plasma. Hydrogen is the first element of the periodic table, and a hydrogen atom consists of one proton and one electron. Depending on the number of neutrons, its isotopes are named protium, deuterium or tritium. In this thesis, individual name of the isotopes are specified, and 'hydrogen' is used as a generic name comprising all isotopes. Its size makes it special for surface scientists. Neither direct imaging methods such as atomic force microscopy nor surface techniques such as photoemission spectroscopy are sensitive enough for its detection. So far, it can only detected by bulk techniques such as nuclear magnetic resonance, secondary ion beam spectroscopy, etc., without spatial nanometer resolution. As surface scientists, this is not enough for us. Though we cannot detect hydrogen directly, we can detect its effects when it is in or on the host material.

Low energy hydrogen molecules can have different interactions with the substrate such as adsorption onto the surface, reaction with the surface or diffusion on the surface. Once dissociated by the surface energy, it can diffuse into the bulk. Though these processes may still occur for higher energy atoms and ions, other processes such as implantation, sputtering, backscattering and secondary electron emission also have to be taken into account. Plasma material interactions are an interplay of all these processes. Within the depth where the impinging ions lose their initial energy, the characterized material which was treated with hydrogen plasma is a different material from before. In this respect, it is reasonable to extend the scope of this thesis from 'surface science' to 'surface and subsurface science'. In terms of the electronic band structure of transition metals, the thesis provides three different examples where hydrogen atoms play a role either as an electron donor or acceptor, or have no charge exchange at all. In terms of mechanical changes of the surface of transition metals, the manuscript provides examples of different phenomena such as thin film delamination, blistering, kinetic roughening, or the surface remaining unaltered under energy deposition. Changes in the optical properties are dependent on the changes of the electronic and mechanical properties. In terms of chemical changes, the thesis presents reactions of protium plasma with layered carbon materials and shows how the distribution of surface electrons and surface chemistry are affected by these changes.

The thesis consists of three parts. The first part consists of Chapters 1 and 2, in which the necessary theoretical notions and experimental details are briefly presented. The last two sections of Chapter 2 contain the author's own interpretation of the reflectivity of nanocrystalline coatings.

The second part of this thesis consists of Chapters 3 to 7. The subjects of these chapters are transition metal/hydrogen system.

ITER is the next generation fusion reactor project, which is currently under construction in Cadarache in the south of France. The aim of the project is to build the largest experimental tokamak (toroidal chamber with axial magnetic field, original abbreviation from Russian) nuclear fusion reactor in the world [1]. Current reactors under operation have optical diagnostic systems which can view the plasma directly or through optical fibers, which will not be possible for ITER due to the high level of neutron radiation expected. Therefore, metallic mirrors are foreseen to play a key role in guiding the plasma light towards the optical diagnostics. As those mirrors directly viewing the plasma, the so-called first mirrors (FMs), will be subject to a harsh environment of particle fluxes due to charge exchange neutrals and neutrons, as well as UV, x-ray and gamma radiation, their performance will be a critical issue for the operation of all optical diagnostics [2–4]. More detailed information about magnetic confinement fusion, the ITER project and the first mirror problem can be found in the PhD thesis of Gregory de Temmerman at the University of Basel [5].

ITER plasma will contain deuterium and tritium, together fusion by-products (e.g. helium) and impurities sputtered from the wall materials (tungsten (W), beryllium (Be) and possibly carbon (C)). Of course, the most abundant element in the ITER plasma will be deuterium, which is in the limelight of this thesis.

Thanks to its robustness against deuterium plasma exposure (low physical sputtering yield [6], no binary compound with hydrogen reported) and acceptable reflectivity in the UV/VIS/NIR region [7], Mo is an important candidate for FMs. The critical issue is to keep the surface relief pattern (i.e. the roughness of the mirror surface) small in comparison to the wavelength of the reflected light in order to have negligible diffuse reflectivity. Single crystal mirrors may suffice these conditions; however, technological difficulties of producing large size Mo crystals limit their use. Polycrystalline mirrors are not an alternative due their poor performance (blistering, roughening due to different sputtering rates for different crystal orientations [8]) under deuterium plasma or neutral exposure [9]. Due to these facts, Mo coatings are being considered as a potential alternative to Mo single crystals. Such coatings are called nanocrystalline, since they consist of homogeneously dispersed crystals with different orientations in the nanometric range. The coating itself does not have a preferred orientation. It is shown in Chapter 2 (and in [10]), that magnetron sputtered films exhibited reflectivity comparable to bulk Mo [7]. After exposure in a tokamak under erosion conditions, these mirrors showed reflectivity very similar to single crystalline mirrors [11].

Erosion of plasma facing components will cause impurities such as W, Be and C to enter the ITER plasma, which may form deposits on FMs. Depending on the local plasma parameters, the first mirrors may be subject either to net erosion or net deposition. FMs in net deposition zones will also see a certain amount of initial erosion during the first ITER shots, before a deposit has built up on the surface. Moreover, deuterium plasma exposure is currently foreseen as a possible cleaning technique to remove deposited layers from the FMs, which will cause erosion of the mirror surface as well [12]. Consequently, understanding the effects of pure deuterium plasma on the reflectivity of Mo, one of the candidate materials for the FMs, is essential before considering additional effects from other impurities. In order to investigate the behavior of magnetron sputtered coated Mo mirrors under deuterium plasma exposure, under conditions expected to occur in ITER either during plasma operation or cleaning, these conditions are simulated experimentally and their altered optical properties are characterized. The results are presented in Chapter 3 (and in [13]).

The nanocrystalline Mo coatings are exposed to high flux deuterium plasma in order to test their roughening limits and reflection performance under strong erosion conditions. The results are presented in Chapter 4 (and in [14]). It is shown that when the mirrors were kept at a surface temperature below 100 °C during exposure, the coatings partially delaminate from the substrate. This is not the case for the samples tested at 200 °C, for which the energy dependence of the roughening dynamics are explained. The reflectivity performance of these mirrors are compared with the results of Chapter 3 and with the results obtained from another exposure campaign.

Rh is another important candidate material for the first mirrors due to its good reflectivity (>70-80%) in the whole UV/VIS/NIR range [7], its acceptably low sputtering yield [6], and its low reactivity with oxygen, C and W. Due to the technological difficulties of production of large size single crystals and due to the very high cost of Rh as a raw material, thick film coatings are considered to be used for the FMs in ITER. Nanocrystalline coatings produced by magnetron sputtering fulfill these requirements [15, 16], and they exhibit handbook reflectivity for the UV/VIS/NIR range [7]. In Chapter 5 (and in [17]), the evolution of the reflectivity of Rh coatings during deuterium plasma exposure is addressed.

After giving special attention to understand how Mo and Rh surfaces would behave during pure deuterium plasma exposure, the research is extended to include impurities such as W, Be and C to enter the plasma. Aluminum (Al) was employed as a replacement for Be due to the chemical similarities between these two metals, since the toxicity of Be precludes its use at the University of Basel. Several possible plasma mixtures relevant to ITER, which include W-C and W-Al impurities, are experimentally simulated while monitoring the *in situ* reflectivity of the mirrors. The aim is to experimentally simulate the effects of such impurities on the chemical composition of the mirror surface, and on the reflectivity accordingly. The results are presented in Chapter 6 (and in [18]).

In Chapter 7 (and in [19]), the attention was the buckling of the gold films during protium plasma exposure. Gold is chosen as an example because it does not hydrogenate (therefore has a low protium solubility) and has a low Young's modulus; thus can buckle easily. This is a dangerous situation for hydrogen plasma treatment of thin and thick films in general, which may result in their catastrophic failure. The buckling of the film is attributed to dynamic protium inventory exceeding the protium solubility of gold, subsequently building a compressive stress due to over-pressurized protium gas trapped in the film.

The wall materials of some of the fusion reactors currently in operation consist of graphite. Therefore, interactions of graphite with hydrogen plasma have been investigated extensively in the fusion community. A recent interest is using hydrogen plasma for chemically modifying layered carbon materials, which the last part of this thesis (Chapters 8 and 9) deals with.

Being an sp^2-hybridized single layer of carbon atoms arranged in a densely packed honeycomb lattice with a true atomic thickness, graphene possesses unusual electronic and mechanical properties [20, 21]. A new perspective is the chemical modification of graphene, especially the incisive idea of attaching atomic protium to both sides of the graphene lattice to produce graphane; an sp^3-hybridized insulating derivative of graphene [22–25]. The achievement of Chapter 8 (and [26]) is to use protium plasma for attaching protium on both sides of the graphene layers. The obtained material is characterized using various surface science techniques, showing that the graphene layers do indeed hydrogenate.

In Chapter 9 (and in [27]), the research in Chapter 8 is extended to the investigation of

graphene supported on a Si/SiO$_2$ substrate. A decrease of 60 meV in the work function of graphene is reported as a result of hydrogenation. It is also shown that stencil masks can be used to obtain hydrogenated/pristine graphene patterns, which is possible to image with Raman microscopy and Kelvin force probe microscopy.

The thesis work has offered 8 articles [10, 13, 14, 17–19, 26, 27] to the scientific community under the first and corresponding authorship of Baran Eren. Please cite these articles instead of the thesis.

Enjoy reading this thesis!

Chapter 1

Theoretical background

This chapter provides a brief summary of the necessary theoretical background for the interpretation of the experimental results in the following chapters. Within the scope of this thesis, the explanations are kept short and qualitative; formulas, when available, are presented as the final equations without any derivations. The explained concepts are as follows: Interactions between plasma and solid surfaces, optical reflectivity of metals, effects of hydrogen implantion into a transition metal, and effects of hydrogen bound to layered carbon materials. The chapter renders service to the reader in terms of providing foreknowledge about hydrogen plasma treated transition metals and layered carbon materials.

1.1 Important plasma material interactions

The scope of this thesis covers materials treated with plasma to a great extent. Therefore, a review of the plasma material interactions is summarized in this section. The plasma material interactions can be categorized into three groups with respect to the energy of the plasma particles as illustrated in Figure 1.1. However, a few words about the plasma itself have to said before starting explaining its interaction with solid surfaces.

1.1.1 A few words about low temperature plasma

Plasmas are quasi-neutral particle systems and they are fluid-like mixtures of free electrons and ions together with neutral particles (atoms, molecules) [28]. The charge carriers and their electromagnetic interactions have a substantial effect on the system properties. There are two aspects of the interactions between the plasma components and the electric charges. The first one is Coulomb interactions among charge carriers, which is each charge carrier interacting simultaneously with many others. The second one is the formation of macroscopic space charges as a consequence of external influences (e.g. due to thermal movement). The most intrinsic attribute of plasma is minimization of external electric and magnetic fields inside its bulk. Plasmas may be divided into two groups as low and high temperature plasmas. A further subdivision among low temperature plasmas can be made as thermal and non-thermal plasmas. The type of plasma used in this thesis is non-thermal low temperature plasma (LTP) with the conditions: $T_i \sim T \sim 300$ K; $T_e \geq 10^5$ K; low-pressure. T_i, T_e, and T denote the ion temperature, electron temperature and gas temperature, respectively. The most important component of

non-thermal LTP is the hot electron gas. The production of ionized, excited and dissociated species with increased chemical activity and the generation of electromagnetic radiation lines and continua are results of these electrons with high kinetic energies. The occurrence of the charge carriers in plasma results in the following: 1- Occurrence of electrical conductivity 2- Interaction with magnetic fields 3- Occurrence of a multitude of oscillations and waves 4- Screening of the electric fields and 5- Formation of characteristic boundary sheaths at the plasma material contacts [28].

1.1.2   Low energy interactions

Some of the interactions with the surface do not require high energy and can also occur in the gas phase. For instance, hydrogen molecules can get dissociated due to the surface energy and can be chemically adsorbed (chemisorbed on the surface). Alternatively, they can stay molecular and can be weakly bound (e.g. via van der Waals interactions) to the surface, which is then called physisorption. For metals, physisorption can be understood as the interaction between the particle and its virtual image in the metal, whereas chemisorption happens via electron donation from the conduction band [29, 30]. Adsorbed species can diffuse on the surface, into the surface or can be desorbed back into the vacuum or gas.
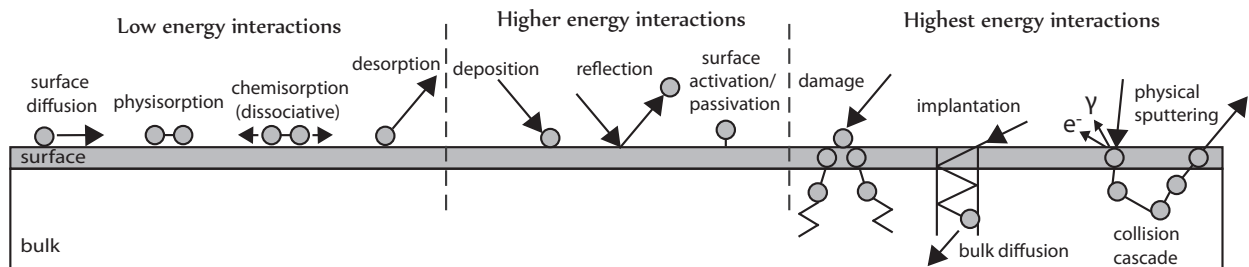
Figure 1.1: Illustration of the interaction of plasma with a material surface and subsurface.

1.1.3   Higher energy interactions

If the energy of a particle is too low for implantation or physical sputtering and too high for the adsorption processes, or if it has no suitable surface site available, it will get reflected from the surface [28]. The probability of reflection is often expressed with the reflection coefficient, which is also dependent on the temperature.

An impinging particle can also create dangling bonds or react with the existing dangling bonds, which are called surface activation and surface passivation, respectively.

1.1.4   Highest energy interactions

The interaction of energetic ions and atoms with a nonreactive surface can be modeled with the binary collision model, in which one binary collision event is considered at each instant. In this thesis (and in the vast majority of theoretical explanations), the classical approach based on conservation of momentum and energy is sufficient. For each binary collision, the amount of energy and momentum transfer will depend on parameters such as the impact parameter or the

scattering angle. Projectile ions or atoms which are not reflected will either be implanted into the subsurface or will get deposited on the surface. In this subsection, brief descriptions of these processes are provided. However, electron emission processes are not relevant to this thesis and, therefore, are skipped.

Implantation

An energetic atom or an ion will be implanted until it loses all its initial power. The specific energy loss per distance is described as the stopping power (S(E)=dE/dz) and it is based on continuous-slowing-down approximation [31, 32]. If the initial energy of the impinging particle is low, this approximation may not hold (no implantation). There are two mechanisms which constitute the stopping power, namely the nuclear stopping power and the electronic stopping power. The nuclear stopping power simply results from the scattering between two nuclei, in which displacements of the atoms, the momentum and the energy transfers are large. It can be calculated from the Rutherford scattering cross section [33]. The electronic stopping power, on the other hand, originates from the interactions between the electrons of the solid and the impinging particle, and it may be calculated from quantum mechanical theory [31, 34].

Physical sputtering

Physical sputtering is the removal of surface atoms as a consequence of energy and momentum transfer from an impinging atom to a surface atom, which initiates a collision cascade among the lattice atoms [33, 35, 36]. If as a result of such a collision cascade, a surface atom receives sufficient energy to overcome its surface binding energy, the atom may leave the surface. The sputtered atom is most likely another atom than the one which was subjected to the initial impact. An often used term is the sputtering yield, which is the number of atoms ejected from the surface per incident particle. Since the sputtering process depends on the surface binding energy, it is a threshold processes, meaning that no sputtering takes place below a threshold value that can be approximated by momentum transfer equations [37]. Sputtering yields for incident and target atom combinations are tabulated in various references [6, 38, 39]. The sputtering yield is also dependent on the incident angle [40], surface roughness [41] and the crystallographic orientation [42]. Kinetic roughening dynamics of metals during physical sputtering are discussed in more detail in Chapter 4.

Physical sputtering by molecular ions

As previously mentioned, an energetic ion impinging on a surface deposits its energy in the near surface region and sets up a cascade of recoiling target atoms, while part of this deposited energy results in ejection of some surface atoms. A more complex process occurs if the impinging particles are molecular ions. In this case, the molecular ion dissociates into its constituent atoms upon impact with the surface, each fraction receiving a kinetic energy proportional to its mass (e.g. energy deposition by the A atom of an AB^+ ion would be $E_A = E[M_A/M_A + M_B]$, where M is the atomic mass and E is energy) [43].

Chemical sputtering

Another pathway for sputtering is a chemical reaction taking place between the surface and the incoming radiation (electrons, ions, photons) which subsequently leads to the desorption of surface atoms [44]. This process is called chemical sputtering and is either the result of volatile molecule creation, or precursor creation with a lowered physical sputtering threshold. This process is outside the scope of this thesis.

1.1.5   Blister formation

Hydrogen induced blistering is typical of polycrystalline metals, where implanted ions diffuse through the grain boundaries and get stuck at a grain boundary between two lateral crystals, resulting in deformation of these crystals [45, 46].

There is another phenomenon, which also results in blistering and it is typical of thin film coatings. When the compressive stress in the film is over a certain threshold value, the film starts to buckle in order to relieve its stress. This may happen due to coating process itself, or alternatively may be induced by excess hydrogen implantation into the film. Previous works on the buckling of thin films as a result of hydrogen loading were performed on hydrogenating materials [47–49], whereas Chapter 7 discusses same phenomenon for a non-hydrogenating metal.

1.2   Reflectivity of metallic solids

A certain fraction of an electromagnetic (EM) radiation reflects when it encounters a material interface. What is being reflected can be quantized either as the reflected electric field (amplitude reflectivity or complex reflection coefficient) or as the reflected electromagnetic power (power reflectivity, reflection coefficient or just reflectivity), the latter being square of the magnitude of the former. Reflectivity is terminologically distinguished from the reflectance, as it applies only to the reflecting media which is 'thick' enough, whereas reflectance is a generic name. Physical notions related to the reflectivity have to be clarified before discussing possible effects of hydrogen plasma treatment on the reflectivity of metals.

The reflectivity of an interface between vacuum (or air) and a semi-infinite (or 'thick' enough) isotropic medium is given by the Fresnel equations [50]:

$$R_s(\omega, \phi) = \left(\frac{cos(\phi) - \sqrt{\epsilon(\omega) - sin^2(\phi)}}{cos(\phi) + \sqrt{\epsilon(\omega) - sin^2(\phi)}} \right)^2, \tag{1.1a}$$

$$R_p(\omega, \phi) = \left(\frac{\epsilon(\omega)cos(\phi) - \sqrt{\epsilon(\omega) - sin^2(\phi)}}{\epsilon(\omega)cos(\phi) + \sqrt{\epsilon(\omega) - sin^2(\phi)}} \right)^2 \tag{1.1b}$$

where $R_s(\omega, \phi)$ and $R_p(\omega, \phi)$ represent the perpendicular and parallel reflection coefficients and $\epsilon(\omega)$ is the complex permittivity of the metal. In a solid, typical interatomic distances are on the order of an Ångström, which corresponds to EM radiation in the x-ray energy domain. This makes it possible to explain the response of a metal to an EM field in the optical (UV/VIS/NIR) range with the classical model. In this model, the bound electrons and lattice oscillate around their equilibrium point when subjected to an external EM field. They can be modeled with a damped harmonic (Lorentz) oscillator with j modes. In the quantum mechanical approach,

this formulation corresponds to interband processes which are electron transitions from occupied states to higher energy unoccupied states upon absorption of a photon by an electron in the occupied state. In addition to these, there are also intraband (free carrier, Drude) processes with no spring constant. The dielectric function is addition of these two terms [51]:

$$\epsilon(\omega) = \epsilon_{Lorentz}(\omega) + \epsilon_{Drude}(\omega), \tag{1.2a}$$

$$\epsilon_{Lorentz}(\omega) = \epsilon_0 \left(1 + \sum_j \frac{\omega_{pj}^2}{\omega_{0j}^2 - \omega^2 - i\beta_j\omega}\right), \tag{1.2b}$$

$$\epsilon_{Drude}(\omega) = \epsilon_0 \left(1 - \frac{\omega_p^2 \tau_D^2}{1 + \omega^2 \tau_D^2} + i\frac{\omega_p^2 \tau_D}{\omega(1 + \omega^2 \tau_D^2)}\right) \tag{1.2c}$$

where in Eq. 1.2b ω is the angular velocity of the acting EM field (e.g. visible light), ω_{pj} is the plasma frequency, ω_{0j} is the eigenfrequency of damped simple harmonic oscillator and β_j is the damping factor. Eq. 1.2c is deduced from Eq. 1.2b with $\omega_{0j}=0$, j=1 and $1/\tau_D = \beta$. τ_D is the intraband relaxation time and the probability of an electron undergoing a collision per unit time is $1/\tau_D$.

For simplicity, let me only emphasize on the Drude term for investigating R(ω, ϕ). τ_D can be written in terms of all the scattering mechanisms available:

$$\tau_D^{-1} = \tau_b^{-1} + \tau_{di}^{-1} + \tau_s^{-1} + \tau_{sr}^{-1} + \tau_{gb}^{-1} + ... \tag{1.3}$$

where the subscripts b, di, s, sr, and gb represent anisotropic background scattering (scattering due to phonons and point defects), defect and impurity scattering, surface scattering, surface roughness scattering and grain/crystallite boundary scattering, respectively. In other words, increase of surface or subsurface scatter events in a solid results in a decrease of its reflectivity. Changes in the electronic band structure (the classical analogy is $\epsilon_{\text{Lorentz}}$) result in further changes in the reflectivity.

For the rest of thesis, reflectivity will refer to the reflectivity at the normal incidence unless the angle is explicitly specified.

1.2.1 Two components of the reflectivity

The total reflectivity of an EM radiation at the interface between two semi-infinite media can be broken into two components, which are the specular (mirror-like) reflectivity and the diffuse reflectivity. As depicted in Figure 1.2, specular reflectivity is the ability of an interface to reflect an EM radiation with a single direction to another single direction, in such a way that these two directions are on the same plane and they have the same angle with respect to the surface normal. Diffuse reflectivity is the reflected light which is not specular. Diffusely reflected light has a certain angular distribution, the term Lambertian referring to the case where it is uniform in all directions. Specular and diffuse reflectivity are simply the percentage ratio of the intensity of the specularly or diffusely reflected light to the intensity of the incident beam. These definitions are valid for reflectivity at all incident angles, but the percentages may be different.

$$R_{total} = R_{specular} + R_{diffuse} \tag{1.4}$$
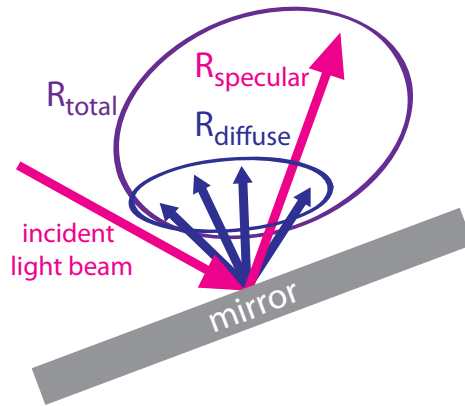
Figure 1.2: The total reflectivity is the sum of the specular and the diffuse reflectivity.

A possible (but not the only) reason of the diffuse reflectivity is the surface roughness. A formulation between the reflectivity at the normal incidence and the roughness for a semi-infinite metal/vacuum interface was suggested in the 50s by Bennett [52], in which the diffuse reflectivity exponentially increases with increasing roughness.

$$R_{specular}(\lambda) = R_0(\lambda)e^{-(4\pi r_{rms})^2/\lambda^2} \tag{1.5}$$

where λ is the wavelength of the light, R_0 is the reflectivity from a perfectly smooth surface and r_{rms} is the root mean square roughness. However, it should always be kept in mind that there are other scattering mechanisms which can contribute to the diffuse reflectivity.

1.3   Hydrogen in transition metals

The first general topic of this thesis is the optical response of transition metals to deuterium LTP exposure. After introduction of plasma material interactions and reflectivity of metallic solids, a few words have to be said about metal/hydrogen systems, which the reader will come across frequently in Chapters 3 to 7.

As mentioned previously, materials treated with hydrogen plasma will contain some amount of hydrogen as a result of implantation and bulk diffusion. In terms of electronic transfer, it is possible to advocate four different simple models when considering a transition metal/hydrogen system [53, 54]: (i) Electrons from hydrogen can fill the unoccupied states in the d band of the metal. (ii) Hydrogen can accept electrons from the metal. (iii) No charge transfer between the metal and hydrogen occurs. (iv) Metal and hydrogen can be covalently bonded. The first two mechanisms and their effects on the reflectivity are thoroughly discussed in Chapters 3 and 5 for molybdenum and rhodium, respectively.

Electron transfer between metal and hydrogen makes valence level and core level photoelectron spectroscopy techniques uniquely qualified for understanding the effects of hydrogen in the electronic band structure of transition metals (photoelectron spectroscopy is explained in detail in Chapter 2). However, care has to be taken during the evaluation process because the measured spectra include different factors such as Fermi Level shifts, Coulomb screening, core photoionization and relaxation, final state effects, etc. Changes in the electronic structure of the

metal directly imply that its optical properties are also changed. Moreover, hydrogen induced states may also form, but these are out of the scope of this thesis.

1.4 Hydrogen on layered carbon materials

The second general topic of this thesis is hydrogenation of layered carbon materials as a result of protium plasma treatment (Chapters 8 and 9). Layered carbon materials are graphene and graphite, the first one being the monolayer version of the second one. Graphene is a pure carbon material with a two dimensional honeycomb lattice structure, whereas graphite consists of graphene layers stacked in the AB form (π-stacking).

Hydrocarbons are molecules with a carbon backbone on which hydrogen atoms are covalently bonded to them. They are the simplest organic compounds. A new approach since 2007 is the investigation of the hypothetical material 'graphane', where hydrogen is attached on both sides of a graphene layer in such a way that hydrogen to carbon ratio is 1:1 [22]. This extended two dimensional covalently bonded hydrocarbon is expected to have different characteristics than its dehydrogenated counterpart, graphene, such as having a 3.5 eV bandgap. It also has an sp^3-hybridization and a binding energy of 6.56 eV/atom which makes it very stable. Contrary to the theoretical expectations, the experimental results so far have resulted in dehydrogenation at temperatures as low as 400-450 °C and only a $T^{1/3}$ dependence of the hole mobility instead of a clear bandgap generation [24,55]. On the other hand, the Raman spectroscopy (phononics) results support hydrogenation, and is so far the most efficient method for the detection of strong atomic rearrangements due to sp^3-hybridization [24,56]. The $T^{1/3}$ dependence of the mobility is a result of carrier hopping conduction due to the defect states lying in the theoretical bandgap, implying that bandgap generation can be practically impossible. In this respect, investigating graphite surface may be more informative, since the defect density is much less than the isolated monolayers supported on insulating materials.

Chapter 2

Experimental

This chapter summarizes the preparation and characterization methods used throughout the thesis. It also provides an introduction to the theory of the coating process (specifically physical vapor deposition) and briefly explains the magnetron sputtering technique. Finally, it gives an example of Mo and Rh coatings with their structural and optical properties.

2.1 Characterization methods and devices

2.1.1 Photoelectron spectroscopy

Photoelectron spectroscopy exploits the landmark discovery of photoemission by Einstein in 1905 [57]. The photons of radiation which are incident on a sample surface excite electrons in the subsurface of the sample, which are then emitted if the photon energy is higher than the work function (WF) of the sample surface. X-ray [58] and ultraviolet photoelectron spectroscopy (XPS, UPS), which are used in Chapters 3, 4, 5, 6 and 8, use an electrostatic analyzer to determine the kinetic energy of the emitted electrons. A very detailed theoretical explanation can be found in Ref. [59].

The simplest picture of the photoemission process is the so-called 'three step model' proposed between 1940 and 1960. The energy diagram is depicted in Figure 2.1 for one quasi-free electron [60–63]. The first step is the optical excitation of an electron with a differential cross section $d\sigma/d\Omega$ (the cross section for a collision process, which results in the emission of particles (e.g. electrons, photons) at a specified angle relative to the direction of the incident particles, per unit angle). The second step is the transport to the surface, where the electron inelasticly and elasticly scatters. The intensity of inelastic scattered electrons scales as: $I(z)=I_0\exp(-z/\Lambda_e\sin(\theta))$, where Λ_e is the inelastic mean free path of an electron, which is a function of E_{kinetic} [64] and θ is the grazing angle. This enables surface enhancement at grazing exit angles. The last step is the escape into vacuum, which requires the surface potential barrier (V_0) to be surmounted. The energy diagram in Figure 2.1 leads to the following equation [59, 66]:

$$h\nu = E_{\text{binding}}^{\text{Vacuum}} + E_{\text{kinetic}} = E_{\text{binding}}^{\text{Fermi}} + \Phi_{\text{spectrometer}} + E_{\text{kinetic}} \tag{2.1}$$

where E_{kinetic} is the measured quantity, $\Phi_{\text{spectrometer}}$ is given; thus $E_{\text{binding}}^{\text{Fermi}}$ can be easily obtained. Fermi level (E_f) will be fixed 0 eV, $E_{\text{binding}}^{\text{Fermi}}$ will be referred as the binding energy (B.E.) and will be expressed with positive values for the rest of this thesis.
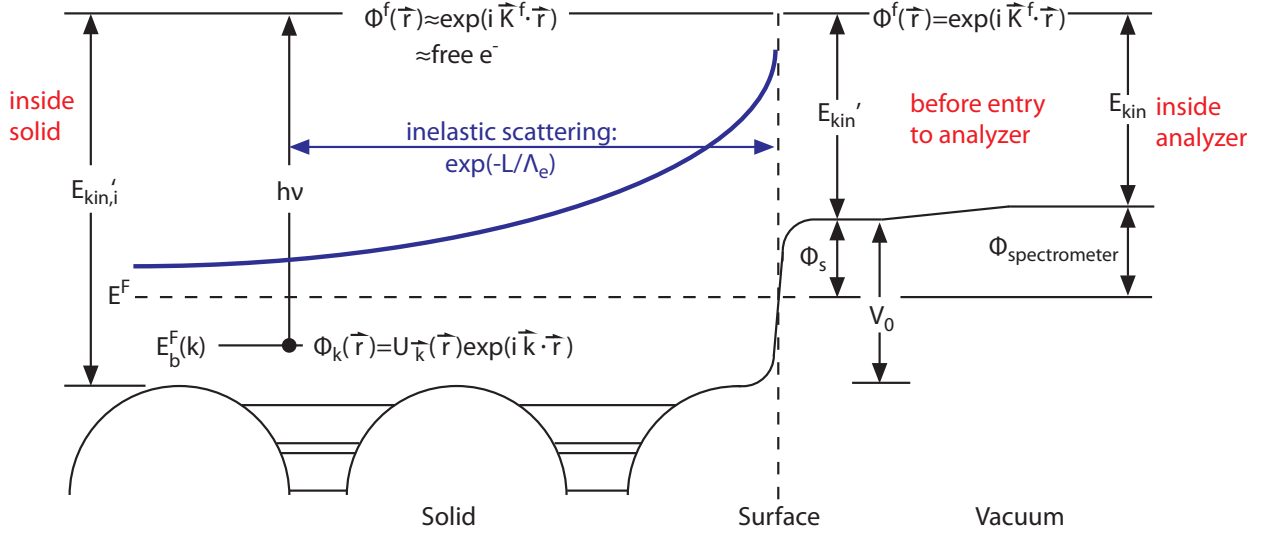
Figure 2.1: One-electron picture of the photoemission process inside a solid surface. The model is based on [65].

Within the borders of the three step mode, the intensity of a core level spectrum of a subshell Qnlj can be expressed with the following equation:

$$I(Qnl\text{j}) = C \int_0^\infty I_{h\nu}(x,y,z) \rho_Q(x,y,z) \frac{\mathrm{d}\sigma_{Qnlj}(h\nu)}{\mathrm{d}\Omega} exp\left[-\frac{z}{\Lambda_e(E_{\text{kinetic}})sin(\theta)}\right] \Omega_{E_{\text{kinetic}},x,y} \mathrm{d}x\mathrm{d}y\mathrm{d}z \tag{2.2}$$

where $I_{h\nu}(x,y,z)$ is the x-ray flux,

$\rho_Q(x,y,z)$ is the density of atoms (Q refers to quantitative analysis),

$\frac{\mathrm{d}\sigma_{Qnlj}(h\nu)}{\mathrm{d}\Omega}$ is the energy dependent differential photoelectric cross section for subshell Qnlj,

$\Lambda_e(E_{\text{kinetic}})$ is the energy dependent inelastic attenuation length,

and $\Omega_{E_{\text{kinetic}},x,y}$ spectrometer acceptance solid angle.

For the valence band intensity, $\rho_Q(x,y,z)$ term has to be replaced by $\rho_{Qnl}(E_{\text{binding}},x,y,z)$ which is the density of states (DOS) projected onto Qnl character. In reality there are many electrons in the system, which require screening/relaxation effects and final state effects due to core level photoionization to be included in the energetics. A typical example is so-called the 'chemical shift' in the core level peaks are a result of electron transfer (or donation) to another element, in which the Coulomb attraction of a core electron to its positive nucleus increases as a result of less screening from outermost electrons [67].

A real photoemission spectrum broadens due to analyzer sensitivity and resolution. More-

over, there is always a background which consists of the smooth contributions (related to photo-electrons with higher kinetic energies) and reconstructed contributions (e.g. plasmon excitations, interband transitions, Auger electrons).

The lateral resolution of the method is limited with the spot size of the beam. The spot sizes used in this thesis are macroscopic; thus the results are averaged over a large area. Since Λ_e depends on the kinetic energy of the electrons, the information depth is different for different materials for the fixed energy radiation sources used in this thesis, introducing a certain amount of error to the concentration analyses. A variable radiation source (e.g. synchrotron) is necessary for an accurate concentration analysis at a specific depth. The information depth obtained from photoelectron spectroscopy using x-ray tubes typically does not exceed 5 nm, whereas UPS is sensitive to the first few atomic layers of the surface.

XPS fitting procedure

Fitting of the core level lines was performed using Doniach-Sunjic (asymmetrical Lorentzian) functions [68], with a Shirley background substraction [69], using UNIFIT for Windows (Version 2008 and 2011) software [70]. A convolution of an asymmetry function, Lorentzian and Gaussian line shapes was used to fit the individual peaks. After this, the intensities were estimated by calculating the integral of each peak; the atomic concentrations were then derived using Scofield sensitivity factors [71].

2.1.2   Scanning probe techniques

Atomic force microscopy

An atomic force microscopy (AFM), in its simplest picture, is a cantilever, where the free end has a tip which is being scanned over a sample surface [72]. The choice of the cantilever material depends on the desired function of the device. In this thesis, silicon cantilevers with sharp tips (radius of curvature on the order of nanometers) were used. Some of the cantilevers were coated with platinum/iridium (Pt/Ir) alloy. The choice of the cantilever is specified in the individual chapters. When the tip is in the vicinity of the sample surface, different forces such as electrostatic, van der Waals, dipole-dipole, etc. can act on the tip which results in the deflection of the cantilever. For the measurements in this thesis, Nanosurf Mobile S and Nanosurf FlexAFM microscopes were used, which both detect the beam deflection with an array of photodiodes (Figure 2.2) [73]. Finally, a feedback loop has to be provided in order to keep the force between the sample and the tip constant by adjusting the z-distance (with piezo crystals) during scanning [74].

The measurements in this thesis were performed in ambient conditions and usually in air. A liquid wetting layer is typical in such conditions, and in order to cope with this problem intermittent contact mode was used in this thesis [75]. In this mode, the cantilever is oscillated externally close to its fundamental resonance frequency ($\omega_{\text{osc}} \approx \omega_0$) with a constant amplitude A_{ext} and constant phase Φ_1. The interactions between the tip and the sample surface would result in a decrease of the oscillation amplitude as the tip approaches to the surface until the set point amplitude A_{sp} is reached. Similar to above, the z-distance is adjusted with a feedback loop to keep A_{sp} constant. The topography image is these adjustments in the z-distance during scanning while the phase image is the difference between the reference phase Φ_1 and the actual phase $\Phi_0(t)$.
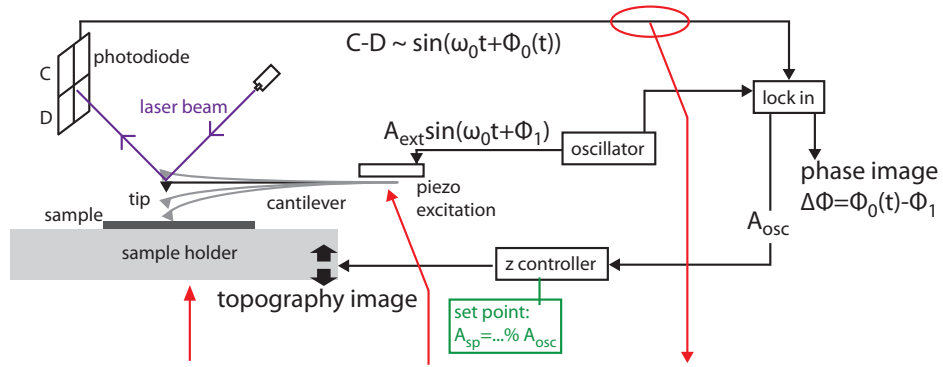
Figure 2.2: Feedback loop of an AFM in amplitude modulated intermittent contact mode. Red arrows indicate the additional connections necessary (Figure 2.3) when contact potential difference image is also desired in addition to topography and phase images.

Kelvin probe force microscopy

WF of a solid is defined as the minimum energy required to remove an electron inside the bulk of a solid into the vacuum immediately outside of the solid, which can be formulated as $WF=E_{vacuum}-E_f$. Secondary electron cut-off energy of a UPS spectrum is a very efficient method of extracting WF of a solid. However, this method averages WF all over the UV light spot area on the surface. Kelvin probe force microscopy (KPFM) method combines the Kelvin principle [76] with AFM and enables local WF measurements [77, 78]. In this thesis, KPFM measurements were performed in Chapter 9, after making the necessary connections shown in Figure 2.3.
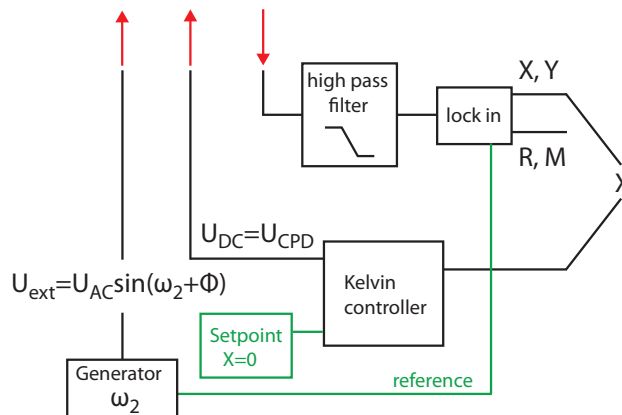
Figure 2.3: Feedback loop of a KPFM in amplitude modulated intermittent contact mode. Red arrows indicate the connections to Figure 2.2.

2.1.3   Optical techniques

Spectroscopic ellipsometry

An incident plane-polarized light beam which is reflected at an interface between two semi-infinite media at some oblique angle becomes elliptically polarized. An ellipsometer, which was invented in 1945 [79], measures the change in the polarization state of light which is related to the optical properties of the media [80]. The actual quantity being measured is the complex reflectance ratio ρ_{ref}=r_p/r_s, where r_p and r_s are the parallel and perpendicular polarized complex reflection coefficients. ρ_{ref} is parameterized to the relative attenuation and to the phase shift as ρ_{ref}=$\tan(\psi)\exp(i\Delta)$. Ideally, an optical model and an iterative fitting procedure have to be employed after the measurement in order to extract the optical properties of the material from the Ψ and Δ data set [81,82]. In this work, ellipsometry is used in Chapter 3 in order to extract the optical constants of deuterium plasma treated Mo. A mathematical interval fit and one layer model is used for simplicity, which turned out to work very well since the calculated reflectivity change was measured almost the same as it is measured by the spectrophotometer.

Spectroscopic ellipsometery measurements were done in variable angle configuration using a Sentech 850 device at incident angles of $45\,^\circ$, $55\,^\circ$ and $65\,^\circ$ for a wavelength range of 300-2300 nm.

Spectrophotometry

Absolute total and diffuse reflectivity measurements were performed with a Varian Cary-5 UV/VIS/IR spectrophotometer for a wavelength range of 250 to 2500 nm. The first principle of measuring an absolute reflectivity of a sample is having reference measurements with a calibrated poly tetra fluoroethylene (PTFE) sample, which has a reflectivity close to 100% for the whole wavelength range mentioned [83]. The spectrophotometer is equipped with a 110 mm diameter integrating sphere (Ulbricht's sphere) which is also coated with PTFE, and is assumed to have a perfect Lambertian diffuse reflectivity. Two geometrical configurations are possible: In the first one, the incident angle of the light beam on the sample is $\approx 3\,^\circ$, and the reflected light is collected by the inner wall of the integrating sphere. This measurement is used for the total reflectivity measurements. For diffuse reflectivity measurements, the light beam has a normal incidence; hence specular reflected photons are not collected by the integrating sphere. Both for the total and diffuse reflectivity measurements, a reference measurement with the PTFE sample and a background intensity measurement have to be performed separately, the latter obtained simply by blocking the light path during the measurement. Finally, after measuring the reflectance of the sample itself, the absolute reflectivity of the sample is calculated as:

$$R(\lambda) = C(\lambda) \times \frac{I_{\text{sample}} - I_{\text{background}}}{I_{\text{reference}} - I_{\text{background}}} \tag{2.3}$$

where I is the intensity and C is the reflectivity of the PTFE reference sample.

2.1.4   Plasma characterization with Langmuir probe

The first quantitative understanding of the difference between plasma and floating potential was achieved in the 1920s by Irving Langmuir and Harold Mott-Smith [84]. They also developed the so-called 'Langmuir probe', which is a wire electrode immersed in plasma, on which a constant

time-varying electrical potential is applied in order to collect electron or ion currents. Figure 2.4 presents an example of a typical current-voltage curve, which consists of three regions: The positive ion current region, transition region and the electron saturation region. These regions are exploited separately to obtain the plasma parameters such as T_e, the ion flux, ion and electron densities, Debye length, plasma potential and the floating potential [85].
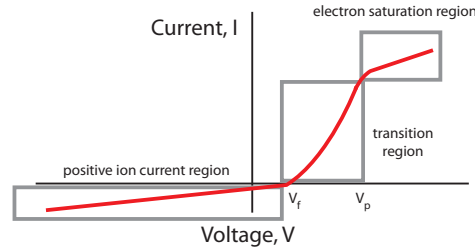
Figure 2.4: Schematic of the three regions of a Langmuir probe measurement.

The characterization of plasma used in this thesis was performed with a commercial Hiden ESPion Langmuir probe.

2.1.5 Other characterization methods

X-ray diffrectometry

Atoms of a solid will scatter x-rays through their electrons. 95% of the solids have a crystal structure and would scatter regular array of spherical waves [86], among which many will be canceled out in most of the directions due to destructive interference. If the lattice atoms have a distance d between them, this would result in a constructive interference, hence a reflection spot in the diffraction pattern [87,88]. d is equal to $\frac{a_0}{\sqrt{h^2+k^2+l^2}}$ for a cubic lattice, where a_0 is the lattice parameter, h, k and l are the intercepts of the diffracting plane with the x, y, and z-axis respectively. From simple trigonometry, the angle satisfying constructive interference equals to $\theta = \sin^{-1}(\frac{n\lambda}{2d})$, where λ is the wavelength and n is an integer.

X-ray diffraction (XRD) measurements were performed using a SIEMENS D500 instrument with Cu Kα radiation (40 kV and 30 mA) at a glancing incidence or in θ-2θ configuration. Glancing incidence was especially used for coatings when it is desired to avoid contribution from the substrate material. All XRD patterns were obtained with scan steps of $0.02\,°$ and with 8 s of acquisition time.

Scanning tunneling microscopy and spectroscopy

Scanning tunneling microscopy (STM) is a surface science technique which was invented in 1981 and it uses the principle of quantum tunneling between a tip and a surface to be imaged [89]. Scanning tunneling spectroscopy (STS) is an extension of STM to measure local DOS of the surface.

STM and STS were used for the experiments described in Chapter 8 and they were performed with a commercial qPlus Omicron microscope at 77 K operated with a Nanonis Control Systems from SPECS GmbH. All STM images were recorded in constant current mode with the bias voltage applied to the tip. The samples were heated to 80-400 °C prior to measurements in

UHV. STS measurements were acquired with the lock-in technique (f $=$ 538 Hz, $V_{mod} =$ 4 to 6 mV).

Scanning electron microscopy

A scanning electron microscope (SEM), as the name suggests, is an imaging tool with a working principle of scanning a focused electron beam over the sample surface [90]. The primary electrons are usually emitted from a tungsten filament (cathode) and are focused on the sample by magnetic lenses. These interact with the sample surface either to produce secondary electrons via inelastic scattering, or reflect high energy electrons via elastic scattering, so-called backscattered electrons. The actual measured quantity is the intensity of the signals from these two kinds of electrons, while the principle of scanning is simply deflecting the primary electron beam. The low energy secondary electrons are more sensitive to surface and, therefore, provide the image of the surface. Back scattered electrons, on the other hand, contain some information about the chemical character of the sample, since their intensity is related to the atomic number.

SEM images presented in Chapters 3 and 6 were taken with a Hitatchi S-4800 device. The images in Chapter 4 were taken after focused ion beam milling in IPP Garching with a NanoLab 600 Helios device and the images in Chapter 7 were taken with a Zeiss Supra 35 device.

4-point electrical resistivity
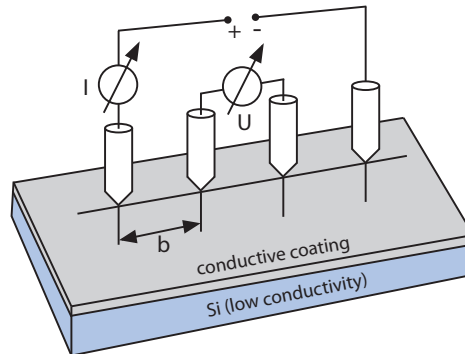
Figure 2.5: Illustration of the 4-point probe electrical resistivity measurement device.

Electrical sheet resistance ($R_\square$) of a thin film is described as the electrical resistance which the electrical current flowing along the plane is subjected to. The quantity being measured by the 4-point method is $R_\square$, which can further be multiplied by the film thickness in order to give an estimate of the specific resistivity (ρ) of the film. Figure 2.5 is a schematic of the measurement device, which consists of four equidistant electrodes that are aligned on a line with a spacing 'b'. With the valid assumptions that the films thickness is smaller than the dimensions of the insulating substrate and the distance b, the following equation holds [91–93]:

$$R_\square = \frac{U}{I} \frac{\pi}{ln(2)} \tag{2.4}$$

where U is the measured voltage and I is the measured current. Since the actual film has finite dimensions, a small correction has to be made to the measured $R_\square$ value. For the experiments in

the thesis, Nagy SD-510 system was used to perform 4-point electrical resistance measurements both under high vacuum and in air. The method is used in Chapters 3 and 5.

Raman spectroscopy

Raman spectroscopy relies on Raman scattering which is an energy shift of a monochromatic light beam after interactions with lattice or molecular vibrations [94, 95]. In this thesis, the use of Raman spectroscopy was limited to the analysis of the vibration modes of the layered carbon materials in Chapters 8 and 9. Therefore, an explanation of the peaks in a typical spectrum is provided in Chapter 8.

Raman spectroscopy measurements were performed using a WITec alpha 300 confocal Raman microscope. The wavelength of the excitation laser was 532 nm and the power of the laser was kept at 2.1 mW without noticeable sample heating or damaging. The laser spot size was 360 nm at $100 \times$ magnification. The spectral resolution was 3 cm^{-1} and each spectrum was an average of 20 accumulations with an integration time of 0.5 seconds per accumulation. For Raman microscopy integration time was 1 second without any averaging.

Line profiles

Line profiles of some samples were measured in order to obtain average roughness (r_a) values. A Tencor 500 α-stepper device was used and r_a was obtained by averaging five measurements of 1 mm length.

2.2 Plasma exposure facilities

2.2.1 Facility-I

This facility consists of 4 high or ultra-high vacuum (HV, UHV) chambers as illustrated in Figure 2.6. Background pressures of the chambers were obtained with individual conventional pumping systems. The samples were always introduced into the system from the HV loadlock chamber, whereas the rest of the system stayed under vacuum. The transfer chamber is a gateway between all the other chambers with a typical background pressure of 1.5×10^{-7} Pa. The chemical and electronic structure analysis of the surfaces of the samples were done in the UHV photoemission chamber, which cannot operate above 1×10^{-6} Pa.

The experiment chamber had a background pressure between 2×10^{-5} to 1.5×10^{-4} Pa, depending on the devices mounted on it. At the heart of the experiment chamber there is a carousel equipped with biasable and heatable sample holders where the samples are mounted in order to be exposed to plasma. One of the sample holders was usually equipped with a quartz microbalance in order to measure coating rates. This chamber was often equipped with magnetrons either for performing coatings or adding metallic impurities to the plasma. Various gas mixtures could be added either directly into the chamber (e.g. for magnetron sputtering) or through the plasma source (described below). Additionally, an *in situ* spectroscopic reflectometry system was built around the vacuum vessel, which is discussed in detail below.

Plasma exposure experiments which are discussed in Chapters 3, 5 and 6 were conducted at this facility. However, for a better XPS and UPS resolution and less oxygen content, the experiments in Chapter 3 were repeated at Facility-II.
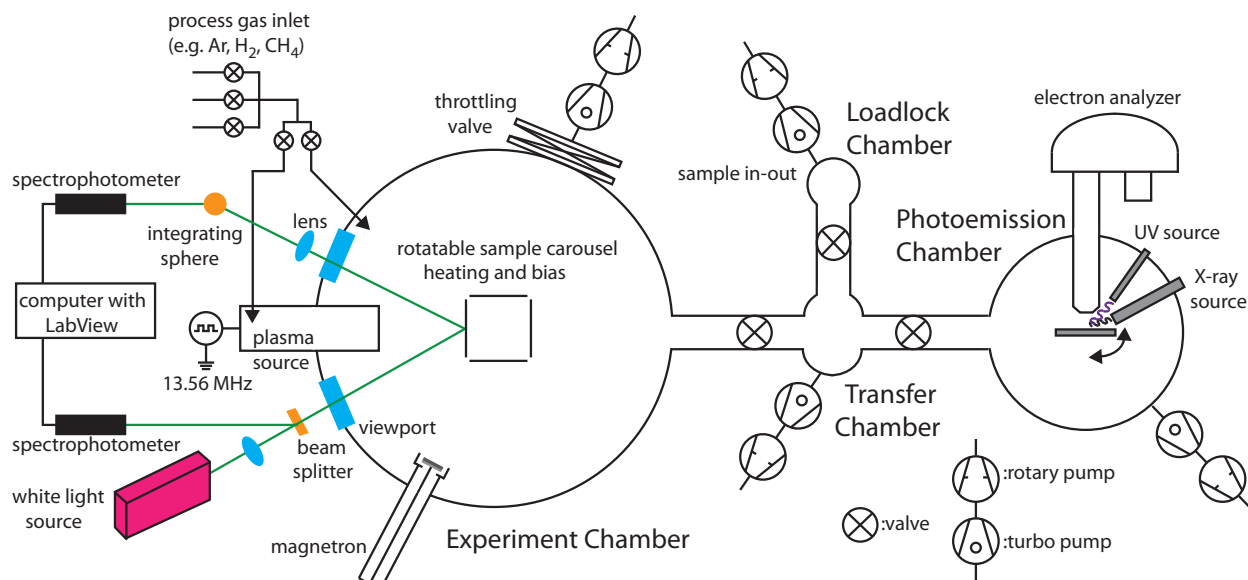
Figure 2.6: Drawing of the Facility-I

Plasma source

Plasma was created in a Pyrex tube of 120 mm diameter and 400 mm length through a matching network by a 13.56 MHz RF generator at a typical power of 90 W. None of the samples used in this thesis had a surface diameter over 30 mm, which when compared to the diameter of the plasma source ensures homogeneity of the plasma across the sample surface. The radio frequency (RF) power was coupled to the tube by an outer electrode (surfatron). 3 Pa of deuterium pressure (99.8% pureness, rest gas is mostly protium) was used. The Langmuir probe measurements were performed 5 cm away from the sample, where an electron temperature of 4.5 ± 0.5 eV and a total ion flux of 3.25×10^{15} cm^{-2}s^{-1} were obtained. Evaluation of D_α and D_β spectral line emission of deuterium also resulted in this electron temperature range [96]. The optical emission spectrum of the plasma did not show any emission lines other than those of deuterium and the differentially pumped mass spectroscopy system revealed no more than a total of 0.02% residual products in the vacuum chamber during plasma exposure. No residual product was identified when the mass spectrometer was measuring only the plasma ions (ionizer switched off).

In-situ **XPS system**

The experiment chamber is (via the transfer chamber) connected to a UHV chamber housing a photoelectron spectrometer for *in situ* XPS and UPS measurements without breaking the vacuum. The spectrometer includes a hemispherical analyzer, an x-ray source (Mg Kα excitation, hν=1253.6 eV) for core level spectroscopy and a UV source (HeI excitation with hν=21.2 eV, or HeII excitation with hν=40.8 eV which is not used in thesis) for valence level spectroscopy. E_f was set to 0 eV and Au 4f$_{7/2}$ peak was set to 84 eV for electron B.E. calibration. The energy resolution of the Leybold EA10/100 system at Facility-I was previously reported as 0.2 eV for UPS and 1 eV for XPS measurements [97].

In-situ **reflectometry setup**

In order to record the evolution of the reflectivity of metallic samples during exposure to plasma, an *in situ* reflectometry setup was built in the experiment chamber of Facility-I [98]. The setup was built around two identical AVANTES USB spectrometers with automatic dark current corrections. A white light source (Schott KL1500 Compact) was used, where the light beam is split into two beams. The first light beam was collected with one of the spectrometers. The second beam enters the experiment chamber through a glass viewport, hits the sample surface and gets reflected, and finally exits from another viewport. Impinging and reflected light beams had an angle of $104\,^{\circ}$ between them, and therefore the actual quantity which is measured was the relative reflectivity, ($\check{R}$, $\phi=52\,^{\circ}$). In order to cope with thermomechanical instabilities of the carousel, the reflected beam was collected into a 2" integrating sphere which was connected to the second spectrometer. The intensity of the plasma light was negligible in comparison to the intensity of the reflected light. Both spectrometers were connected to a computer with a LabView program, which records temporal evolution of the light for both spectrometers.

The spectra collected by the first spectrometer were the reference measurements, whereas the spectra collected by the second spectrometer were the sampling measurements. The sampling measurements were divided by the reference measurements for each time slice, giving the corrected measurements. The system was not absolutely calibrated, thus measures the evolution of the reflectivity. The initial intensity ($I(\lambda,0)$) was the average of the first ten corrected sampling measurement. Relative reflectivity is simply equal to $I(\lambda,t)/I(\lambda,0)$.

2.2.2 Facility-II

Plasma exposure experiments which are discussed in Chapters 7, 8, 9 were conducted in this facility.

Plasma source

A similar (but longer electrodes) plasma source was used to ignite a plasma 75 cm away from the sample, which was mounted on a HV chamber with a metal carousel with heatable and biasable sample holders at the center. 3 Pa of protium (99.9999% pureness) pressure was used, where the background pressure was 5×10^{-6} Pa. The optical emission spectrum of the plasma yielded no peaks other than those of protium and self-ionized mass spectroscopy did not reveal any other ions than those of protium. The protium plasma was characterized with a commercial Hiden ESPion Langmuir probe. The probe measurements were performed 5 cm away from the sample where an average T_e of 3.5 ± 0.5 eV and an ion flux of $1.5 \pm 0.5 \times 10^{15}$ cm^{-2}s^{-1} were obtained. The exact plasma chemistry of the protium ions (H^+, H_2^+, H_3^+) was not known, therefore an estimate of 2 amu was used as the average ion mass, which introduces $\sim 10\%$ uncertainty to T_e calculation. For an electrically floating sample, the ion impact energy (ϵ_i) was calculated as a sum of energy gained traversing plasma sheath (from balancing ion and electron fluxes at the sample surface) and the initial ion energy: $\epsilon_i = (T_e/2)ln(M/2\pi m) + 0.5(T_e)$ which corresponds to 3.34 T_e for H^+ and 3.88 T_e for H_3^+ ions. For simplicity, ϵ_i was taken as 3.6 T_e which is 12.6 $\pm$ 1.8 eV.

In-situ **XPS system**

The photoemission spectroscopy measurements were performed with a VG ESCALAB 210 spectrometer using monochromatic Al Kα radiation (1486.6 eV) without breaking the vacuum. The Gaussian broadening of the spectrometer (convolution of the spectral resolution (which itself is a convolution of the analyzer resolution and the source resolution) and thermal broadening) was calibrated as 0.55 eV for the 20 V analyzer pass energy used in this thesis. Normal electron escape angle and a step size of (maximum) 0.05 eV were used. Initially, wide scan XPS spectra from 0 to 1200 eV were taken in order to specify all the species present on the sample surface. The base pressure in the chamber was around 1×10^{-7} Pa during acquisition. The binding energy scale was calibrated using a clean gold sample and positioning the Au $4f_{7/2}$ line at 84.0 eV binding energy. As all the samples were verified to be stable in UHV and under x-ray irradiation, longer integration times could be used to optimize the signal to noise ratio. A helium discharge lamp emitting in ultraviolet range (HeI, 21.2 eV) was used for the UPS measurements.

2.2.3   High flux plasma exposure

High flux deuterium plasma exposure was performed in the DSM-2 exposure facility at the Kharkov Institute [99,100], where plasma was created in a double mirror magnetic configuration by electron cyclotron resonance (ECR) excitation at 2.375 GHz. The parameters of the stationary ECR discharge plasma created with a power of 200-400 W and at a gas pressure between 2×10^{-3} and 10^{-1} Pa were as follows: $n_e \sim 10^{10}$ cm^{-3}, $T_e \sim 5$ eV. The samples were fixed to a water-cooled movable coaxial holder. A negative bias was applied to the sample holder to accelerate the plasma ions onto the surface. Both fixed and time-varying (with a repetition frequency of 100 Hz) negative bias were used in the experiments. The second case was realized by adding positive half-waves from a separate biphase rectifier to the fixed negative voltage of -1.5 kV, in such a way that the ion acceleration voltage varied between 0.1 and 1.5 kV with a mean value of around 0.5 kV.

The sputtered layer thickness was estimated from weight loss measurements with an accuracy of 25 μg for the 3.14 cm^2 surface area which was exposed. 25 μg corresponds to a thickness of around 8 nm for molybdenum samples. The ion flux was estimated from the ion current density measurements with an accuracy of $\pm$ 30%.

Plasma exposure experiments which are discussed in Chapter 4 were conducted in this facility.

2.3   Coating process

Two different coating methods, namely magnetron sputtering and evaporation were used for the preparation of reflective metal films. Of those, mainly magnetron sputtering was used and will be described in detail.

2.3.1   Principles of the magnetron sputtering coating technique

Coating processes based on sputtering exploit the physics of the sputtering processes described in Section 1. A controlled sputtering process setup consists of the following components: 1- Plasma inside a vacuum chamber which acts as a provider of the sputtering ions. The process gas is often chosen from one of the noble gases. Alternatively, reactive gases such as oxygen or nitrogen

can be used for oxide or nitride coatings. 2- The target material which will be sputtered away. The target can either be RF-biased, continuously or pulsed DC-biased. RF-bias is essential for poorly electrically conducting target materials, in order prevent electrostatic charging. 3- Substrate material on which the deposit will be formed. Applying a bias and/or heating the substrate are additional options. 4- Optionally, magnets in order enhance the sputtering of the target. Such a magnetically enhanced system is called a magnetron and is illustrated in Figure 2.7.
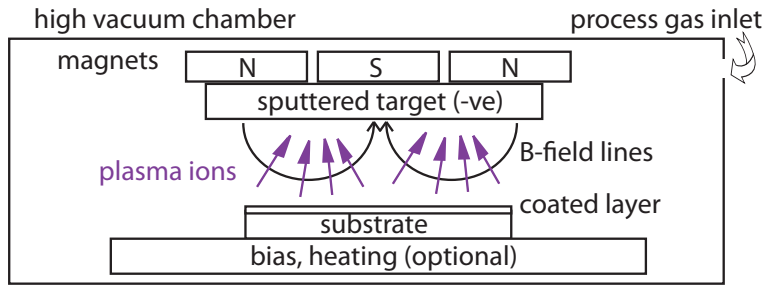
Figure 2.7: Illustration of coating of a substrate by the magnetron sputtering technique.

The sputtering process requires a negative bias on the target which creates an E-field between the target and the ground. With the help of this E-field, the electrons are accelerated and some of them collide with atoms to produce ions and more electrons. Of these charged particles which are created by the E-field, the electrons are accelerated towards the ground which cause more collisions on their way, whereas the ions tend towards the target (cathode). The ions sputter the target materials and result in ejection of atoms from its surface. The sputtered away atoms have a random direction and can strike and condensate anywhere on the vacuum vessel. The advantage of including a magnetic field is concentrating the ionization process in the proximity of the target. As shown in Figure 2.7, the magnets are placed behind the target causing localized erosion, which causes the coating rate to vary with time. The localization of the plasma also heats up the target material and, therefore, the system is often cooled by running water across the back of the magnets. The main advantages of using magnets are achievement of higher sputtering rates, operation at lower pressures and most importantly obtaining a directional deposition.

2.3.2 Dynamics of the coating process

Figure 2.8 is a schematic illustration of the physical vapor deposition process which includes nucleation, island growth, impingement and coalescence of islands, formation of polycrystalline islands and channels, development of a continuous structure, and film growth [101].

Nucleation is a copious process, which makes the nuclei spacing and the grain size impingement in the order of 10 nm or less [102]. Coarsening is driven by surface atom diffusion and grain boundary motion during island coalescence [101]. The system will try to minimize its energy, in such a way that an island with a lower energy per atom would consume another one. This process will continue until the local grain size becomes sufficiently large that the grain boundaries are immobile.

At low temperatures, in-plane grain sizes are set by the saturation nucleation density. The mobility of the adatoms are low, and therefore the random orientation of the nuclei would

be preserved as predicted by the ballistic models [103]. The columnar grains are composed of smaller more equiaxed grains, lending the name 'nanocrystalline' for such coatings. At high temperatures, crystal orientation selection during coarsening would be driven by minimization of the interface and surface energy and a decrease in the grain boundary area [102]. Typically, the islands with the densest planes are selected, which are the (111) planes for the face centered cubic (fcc) and (110) planes for the body centered cubic (bcc) phases. The temperature dependence of the process has led to the development of structure zone models [104, 105].
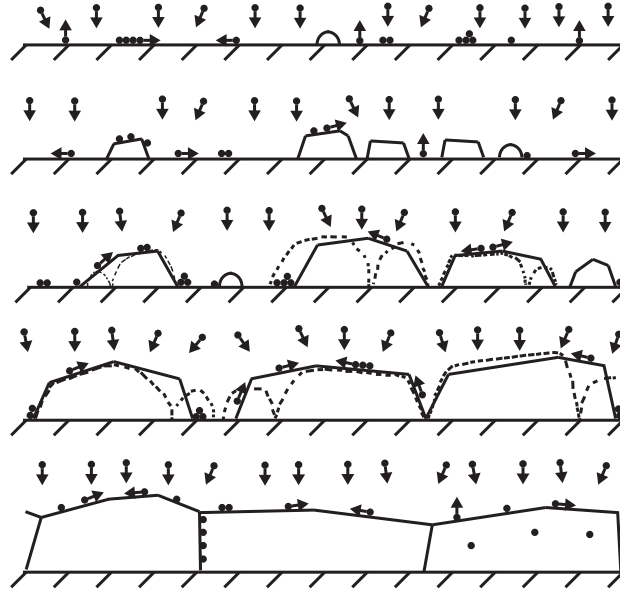
Figure 2.8: Illustration of the coating process. The illustration in [106] is taken as model.

2.4   Reflectivity of the Mo and Rh coatings

This subsection gives an example of two reflecting coating techniques: Magnetron sputtering and evaporation. It provides information about why the magnetron sputtering technique is superior to evaporation. All the coatings presented in the later chapters are prepared by the magnetron sputtering technique.

2.4.1   Preparation of the films

Coating of both Rh and Mo films were performed in high vacuum chambers, pumped down to a pressure about 2×10^{-4} Pa for magnetron sputtering [107] and 1×10^{-5} Pa for electron beam evaporation [108]. Silicon (Si) wafer pieces, mechanically polished stainless steel 316L (SS316L) and mechanically polished Mo were used as substrates for Mo films, while polished tungsten was used for Rh films. Mechanical polishing was done first by abrasive SiC paper, then by diamond paste, and finally by an alumina powder of 0.05 μm particle size.

For magnetron sputtering of Mo, water cooled magnetrons with 100 W pulsed-DC power were used. A round Mo target (99.9% purity, 2 cm in diameter) was positioned at a distance of 5 cm from the substrate. Argon was used as a sputter gas at a pressure of 1.8-2 Pa. The pulse

parameters were fixed to 50 kHz and 1056 ns. Prior to coating, the substrates were biased to -50 V and their surfaces were cleaned *in situ* with a deuterium plasma for 30 min.

For evaporation of Mo and Rh, a commercial electron beam evaporation device (Omicron EFM3) was used. The substrate holder allowed deposition at elevated temperatures by means of resistive heating. The substrate temperatures were measured by a chromel/alumel thermocouple fixed to the back of the substrate. Before deposition, the substrates were cleaned in vacuum by an argon ion gun (5 min, 500 eV).

Both chambers were equipped with quartz crystal microbalance (Inficon XTM), allowing coating rates to be measured and correlated to cross sectional SEM images. Without breaking the vacuum, the samples can be transferred to UHV chambers for core level XPS measurements. The surface morphology of the films was investigated using the SEM technique. The α-stepper was used to measure the r_a values of the surface before and after coating. Total and diffuse reflectivity measurements were carried out with the spectrophotometer. The adhesion properties were evaluated using a CSM Micro Scratch instrument scratch tester. During the test, the applied load was progressively increased from 0 N to 20 N at a rate of 10 N min^{-1} and the scratch length amounted to 10 mm. Per sample, five measurements were taken and averaged to obtain the critical load, which is defined as the minimum load at which the substrate appears in the track. XRD measurements were performed at a glancing incidence of 5 °.

2.4.2 Reflection performance of the coatings

Evaporated Mo films

Figure 2.9(a) shows a typical Mo 3d core level spectrum measured by *in situ* XPS of an evaporated Mo film. No effect of the substrate temperature or material on the XPS spectrum has been observed. The survey measurements (not shown here) revealed no impurities other than the adsorbed oxygen O1s peaks, which contributed less than 13 atomic percent. Shirley background substraction [69] and Doniach-Sunjic [68] fit functions were applied to the Mo 3d spectrum, revealing only one component of Mo 3d$_{5/2}$ line at a binding energy of 227.8 eV and a spin orbit splitting of 3.15 eV [108].
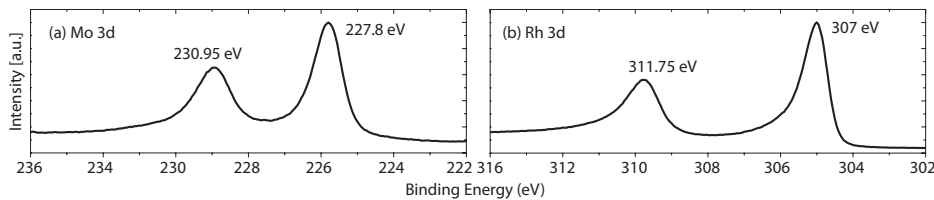
Figure 2.9: Typical (a) Mo 3d and (b) Rh 3d core level XPS spectra measured after evaporation of Mo and Rh films.

The effects of different substrate temperature during coating were already been studied and discussed in [109]. 140 nm thick Mo films were coated on SS316L substrates at room temperature (RT), 350 °C and 550 °C. Figure 2.10 shows the SEM images of the surfaces. The r_a values of the substrate (left of the arrow) and of the coating (right of the arrow) are also indicated. No significant change of r_a was observed after coating. An increase in in-plane grain size can be observed with increasing temperature. At RT, the surfaces of the columnar grains are separated by void boundaries; hence the surface no longer features the reflectivity of bulk Mo. The

Table 2.1: XRD data evaluation results of Mo films prepared by evaporation and magnetron sputtering (Magn.). The reference corresponds to the bcc phase [112].

	Ref.	Evaporation			Magn.
Deposition temperature	-	RT	350 °C	550 °C	RT
Average grain size (nm)	-	7.6	9.4	9.6	10.9
Std. err. (±nm)	-	0.1	0.2	0.3	0.1
Lattice constant ($\mathring{A}$)	3.1472	3.1453	3.1438	3.1502	3.1491
Std. err. (±$\mathring{A}$)	-	0.0003	0.0004	0.0004	0.0002

effect of this structural disorder on the drop of reflectivity has already been discussed [110]. As the deposition temperature increases, the surface packing density increases, leading to an improvement of the reflectivity of the films (Figure 2.11, □, ◇ and ▽ curves).
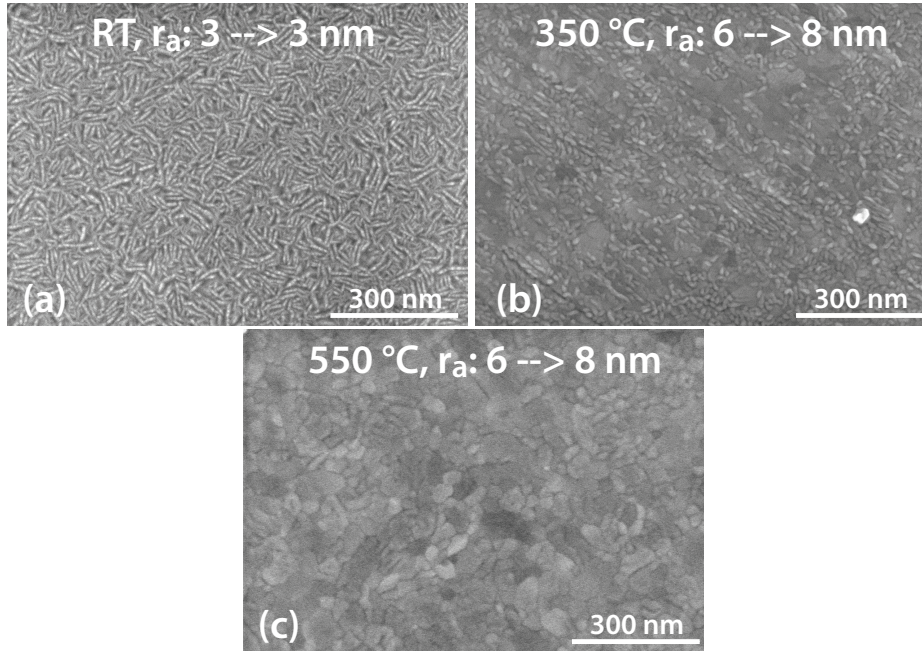
Figure 2.10: Top view SEM images of Mo films (140 nm thick) coated on SS316L substrates by evaporation at following temperatures: (a) RT, (b) 350 °C and (c) 550 °C. Similar results are obtained for coatings on silicon substrates.

Table 2.1 summarizes the lattice constants and crystallite sizes obtained, with their standard errors, after evaluation of the XRD patterns (Figure 2.12(a)). For coatings at elevated temperatures it is observed that the crystallite size (individual crystallites forming columnar grains), calculated from Scherrer's formula (size=$\frac{K\lambda}{\beta cos(\theta)}$, where K is the shape factor taken as 0.9, λ is the x-ray wavelength, β is the full width at half maximum, and θ is the Bragg angle (not the glancing incidence angle)) [111], is larger in comparison to coatings prepared at RT.

No effect of the coating thickness (ranging from 40 to 670 nm), the coating rate (ranging from 0.1 to 0.7 $\mathring{A}$/s) or the substrate material is observed on the surface morphology or reflectivity.

Investigations of adhesion with the scratch-test method were carried out for Mo films evapo-
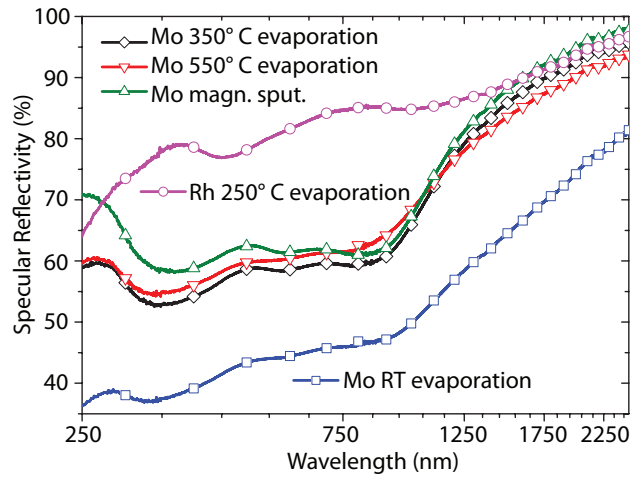
Figure 2.11: Specular reflectivities of all mentioned films measured with spectrophotometry are plotted.
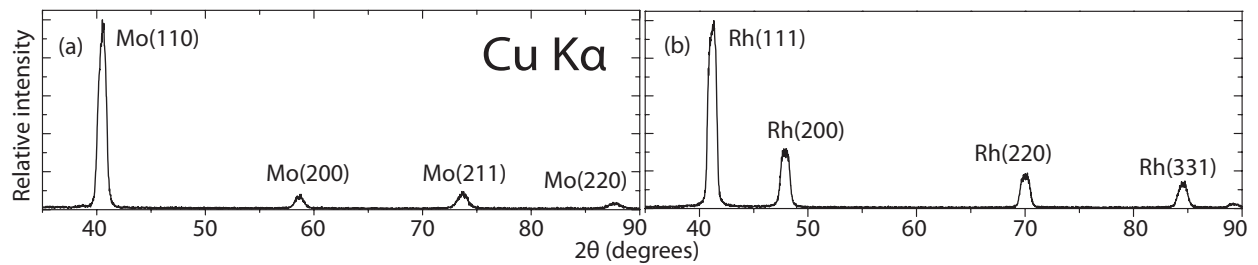
Figure 2.12: Typical (a) Mo and (b) Rh x-ray diffraction patterns measured after coatings using glancing incidence at 5 °.

rated at RT and 550 °C on stainless steel substrates. As defined in Ref. [113] the critical load (N) and the standard deviation for the films deposited at RT and 550 °C are 8.1 ±1 and 11.3 ±2.9 N, respectively. These values are comparable to the results for Rh films coated by magnetron sputtering. This improvement of the adhesion properties for elevated temperature depositions shown here was also addressed in [113].

Magnetron sputtered Mo films

The *in situ* XPS measurements of magnetron sputtered Mo films yield the same spectrum as the evaporated Mo films, as shown in Figure 2.9(a). Coating rates were kept over 1 nm/s in order to obtain films in the compressive stress state [114, 115].

As can be observed from the SEM image (Figure 2.13(a)), magnetron sputtering coating at RT of Mo films reveals a much denser surface compared to the ones coated with evaporation. Figure 2.13(b) shows the cross section image of this film, revealing dense columnar structures. No significant difference of roughness is observed between the substrate and the deposited film. The specular reflectivity of the films coated with this method showed a spectrum similar to the reflectivity calculated from Palik (Figure 2.11, $\triangle$ curve) [7]. Similar structural and optical results are obtained for coatings at a lower working pressure (0.75 Pa, coating speed kept higher than 1 nm/s).
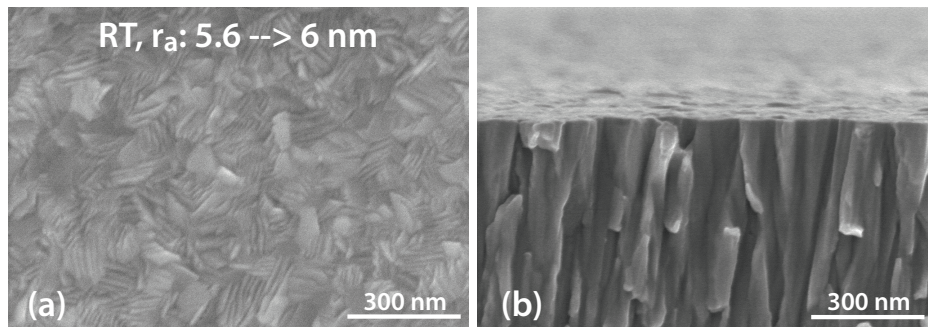
Figure 2.13: SEM images of Mo films (780 nm thick) deposited by magnetron sputtering at RT on a Mo substrate. The cross section image was obtained after cleaving a silicon wafer piece, which is in fact a witness sample of the actual sample being coated.

Evaporated Rh films

Figure 2.9(b) shows a typical Rh 3d core level spectrum measured by *in situ* XPS of an evaporated Rh film. The survey measurements (not shown here) revealed no impurities. After the previously mentioned fitting procedure was applied, it revealed only one component of Rh $3d_{5/2}$ line at a binding energy of 307 eV and a spin orbit splitting of 4.75 eV [16].

Figure 2.14 shows the SEM image of a Rh film deposited at 250 °C, together with the substrate and film r_a values. The specular reflectivity of the Rh film is shown in Figure 2.11 (∘ curve). Figure 2.15 shows the cross section SEM image of a Rh film coated at RT by evaporation. The surface shows a disordered structure, very similar to Mo coated at RT by evaporation (Figure 2.10 top).

According to the identified diffraction lines from the XRD pattern (Figure 2.12-B), Rh is found to crystallize in the fcc phase [116]. The calculated lattice constant a=3.7980±0.0004 $\mathring{A}$ is close to the corresponding value of the database a=3.8031 $\mathring{A}$. The calculated average crystallite size is 10.3±0.2 nm for RT and 10.6±0.2 nm for 250 °C evaporation.
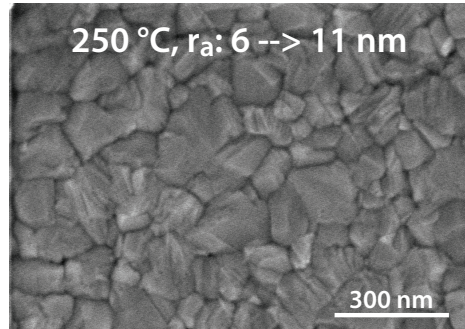
Figure 2.14: Top view SEM image of a Rh film (1 micron thick) evaporated on tungsten at 250 °C
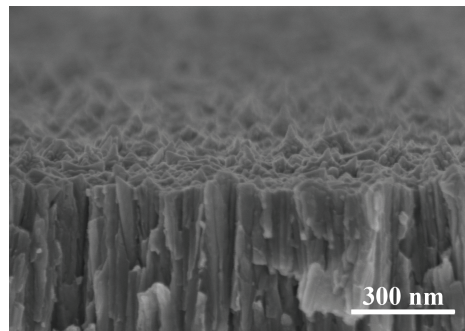
Figure 2.15: Cross section SEM image of a Rh film (950 nm thick) evaporated on silicon at RT. The columnar crystallites are not dense and the surface structure is disordered compared to the magnetron sputtered samples (Figure 2.13(b) and [16]).

2.4.3 Outcomes

Different coating conditions result in structural differences and RT evaporated films exhibit void grain boundaries on the surface which reduce the reflectivity. Magnetron sputtering and elevated temperature evaporation can be considered reliable methods for reflective coatings for the first mirrors of ITER. All mirrors demonstrated acceptable performance under mild erosion conditions and Mo mirrors preserved their optical properties even in severe erosion conditions in TEXTOR (a tokamak in Jülich, Germany). The performance of the coated films under erosion condition tests in TEXTOR are discussed thoroughly in [11], and will be mentioned more in Chapter 3. After this work, relevant ITER size prototype of FMs were designed and manufactured using the magnetron sputtering technique [117].

2.5   Angular reflectivity of the Mo coatings

In this section, the reflectivity of nanocrystalline Mo mirrors for different incident angles is compared with respect to the effects of diffuse and specular crystallite boundary reflections.

Figure 2.16 shows the R(λ=400-800 nm, ϕ=0° and 40°) of two 1 μm thick nanocrystalline Mo mirrors. R(ϕ=40°) was measured by means of using a reference mirror with a Sentech 850 ellipsometer in the reflectance mode. R(ϕ=0°) was measured with the spectrophotometer. Interestingly, one of the mirrors had a better reflectivity at 40° than the other one, whereas it had a worse reflectivity at 0°.
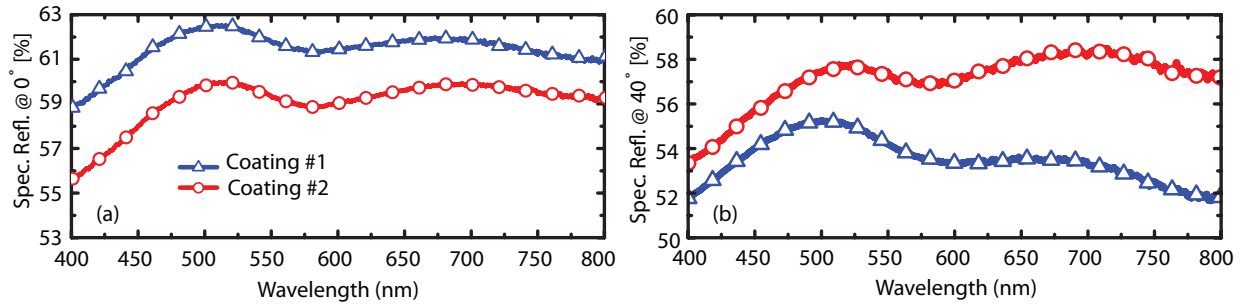
Figure 2.16: Specular reflectivity (spec. refl.) of two nanocrystalline Mo coatings (a) at normal incidence (0°) and (b) at 40°. Both samples had a diffuse reflectivity smaller than 1%, hence roughness effects can be disregarded. Moreover to this point, the differences in the reflectivity are not strongly dependent on the wavelength and, therefore, can neither be attributed to roughness nor to deep oxidation associated with percolation of water.

The nanocrystalline mirrors consist of columnar grains and nanocrystals, which introduces a finite τ_{gb} value which is virtually infinite for single crystal mirrors. For instance, ρ of a 1 μm thick coating was measured as 140 $\pm$ 10 nΩ·m, whereas the bulk resistivity of Mo is 53.4 nΩ·m at RT [118]. In the Drude theory of metals, the dc resistivity is inversely proportional to τ_D. It is clear from these values that the τ_{gb}^{-1} term is comparable to the τ_b^{-1} term. According to Eq. 1.1 and 1.2, a better nanocrystalline sample should have had a higher reflectivity for all incident angles, which it did not (Figure 2.16). Until now, grain/crystallite boundary scattering is considerred to have completely random directions, which in fact is not necessarily true.

The quantum mechanical definition of a crystalline structure has to be considered, in which the solid is defined as weak periodic potential and the grain/crystallite boundaries acting as singularities in this periodicity. In their electrical resistivity model for nanocrystalline solids, Mayadas *et al.* proposed a system which assumes N partially reflecting planes, located perpendicular to the E-field [119]. Mathematically, these planes are potential barriers U, with widths of a delta function. The grain/crystallite boundary scattering term in this model is

$$\tau_{gb}^{-1} = \left(\frac{3V_F\mathfrak{R}}{2\lambda_g(1-\mathfrak{R})} \right) \tag{2.5}$$

where V$_F$=1.7 $\times$ 10^6 m/s is the Fermi velocity for Molybdenum, λ_g is the electron mean free path due to grain (or crystallite) boundary scattering, and $\mathfrak{R}$ is the reflection coefficient at a boundary [120, 121]. Based on the assumption that same mechanism holds for electrons in

response to the dc and optical fields, this model can be extended for the reflectivity. In this case, a system of partially reflecting planes which are perpendicular and parallel to the surface normal with a distance of the crystallite diameter from each other should be considered. Based on the assumption that the penetration depth of light is smaller than the size of 2 nanocrytals, only the first two rows of nanocrystals can be accounted. EM radiation at small incident angles would encounter crystallite boundary reflection ($\mathfrak{R}$) at the plane perpendicular to the surface normal, with the same direction of R. This means that the crystallite boundaries could even increase the reflection measured from the outside for short angles. For higher incidence angles, $\mathfrak{R}$ from the planes parallel to the surface normal will not be parallel to R. Less reflectivity will be measured from the outside.

The Mayadas model cannot explain the reflectivity differences of two nanocrystalline mirrors shown in Figure 2.16. The model assumes a perfect grid of reflecting planes, which is not true in reality. The crystallites have cycloid surfaces [122], which would change the direction of $\mathfrak{R}$ and a random direction would have a probability of having an enhanced reflectivity. A real nanocrystalline solid consists of crystallite and interfaces sites, which take different size parameters such as site-energy, site distance and transition rate [123]. It is very hard to imagine a theoretical understanding of a singular property of nanocrystalline solids with such complicated structural characters [124]. Each interface site would partially specularly reflect, partially diffusively reflect or partially hop the electrons. Nevertheless, each nanocrystalline solid has crystallites with various number of atoms distributed by a certain rule with a finite randomness [123]. The author thinks that a specific distribution of the crystallite and interface parameters has a finite probability to have a better reflectivity of the coating for a specific angle range. Considering the randomness of these distributions, each coating would have its specific angular reflectivity values, which are, in principle not reproducible.

Angular dependence of the reflectivity for the nanocrystalline metals is not further investigated in this thesis. A separate independent study with more similar examples, ellipsometry and photoelectron spectroscopy measurements are necessary in order to express a more solid hypothesis. Nevertheless, the author suggests to calibrate each individual mirror that will be placed on ITER at its desired angle of operation instead of a single reflectivity measurement taken at the normal incidence.

Chapter 3

Properties of deuterium plasma treated Mo

This chapter deals with the reflectivity of Mo, before and after it has been exposed to pure deuterium plasma. The optical characterizations are correlated with the electronic structure and surface chemistry measurements performed using UPS and XPS. Finally, surface morphologies measured with AFM and SEM are presented, discounting any possible effects related to surface roughening as the origin of the changes in reflectivity.

3.1 Experimental preparations

Both magnetron sputtering and deuterium plasma exposure were performed at Facility-I. The magnetron sputtering technique for the nanocrystalline Mo coatings was explained thoroughly in Chapter 2. 25 mm diameter, 2 mm thick, mechanically polished SS316L was used as substrate for $\sim 1~\mu$m Mo film coatings. The sample holders for plasma exposures were coated with Mo to avoid contamination.

A 150 °C mirror temperature and a 200 eV particle energy are the expected wall conditions in ITER [4,125]. Therefore, the substrates were heated to 150 °C by resistive heating and biased to -200 V during plasma exposure. The temperature calibration of the heating system was done with a chromel/alumel thermocouple fixed on the surface of a witness sample. Power supplies of both the voltage and heating systems were connected to RF filters before being connected to the sample holder.

The UV-VIS-NIR reflectivity of the mirrors was measured before and after deuterium exposure using the spectrophotometer (250-2500 nm) and calculated from ellipsometric measurements (300-2300 nm). The change in reflectivity was recorded after different exposure times. r_a of the samples was measured by a Tencor 500 α-stepper. The measurements were done before coating with Mo, after coating and finally after exposure. r_a of the substrates was found to be in a range of 15 to 20 nm. Coating did not have a significant effect on the roughness. AFM measurements of the Mo surfaces were done before and after deuterium plasma exposure in order to gain information on the surface roughness on a nanometer scale and to visualize topographical and structural changes induced by the exposure. The morphology of the mirrors was also investigated by top view SEM images taken before and after exposure.

For electrical resistivity tests, ~ 21 nm of Mo was coated on a Si(100) surface. The sample

was biased to -200 V and exposed to deuterium plasma. The sheet resistivity of Mo was recorded before, during and after deuterium exposure without breaking the vacuum. The sheet resistivity was multiplied by the thickness values of the virgin and exposed Mo (for the latter, estimated remaining thickness after erosion), in order to obtain the specific resistivity of the film.

In situ XPS and UPS measurements were done both after the coating and after plasma exposure. Wide scan XPS spectra from 0 to 1200 eV showed only Mo and oxygen. Though the experiments were held at Facility-I, they were repeated at Facility-II for better resolution XPS and UPS measurements with less oxygen content. The photoemission spectra obtained at Facility-II complements those performed at Facility-I.

3.2 Results and discussion

The negative bias on the mirrors would result in 200 eV ion energy of the impinging D^+ ions, which physically sputters the Mo surface [6]. (-200 V is the applied voltage measured outside of the chamber. If the acceleration potential is calculated with respect to the plasma potential which is around +35 to 40 V, it would be 240 eV. However there is also an unknown amount of voltage drop due to the inner impedance of the system. Moreover to these, effects of secondary electrons and sheath expansion have to be considered. In conclusion, the ion energy would be at some value below 240 eV, and 200 eV is a decent estimate.) In addition to physical sputtering, deuterium is also implanted into the bulk Mo layers with a highest concentration at 4.4 nm depth and a maximum penetration depth of ~ 11 nm estimated from TRIM calculations [126]. This is followed by the diffusion of the deuterium in Mo. These three processes are in competition during the plasma exposure and in the end deuterium may be present in different forms: atomic, molecular (or larger bubbles), or bound to a defect or impurity [127].

3.2.1 Mechanical changes

Previously, blistering due to deuterium implantation was reported to happen with implantation energies above 1 keV [128]. Actually, blistering can still happen at energies used in this work, but either for polycrystalline mirrors (discussed below with examples) or for exposure with higher fluxes (discussed in detail in Chapter 4). Optical and SEM images revealed no blistering after exposure and no significant change in r_a values was observed. Moreover, the diffuse reflectivity of the films, which is linked to the roughness via Bennett's law (Eq. 1.5), showed no change.

The weight loss was measured using a Mettler M 3 micro balance (with 1 μg repeatability). Using a sputtering yield of 0.001 atoms/ion from literature [6], a D^+ ion flux of 1.55×10^{15} $cm^{-2}s^{-1}$ can be estimated. Combining this with the Langmuir probe data results in an average molecular mass of 4 amu and a total ion flux of 3.25×10^{15} $cm^{-2}s^{-1}$, indicating the presence of molecular ions, possibly D_2^+ and D_3^+. The contribution of molecular ions to physical sputtering is omitted since their particle energy is below sputtering yield threshold [6,43]. It should be mentioned that this value of $1.55 \times 10^{15} D^+$ ions/cm^{2}s^{-1} may not be very accurate. If the acceleration energy is considered as 240 eV instead of 200 eV, the sputtering yield would be 0.002 atoms/ion, resulting in half of this value. Nevertheless, direct measured quantities such as the erosion rate and the total ion flux remain within good accuracy.

3.2.2   Spectral changes

Exposures on coated Mo were carried out for time periods of 1h, 3h 30', 8h 30', 20h 5' and 55h 20' which is equal to a range of fluences between 1.2×10^{19} and 6.5×10^{20} ions/cm^2. The final reflectivity was very similar for all the fluences (Figure 3.1(a) and (b)), where 1 to 48 nm material was removed. The maximum amount of material removed corresponds to 18 ITER discharges in equatorial ports and 38 discharges in the upper ports in the first wall positions without any protection. If the mirrors are going to be placed in protective ducts, the number of ITER shot estimations increases by several orders of magnitude [129].

After an initial decrease, the reflectivity attained a constant value, which was similar for all fluences within the stated range. This indicates that the implantation of deuterium, the erosion of the surface layer and the diffusion into the bulk reach an equilibrium state. Furthermore, neither blistering nor increase in surface roughness was observed, showing mechanical effects may be discounted as the cause of the change in reflectivity. Figure 3.1(c) shows the difference between the initial reflectivity of Mo and the reflectivity after any of the exposures within the fluence range from 1.2×10^{19} to 6.5×10^{20} ions/cm^2. The maximum discrepancy between the two reflection drop measurements does not exceed 1.5% in the whole wavelength range.

The drop of reflectivity may be explained with the complex permittivity calculated from the ellipsometric measurements (Figure 3.2(a)). The complex permittivity of the exposed mirrors was similar for the whole fluence range. A single layer model was used for extraction of the real and imaginary parts of the permittivity. The penetration depth of light in the virgin Mo was also calculated and found to be 10.6 nm and 16.8 nm for wavelengths of 800 and 500 nm respectively. These values increased to 11.6 nm and 17.6 nm for exposed Mo mirrors (Figure 3.2(b)). The reflectivity (and therefore the complex permittivity) is an average function of the top layers containing deuterium and the bottom virgin layers but since the mirror subsurface was in equilibrium (between implantation, sputtering and diffusion), this single layer model is always a valid approximation (A double layer model consisting of deuterium implanted Mo and virgin Mo can also be considered as an alternative. However, in reality, deuterium concentration in the Mo subsurface is continuously varying in the z direction; therefore a double layer model practically has the same error as the single layer model. Using a many layer model which considers the deuterium gradient in the z direction is impractical. Single layer model approximates the reflectivity spectrum very close to the measured spectrum and, therefore, is effective and sufficient). The smaller decrease in $\varepsilon 1$ (the real part of the permittivity) of exposed mirrors with increasing wavelength above 827 nm is attributed to a shorter intraband relaxation time compared to virgin mirrors [121] (Eq. 1.2(c)). This suggests enhanced light scattering, which can be attributed to surface and grain boundary scattering, defect, and impurity scattering [130, 131] (Eq. 1.3). Since the diffuse reflectivity measured by the spectrophotometer does not increase after any of the exposures, surface and grain boundary scattering are negligible (within the optical skin depth and for the E-field parallel to the surface normal, see Section 2.5). The defects and impurities are increasing the frequency of scatter events in the Mo lattice. In this particular case, the impurities are the implanted deuterium and the defects (e.g. voids) are caused during and after implantation of deuterium. Since these are subsurface effects, the scattered light is not collected as diffuse reflectivity and is lost in the subsurface (e.g. to lattice vibrations). The fact that the reflectivity remains constant above 827 nm supports the argument that surface effects are negligible. The lower amplitude of $\varepsilon 2$ (the imaginary part of the permittivity) of exposed mirrors compared to virgin mirrors for lower wavelengths is attributed to weaker optical absorp-
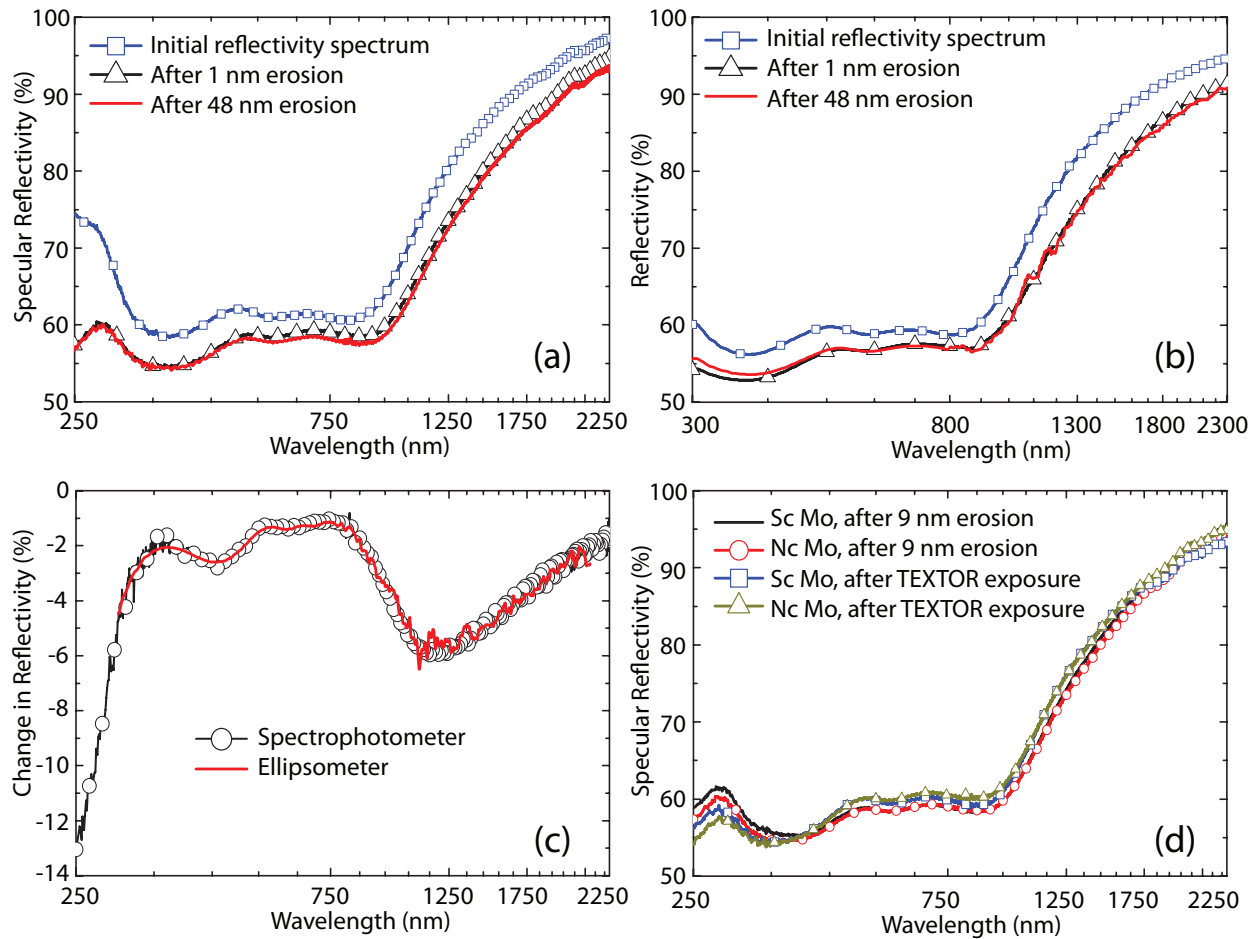
Figure 3.1: Initial reflectivity and deuterium exposed reflectivity of Mo measured by (a) spectrophotometer and (b) calculated from the ellipsometric measurements. (c) Reflectivity drop of Mo after deuterium exposure. (d) Comparison of single and nanocrystalline Mo reflectivities after deuterium exposure measured by spectrophotometer.

tion associated with the interband transitions [121]. This is also due to a higher concentration of deuterium and deuterium induced defects in the subsurface layers of Mo mirrors as a result of implantation. The changes in the interband transitions are further explained in terms of the valence band structure of Mo in the following sections.
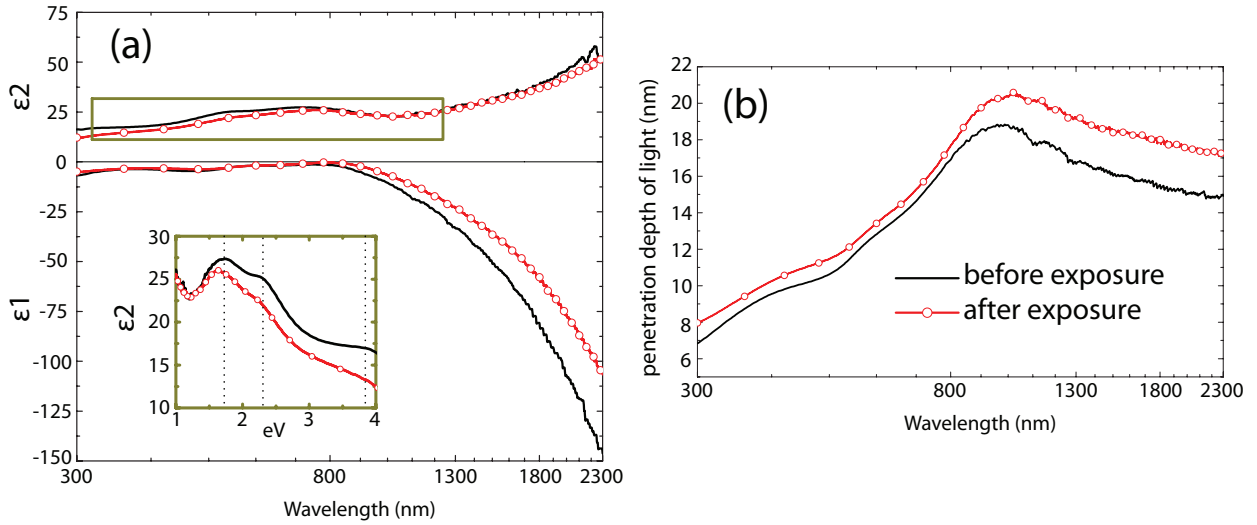
Figure 3.2: Complex permittivity $\varepsilon = \varepsilon 1 + i\varepsilon 2$ (a) and penetration depth of light (b) calculated from simulations of the ellipsometry data. Boxed area is shown in the inset, using the relation $1240/\lambda(nm) \approx \lambda(eV)$ for the wavelength axis.

Further exposures of 1.2×10^{20} ions/cm^2 (~ 9 nm removal) were done for single and nanocrystalline Mo mirrors and similar final reflectivity spectra were obtained (Figure 3.1(d)). This was also the case for the exposure in a tokamak where 120 nm of coated Mo had been eroded (TEXTOR tokamak, mixture of 50% H and 50% D with an impurity content of 3% C and 1% O, total particle fluence of 1.4×10^{21} ions/cm^2, surface temperature of $670\,^{\circ}$C to $1240\,^{\circ}$C and electron temperature of 30.6 eV) [11]. This in turn suggests a similar steady state condition for single crystalline mirrors. The fact that single and nanocrystalline Mo showed a similar change in reflectivity suggests that grain boundary scattering is negligible. Since there was no dramatic change in roughness either, this result also suggests that the presence of deuterium impurities and implantation induced defects is the main mechanism which increases the scattering of light. In other words, presence of deuterium and deuterium induced defects reduced the intraband relaxation time, hence the decrease in $\varepsilon 1$.

3.2.3 Electrical resistivity

Figure 3.3 shows the specific electrical resistivity of an initially 21 nm thick Mo layer before and during deuterium exposure. The initial specific resistivity of the coating was around 10 times more than the bulk resistivity of Mo (5.7×10^{-6} Ω·cm) [118]. Grain boundary scattering is obviously the most dominant scattering mechanism for an E-field perpendicular to the surface normal. In the Drude theory of metals, the dc resistivity is inversely proportional to the intraband relaxation time, based on the assumption that the same scattering mechanism holds for electrons in response to dc and optical fields [121]. The specific resistivity and the reflectivity

of an exposed Mo film are both an average function of the top layers containing deuterium and the virgin bottom layers. It is clearly seen in Figure 3.3 that the specific resistivity increases upon deuterium exposure but remains constant after a certain fluence is reached, supporting the suggestion that the same physical mechanism governs both properties.

The initial increase in the resistivity is attributed to the introduction of scatter centers as a result of impurities and defects in the Mo subsurface. It is also interesting to notice that the resistivity stays rather constant even though the thickness drops down to $\approx$ 13 nm. Of course, even a 1 nm misestimation of the initial surface thickness will change this constant trend to a linearly increasing trend. Nevertheless, it is clear that the surface scattering does not play a great role when compared to very dominant grain boundary scattering term. The effect of impurity and/or defect scattering is, on the other hand, is only 4 times smaller than grain boundary scattering.
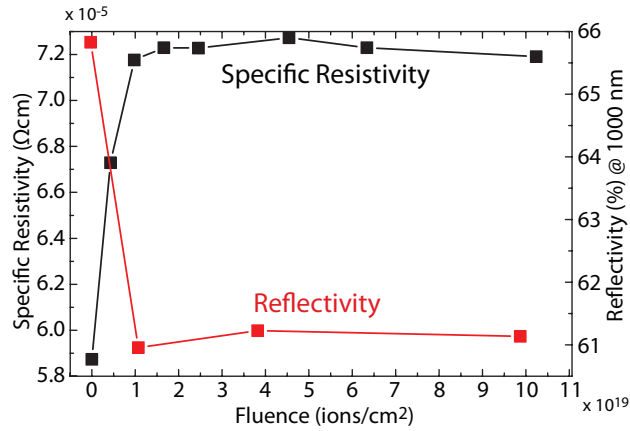
Figure 3.3: Specific resistivity of 21 nm Mo coating before and during a deuterium exposure, together with the reflectivity of 1 μm mirrors at a wavelength of 1000 nm before and after deuterium exposures.

3.2.4 *In situ* **reflectivity**

In situ reflectometry setup was used to monitor the evolution of the reflectivity during deuterium plasma exposure [98]. Figure 3.4 shows the *in situ* reflectivity measurements of (a) single crystalline, (b) nanocrystalline and (c) polycrystalline Mo mirrors at θ=52° during deuterium plasma exposure. The samples were biased to -200 V and they were self-heated to 80-85 °C during exposure. The dashed lines indicate the time of plasma switch-on and, somewhat later, -200 V bias application.

For single and nanocrystalline Mo (Figures 3.4(a) and (b)), an initial increase in reflectivity at plasma switch-on, possibly due to the instantaneous removal of either native oxide or a hydrocarbon layer built up during air storage can be observed. Following this, the reflectivity drops only slightly after the bias is applied and remains virtually constant throughout the exposure. The drop in reflectivity appears lower for the nanocrystalline sample, because this sample initially had a lower reflectivity (than usual) to start with. Unlike in the case of single and nanocrystalline samples, the reflectivity had continuously decreased for the polycrystalline Mo

sample (Figure 3.4(c)). After the exposure, the loss of the specular reflectivity of this sample was even observable to the naked eye. Optical microscopy images revealed heavy blistering occuring on the surface, which is typical for polycrystalline samples.

The *in situ* reflectometry results proves that the reflectivity of single and nanocrystalline Mo mirrors degrades initially, but retains constant during further exposure. Moreover, it is once again shown that polycrystalline samples cannot be considered to be used as light reflecting components while being exposed to hydrogen plasma.
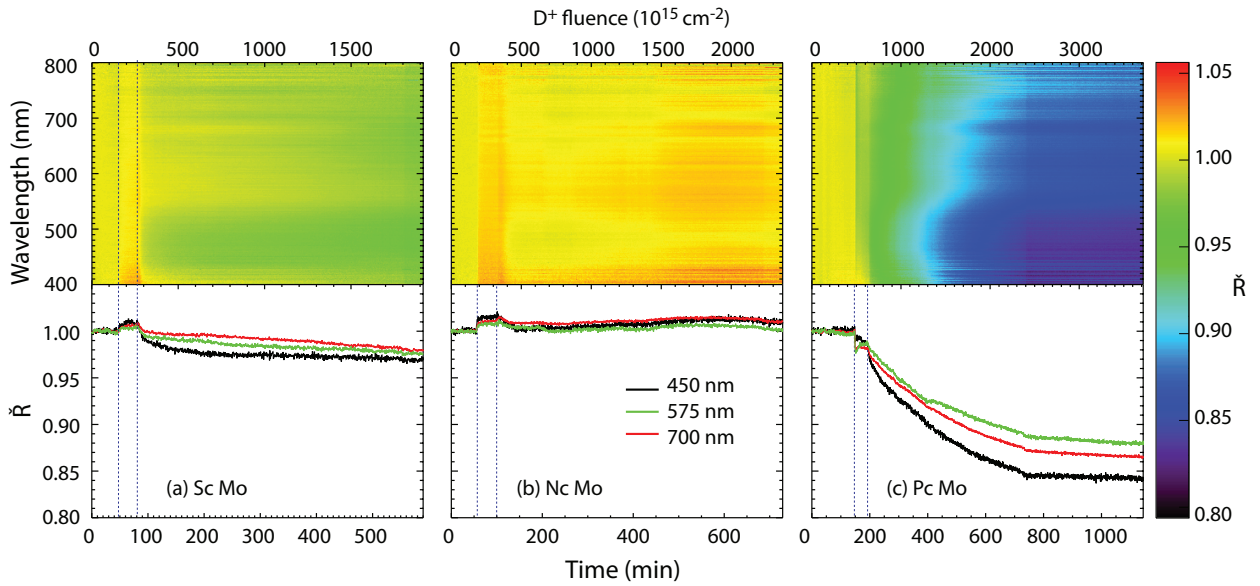
Figure 3.4: Evolution of the reflectivity of (a) single crystalline (b) nanocrystalline and (c) polycrystalline Mo mirrors during deuterium plasma exposure.

3.2.5   Photoelectron spectroscopy

The Mo coated mirrors were characterized before and after exposure by XPS. The core level lines and fits are represented after normalization in Figures 3.5 and 3.6, and the relative concentrations of the individual species are presented in Table 3.1. UPS and valence level XPS data are presented in Figure 3.9.

As with the reflectivity of the exposed mirrors, the photoelectron spectra did not vary with fluence.

Core level

Core level XPS spectra of the as-coated mirrors consisted of only two elements: Mo itself and the physisorbed oxygen species on the surface. Mo was in a pure metal state, with the Mo $3d_{5/2}$ peak at 227.7 eV with a spin-orbit splitting of 3.15 eV (Figure 3.5(a)). The oxygen O 1s region consisted of two species, where the broader peak over 532 eV ($\sim$ 3 at.%) corresponds to H_2O

and the narrower peak between 530.5 and 531 eV ($\sim$ 10 at.%) corresponds to OH^-, which are both pyshisorbed on the metal surface (Figure 3.6(a)) [132].

After deuterium exposure, no additional elements were observed on the sample surface. The core Mo 3d region of the deuterium exposed Mo samples consisted of three doublets where the Mo $3d_{5/2}$ peaks are at 227.7, 228.3 and 230 eV with spin-orbit splittings of 3.15, 3.15 and 3.2 eV respectively (Figure 3.5(b)). The first doublet is attributed to metal Mo, preserving its position and shape after exposures. The third peak has an oxide characteristic due to its larger spin-orbit splitting and due to its position at higher binding energies. The second peak is the most interesting peak, not only because it is the most dominant peak but also due to its binding energy. Its binding energy is too low for an oxide (even a hydrogen reduced MoO_2 peak was reported at 228.7 eV [133]) and too high for a metal Mo peak. The author attributes this peak to Mo implanted with deuterium. Pettrovich *et al* had pointed out that a smaller effective number of electrons in the valence band shifts the inner-shell electrons to higher binding energies [134,135]. A 0.6 eV shift to higher binding energy is indicative of charge transfer from Mo towards deuterium. The same phenomenon has already been reported for other transition metal - hydrogen systems [53,136]. As Mo donates its valence electrons to deuterium, inner-shell electrons get more attracted to the ionic core as a result of reduced Coulomb screening through valence electrons. This results in a higher binding energy. This hypothesis is further discussed after presentation of the valence band spectra.

It was observed that the Mo-D peak at 228.3 eV was stable even after it had been exposed to air for 6 months (Figure 3.5(d)), while the as-coated Mo preserved its peak at 227.7 eV (Figure 3.5(c)) during the same period. Furthermore, the Mo-D sample oxidized much less in air in comparison to as-coated metallic Mo, suggesting that oxidation at room temperature is energetically less favorable for this sample. The spectra of the mirrors which were exposed in a tokamak also revealed a peak at 228.3 eV after having been exposed to air 3 months (Figure 3.5(e)). Mo was mostly in an oxidized state for these tokamak exposed mirrors, probably due to elevated temperatures reached during exposure where the gas combination also included 1% of oxygen [11]. It should also be mentioned that all the mirrors which were exposed to air also revealed carbon 1s peak due to the hydrocarbon contamination.

The core O 1s region of the samples exposed to deuterium plasma consisted of 3 species: Physisorbed H_2O and OH^- (hydrogen may either be protium or deuterium), as in the spectrum before exposure, and an additional peak at 530.0 eV, which is typical of oxides (Figure 3.6(b)). Since the O 1s peak at 530.0 eV represented only a 6% atomic fraction, the second peak of Mo $3d_{5/2}$ (228.3 eV, which is around 50 at.%) cannot be attributed to substoichiometric oxides. In comparison to as-coated mirrors, the adsorbed H_2O peak showed only a slight increase, whereas a dramatic increase is observed in the OH^- peak. This increase of OH^- has two reasons: 1) The implanted deuterium atoms attracted the electronegative OH species onto the metal surface, 2) Some of the OH^- was bound to slightly formed Mo oxides, which also generated the Mo $3d_{5/2}$ peak at 230 eV [137]. Only a slight increase of adsorbed H_2O ($\sim$ 5 at.%) in turn suggests that there was no significant increase in the surface roughness, as a larger surface area would have resulted in larger amounts of H_2O adsorption.

Two additional experiments were done in order to determine the effect of deuterium without a plasma treatment and the effect of increase in surface roughness on the oxygen concentrations. In the first experiment, Mo was coated with a process gas of 50% argon - 50% deuterium mixture instead of pure argon and $\sim$ 5 at.% of adsorbed H_2O (hydrogen is probably partly deuterium)
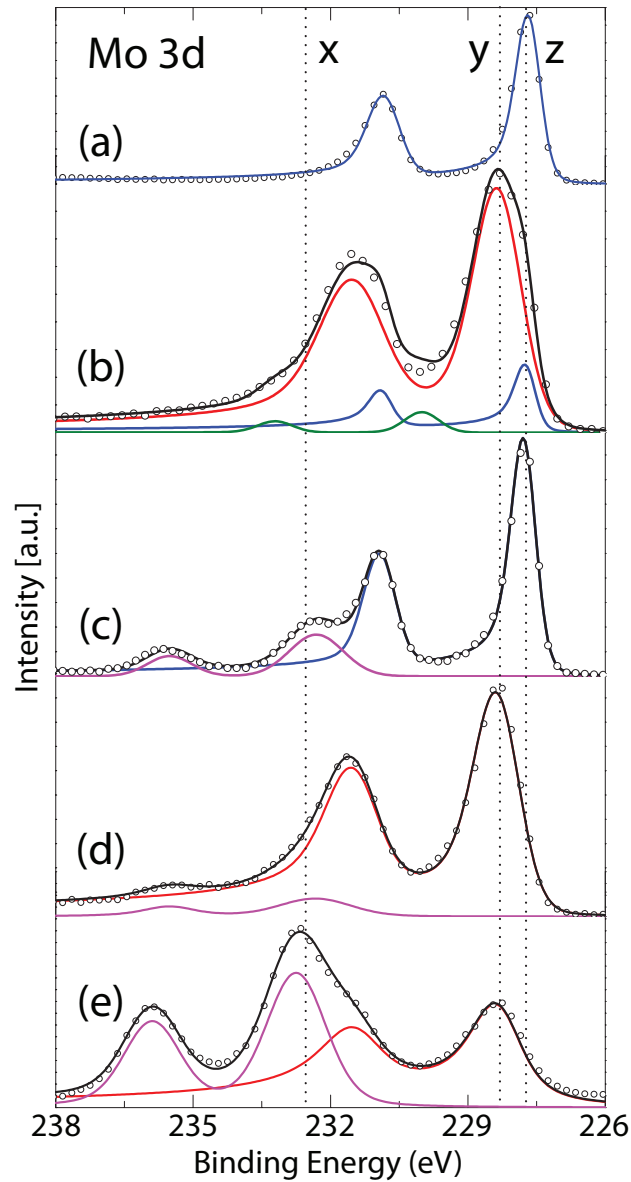
Figure 3.5: Core level Mo 3d spectra of (a) as-coated, (b) exposed to deuterium plasma, (c) as-coated and stored in air, (d) exposed to deuterium plasma and stored in air and (e) exposed in a tokamak samples. Lines x, y and z represent the positions of Mo $3d_{5/2}$ peak corresponding to MoO_3 (>232 eV), Mo-D (228.3 eV) and pure Mo (227.7 eV) respectively. Spectrum (b) has one additional Mo $3d_{5/2}$ peak at 230 eV, corresponding to $MoO(OD)_2$. The colored lines are the different components. The open circles are the spectrum data points after background subtraction, where one of every five data points are presented. The solid line behind the open circles is the fit sum of the components.
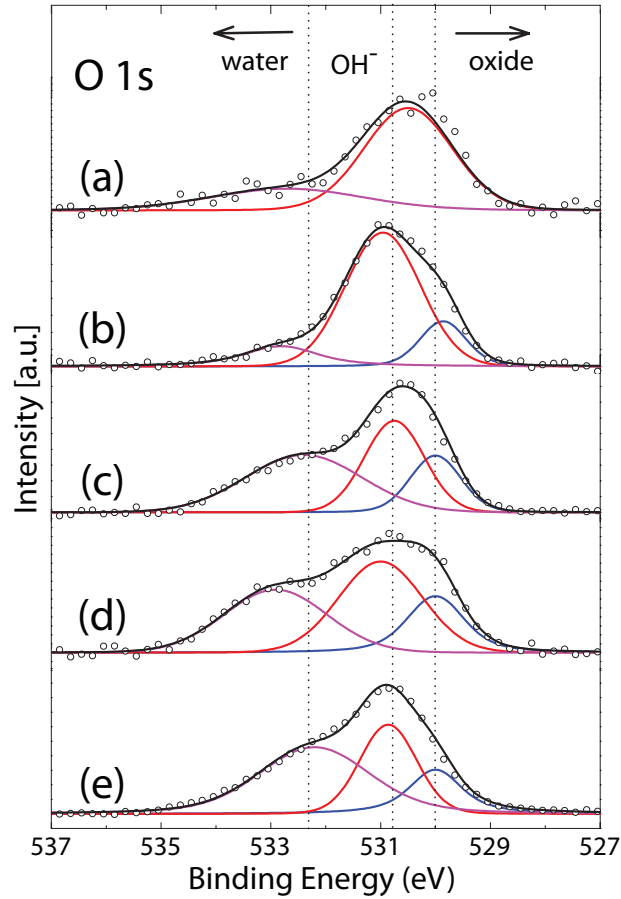
Figure 3.6: Core level O 1s spectra of (a) as-coated, (b) exposed to deuterium plasma, (c) as-coated and stored in air,(d) exposed to deuterium plasma and stored in air and (e) exposed in a tokamak samples. The broader peaks above 532 eV represent physisorped H_2O or D_2O whereas the peaks below 530 eV represent oxides. The peaks between 530.5 and 531 eV represent the physisorbed OH^- or OD^-. The colored lines are the different components. The open circles are the spectrum data points after background subtraction, where one of every five data points are presented. The solid line behind the open circles is the fit sum of the components.

was calculated (Figure 3.7(a)). This suggests that the presence of deuterium, with or without plasma, results in a marginal increase of the H_2O content to 5 at.%. In the second experiment, a 1 μm Mo coating was exposed to an argon plasma at 150 °C temperature and -200 V bias, where 490 nm of Mo was removed. As a result of this exposure, the r_a value increased from 15 nm to 65 nm and the top view SEM images (Figure 3.8) revealed dendrite like features on the surface. The effect of an increase in the surface roughness on the physisorbed H_2O can be clearly observed after this experiment, where the concentration of H_2O increases dramatically up to $\sim$ 14 at.% (Figure 3.7(b)). These two additional experiments show that deuterium plasma exposure of Mo does not increase the surface roughness, as a dramatic increase in adsorbed H_2O would have indicated such a phenomenon. The marginal increase in H_2O after deuterium exposure is only due to presence of deuterium itself.
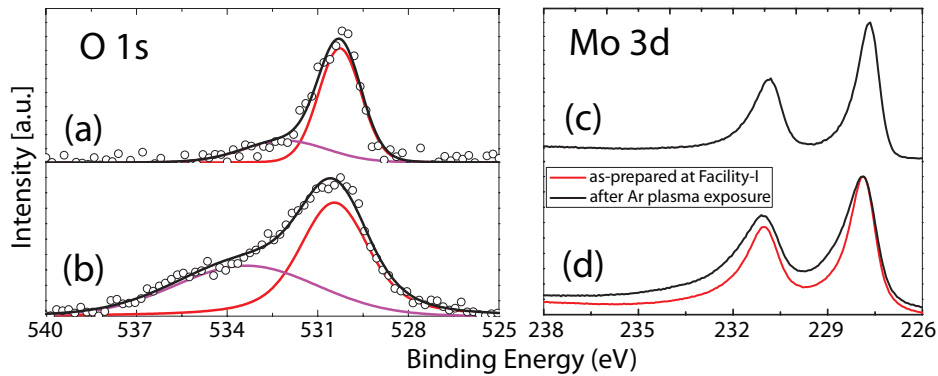
Figure 3.7: Core level O 1s spectra of (a) a Mo coating where 50% argon - 50% deuterium mixture is used as process gas and (b) argon plasma exposed Mo. The colored lines in the O 1s spectra are the different components. The open circles are the spectrum data points after background subtraction, where one of every five data points are presented. The solid line behind the open circles is the fit sum of the components. The Mo 3d spectrum of a coating prepared with a 50% argon - 50% deuterium mixture (shown in (c)) is the same as a coating prepared with pure argon. In (d), the Mo 3d spectrum of argon plasma exposed Mo is shown. The measurements in (b) and (d) were performed at Facility I and, therefore, the peak positions appear at higher binding energies (related to analyzer calibration). In (d), reference spectrum of an as-prepared coating is represented in red color. As a result of argon exposure, a broadening of the Mo 3d peak is apparent without any change in the peak position.

Table 3.1 summarizes the concentrations of all Mo 3d and O 1s species observed in core level XPS measurements of the above mentioned samples. The carbon concentration of the samples that were exposed to air are omitted in this table.

Valence level

Valence level spectrum of photoemission measures the joint DOS, which implies that optical transitions with k conversions will be selected [138]. Moreover, each transition is weighed by its appropriate strength factor. For instance, if the k conversion of a transition is lost or if the transition strength gets substantially weaker as a result of deuterium implantation, it will not appear in the valence band photoemission spectrum. In other words, valence band photoe-
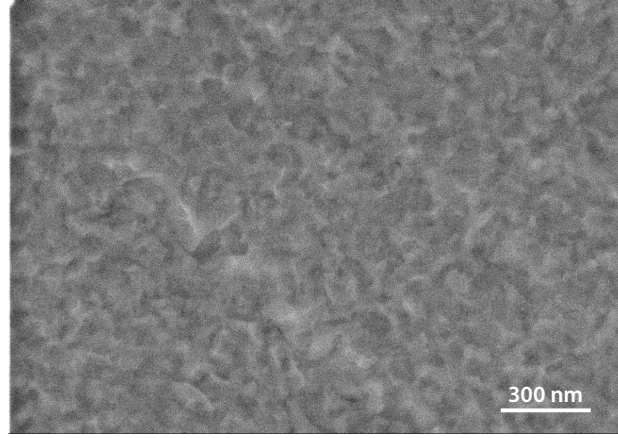
Figure 3.8: SEM image of argon plasma exposed Mo. r_a value has reached 65 nm after 490 nm removal of material.

Table 3.1: Atomic concentration percentages of different species obtained after evaluation of the XPS measurement. Carbon is not taken into account for samples which were exposed to air.

	Mo $3d_{5/2}$ (227.7 eV) metal	Mo $3d_{5/2}$ (228.3 eV) Mo-D	Mo $3d_{5/2}$ (230 eV) MoO(OD)$_2$	Mo $3d_{5/2}$ (>232 eV) MoO$_3$
1- as-coated (only Ar)	87	-	-	-
2- after D plasma	9.5	51.5	2.1	-
3- ♯1 air exposed	38.4	-	-	8.1
4- ♯2 air exposed	-	46.6	-	3.4
5- after tokamak	-	21.5	-	16.5
6- as-coated (50% D, 50% Ar)	82	-	-	-
7- after Ar plasma	69	-	-	-

	O 1s (>532 eV) H$_2$O or D$_2$O	O 1s (530.4-531.0 eV) OH$^-$ or OD$^-$	O 1s (≤ 530.0 eV) oxide
1- as-coated (only Ar)	3	10	-
2- after D plasma	5.0	26.1	5.9
3- ♯1 air exposed	23.6	19.3	10.6
4- ♯2 air exposed	18.1	21.4	10.5
5- after tokamak	30.9	19.7	11.4
6- as-coated (50% D, 50% Ar)	5	13	-
7- after Ar plasma	14	17	-

mission spectroscopy is governed by the Fermi golden rule, just as the reflectivity of a metal. Therefore, the $\epsilon 2$ spectra obtained from the ellipsometry analysis can be corroborated with the photoemission spectra between -1 and 7-8 eV.

Valence level XPS spectra of the as-coated Mo mirrors exhibited 5 peaks around 0.3, 1.7, 2.8, 4.0 and 5.8 eV below the Fermi level (Figure 3.9(a)). The two main peaks at 1.7 eV and 2.8 eV are from the bulk emissions of Mo, whereas the peak at 0.3 eV and the peak at 4.0 eV are also from bulk emissions but also has contribution from surface resonances [139] (A surface resonance peak is actually also a bulk emission peak, but with a higher intensity close to the surface). The peak 5.8 eV below E_f is attributed to the presence of physisorbed oxygen species on the surface. After deuterium exposures, as seen in Figure 3.9(b), the peak at 0.3 eV had vanished completely due to increased surface contamination with oxygen. The two bulk emission peaks at 1.7 eV and 2.8 eV were no longer distinguishable. Moreover, the convolution of these two peaks exhibited a shift to the lower binding energies. The peak at 4.0 eV vanished completely after deuterium exposure, which may be partially due to surface contamination, but also due to weaker interband transitions. The peak at 5.8 eV increased dramatically due to an increased amount of physisorbed oxygen species on the surface.

HeI UPS measurements of as-coated Mo exhibited the same peaks as discussed above at around the same energies of 0.3, 1.7, 2.8, 4.0 and 5.8 eV below E_f, respectively (Figure 3.9(c)). This proves that all are bulk emission peaks. As in the valence level XPS spectra, the peaks at 0.3 eV and 4.0 eV vanished completely, the peaks at 1.7 eV and 2.8 eV were shifted around 0.5 eV to lower binding energies and were broadened and the peak at 5.8 eV increased dramatically after deuterium plasma exposure Figure (3.9(d)). Moreover, the last peak also had a shoulder around 7 eV below E_f. An introduction of a new peak around this energy due to hydrogen implantation was reported for other transition metal - hydrogen systems [53,140], although it is also possible to attribute this peak to a slight oxidation [141].

The changes in the valence band spectra after deuterium exposure corroborate the discussion about the imaginary part of the complex permittivity. It was seen that the two main bulk emission peaks (1.7 and 2.8 ev below E_f) were broadened and shifted to lower binding energies, just as the individual peaks of $\varepsilon 2$ (Figure 3.2(a) inset). The peak at 4.0 eV, on the other hand, had completely vanished in the photoelectron spectra, which corresponds to UV region of the reflectivity spectrum where the most dramatic drop was observed. The reason for these shifts is the electron donation of Mo to deuterium, which results a negative shift (positive in terms of binding energy) of E_f of Mo. This can also be observed in the core level shift, since the reduced number of valence electrons on the Mo site leads to a decrease in the Coulomb screening of the attraction of the ionic nucleus through valence electrons. The broadening in the valence level spectra can be understood as the reduced degree of order. The Mo lattice exposed to deuterium plasma is subject to distortions during the implantation and collision cascade process. As a result, the transition matrix elements vary with respect to the distortions of the reciprocal lattice.

3.2.6   Surface topography

Surface topography analysis includes AFM topography images and top view SEM images of single and nanocrystalline (1 μm thick on stainless steel) Mo samples before and after exposure. Exposures were done for a fluence of 6.5×10^{20} ions/cm^2 (48 nm removal of nanocrystalline mirror). An additional Mo coating was done on a silicon wafer for a thickness of 100 nm (same
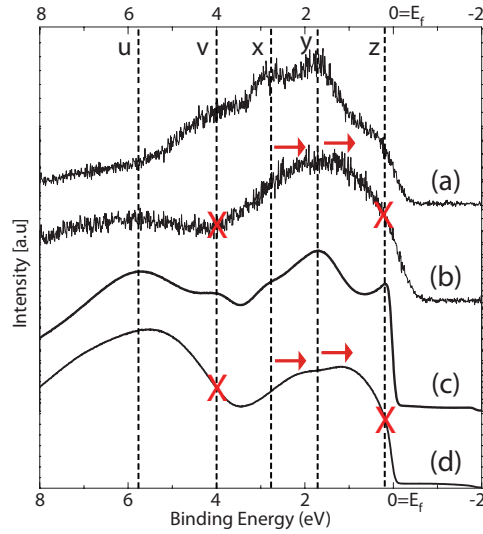
Figure 3.9: Valence level XPS spectra (a) before and (b) after deuterium plasma exposure. HeI UPS spectra (c) before and (d) after deuterium plasma exposure. The line u, which is due to physisorbed oxygen species, increased after exposures. Lines x and y, which are due to bulk emissions, got broadened and were shifted to lower binding energies where the arrows present the shift. The vanished lines v and z are shown by the sign 'X', where they both have contributions from the surface to their intensity.

coating method and conditions as the films on stainless steel substrates), in order to obtain a smoother surface to improve the resolution of AFM imaging. This exposure had a fluence of 8×10^{19} ions/cm^2 (6 nm removal). Figure 3.10 shows the AFM topography images and corresponding line analyses of the samples mentioned above. The images also include the r_{rms} values calculated over the entire image ($10 \times 10 \ \mu m^2$). The three top images are for virgin Mo samples (from left to right: 1 μm coating on stainless steel, 100 nm coating on silicon, single crystalline) whereas the bottom images are the images of the same samples after exposure. Figure 3.11 shows the top view SEM images of these samples with the same order.

Coatings of Mo with magnetron sputtering consist of dense columnar structures, with a diameter of 70 to 100 nm. However, due to initial surface roughness of the mechanically polished SS316L substrate, the coating can also include exaggerated structures on the surface, which would be even more pronounced for thicker film coatings since the new crystals nucleate periodically on top of well developed grains underneath [104, 142]. These features appear to have a diameter of 150 to 200 nm and they can be seen in the top image of Figure 3.10(a), together with other smaller in-plane grains. After removal of 48 nm of Mo with deuterium exposure, these features had disappeared completely and only smaller grains are observed in the bottom image of Figure 3.10(a). The gaps between individual grains after exposures were only ~ 5 nm, which is too small to enhance the surface scattering of light (for the wavelength range from 250 to 2500 nm used in this work). For the 100 nm thick coating on the silicon wafer, where the initial surface roughness of the sample was lower (Figure 3.10(b) top), individual grains with 3 to 5 nm gaps in between can be clearly observed. After exposure (Figure 3.10(b) bottom), ~ 10 nm diameter structures with ~ 2 nm gaps (even subnanometer for nanocrystallites on the same

grain) had appeared. These are the individual crystallites forming columnar grains. This value of 10 nm coincides with the value given in Chapter 2, where the average crystallite size of 10.9 nm was calculated for the as-coated mirrors using X-ray diffraction. The appearance of individual crystallites only after exposure suggests that the crystallite boundaries had been physically sputtered more than the rest of the surface. However, a 2 nm spacing of grain boundaries is too small to enhance the surface scattering of light. The AFM topography images of the coated samples confirm that neither grain/crystallite boundary scattering nor surface roughness can account for the reflectivity drop of Mo.

The AFM image of mechanically polished single crystalline Mo with a (111) crystal orientation is shown in the top image of Figure 3.10(c), showing only some defects due to mechanical polishing. However, topographical features can be observed in the image after deuterium plasma exposure (Figure 3.10(c) bottom). It will be discussed in Chapter 4 that surface diffusion will keep the surface rather smooth againt roughening due to sputtering at the conditions used in this chapter (in fact, the surface roughness decreases after exposure for all the samples). Since this is the case, the sputtering rate should be rather constant across the surface of this sample. Nevertheless, some corrugation pattern can be generated during the early phases of physical sputtering. The appearance of the topographical features can also be explained either by a re-deposition of some of the sputtered Mo on the sample or by the fact that the top surface layers of the sample were actually not single crystalline due to the stress applied during mechanical polishing. In either case, these features are small enough not to enhance the surface scattering of light.

The SEM images in Figure 3.11 show similar changes discussed for AFM images, however with a lower lateral resolution. This proves that the all the discussed features in AFM images were real, rather than artifacts due to tip convolution or electrical noise.

3.3   Outcomes

1- Due to 200 eV D^+ exposures, the reflectivity of coated Mo mirrors will decrease initially, but attain a constant value at which it remains upon further exposure (Figure 3.1(a) and (b)). The reflectivity drop represented in Figure 3.1(c) will happen in all scenarios in ITER even after the very first shots and the optical diagnostic analyses which are dependent on FMs have to consider this change trend in the reflectivity. Moreover, it may also be an option to use already exposed Mo mirrors in ITER. This pretreatment of the mirrors would reduce the reflectivity initially (which is anyway not possible to avoid) but prevent a sudden drop in the optical diagnostics signals in the first plasma shots where the accuracy of the diagnostics signals might be very critical.

2- 200 eV D^+ exposure of coated Mo mirrors causes no significant mechanical damage like blistering of the coating or increase of the surface roughness. The reflectivity drop is due to weaker optical absorption and enhanced scattering of light, both caused by the presence of deuterium and deuterium induced defects (Figure 3.2).

3- Single and nanocrystalline Mo mirrors have the same reflectivity after 200 eV D^+ exposure, which suggests that grain boundary effects are negligible not only before, but also after exposure (Figure 3.1(d) and [11]). This, however, was not the case for polycrystalline mirrors due to different sputtering yields of different crystal orientation of Mo [3].

4- The exposures result in a Mo-D system on the surface, where the binding energy of Mo
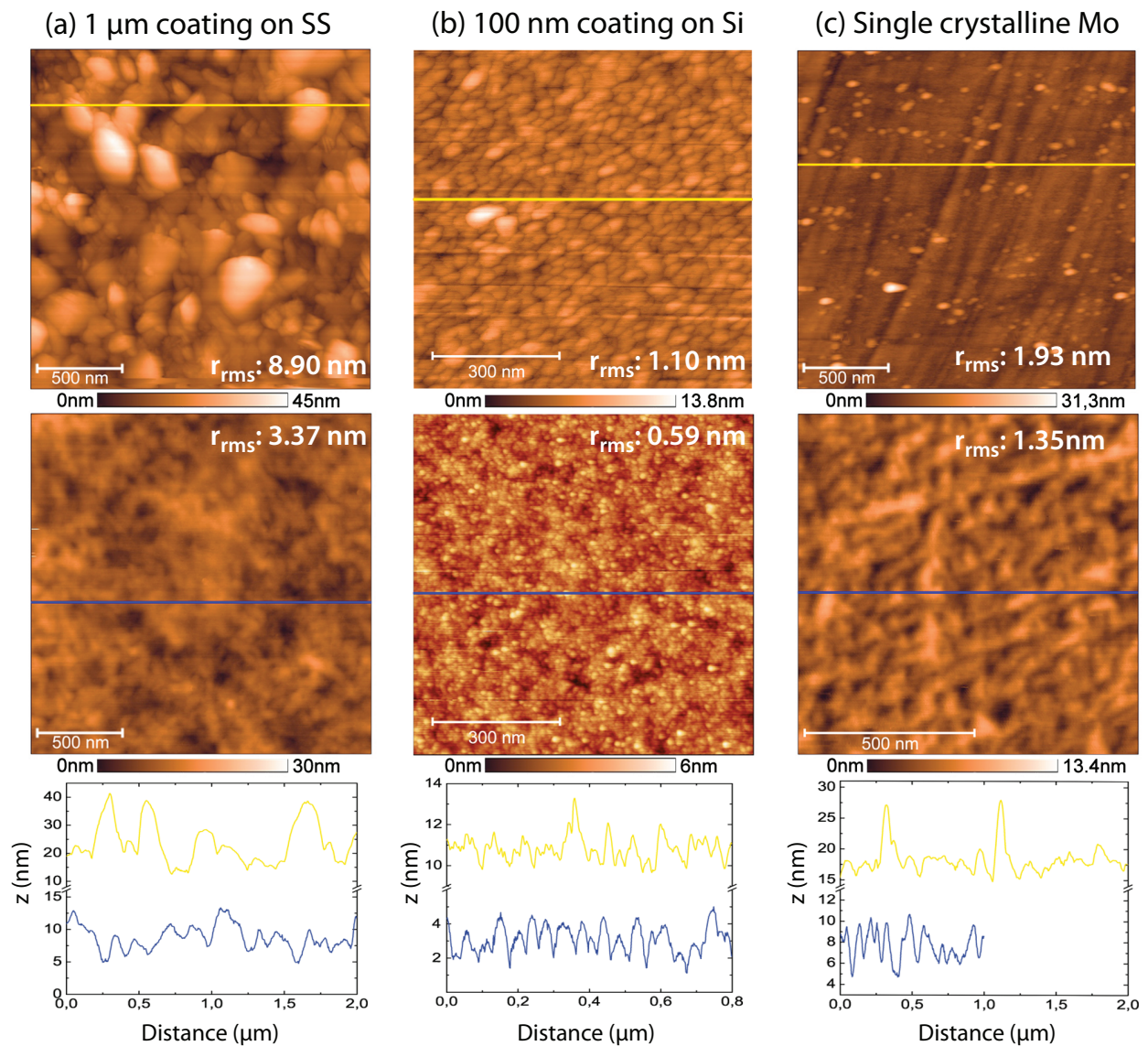
Figure 3.10: AFM topography images and line analyses of the single and nanocrystalline samples. Images in the first row with yellow line scales are the samples before exposure, whereas the second row images with blue line scales are the same samples after deuterium plasma exposure (from left to right: 1 μm nanocrystalline Mo on SS316L, 100 nm nanocrystalline Mo on Si, single crystalline Mo).

(a) 1 μm coating on SS   (b) 100 nm coating on Si   (c) Single crystalline Mo
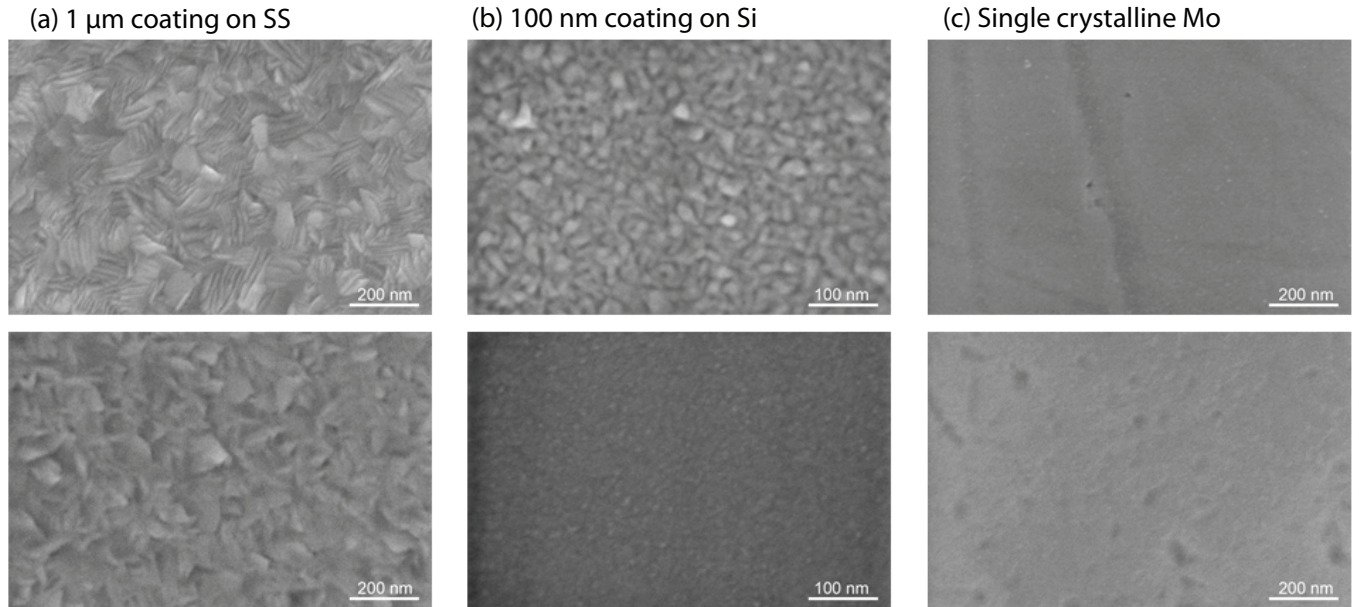
Figure 3.11: Top view SEM images of the single and nanocrystalline samples. Images in the first row are the samples before exposure, whereas the second row images are the same samples after deuterium plasma exposure (from left to right: 1 μm nanocrystalline Mo on SS316L, 100 nm nanocrystalline Mo on Si, single crystalline Mo).

3d doublet shifts 0.6 eV to higher binding energies. The reason behind such a shift is the charge carrier transfer from Mo to deuterium. This new state of Mo is stable in air and oxidation is observed to be energetically less favorable in comparison to as-coated metal Mo. This can be interpreted as a self-protecting system of the exposed mirrors against a possible oxygen or water leak in ITER.

It can be concluded with this chapter that magnetron sputtered nanocrystallline Mo mirrors are a very important candidate for ITER first mirrors and optically have no disadvantage with respect to single crystal mirrors under pure deuterium erosion conditions. Designs of optical diagnostic systems should consider modified reflection curves instead of the bulk reflectivity of Mo.

Chapter 4

Erosion of Mo with high flux deuterium plasma

This section deals with the Mo coatings, which were exposed to high flux deuterium plasma in order to test their roughening limits under erosion conditions. Higher energy of deuterium ions results in more vigorous roughening of the surface, whereas longer exposure results in only a slightly increased roughness compared to shorter exposure. Both phenomena match to the theory regarding roughening dynamics of physical sputtering. Comparison of results in this work with the previous chapter gives support to the hypothesis that roughening is flux and temperature dependent. Partial delamination of the coatings was observed upon exposure at room temperature, but not at an elevated temperature (200 °C). In summary, Mo coatings will remain functional in the ITER environment under the expected conditions. However, changes in the expected conditions such as 500 eV energy of impinging charge exchange neutrals or <100 °C surface temperature of the mirrors may lead to gradual or sudden failure of the coatings.

4.1 Experimental preparations

4.1.1 Mirror coatings

As mentioned in Chapter 2, magnetron sputtering is an energetic method resulting in dense structures with a packing fraction close to unity, which makes it a superior method for producing reflective coatings in comparison to the evaporation technique which typically produces coatings with a packing fraction below 90%. Coating rates were kept between 1.2 to 1.4 nm/s in order to obtain films in the compressive stress state [114, 115]. XPS measurements performed after the coating process without breaking the vacuum revealed only metallic Mo and adsorbed oxygen peaks without any binding between these two elements (Figure 4.7(a) and (c)).

4.1.2 Plasma exposure

Plasma exposure was performed in the DSM-2 facility at the Kharkov Institute [99, 100]. Table 4.1 summarizes the important parameters used during exposure.

45

Table 4.1: Summary of the sample names, deuterium plasma exposure parameters and delamination observations after exposure. Wide ion energy corresponds to variation of the acceleration potential between 0.1 and 1.5 kV. As presented in bold characters, no partial delamination was observed for the exposures when the sample was kept at 200 °C.

sample	temperature	delamination	ion energy	ion fluence	sputtered thickness	sputtering rate
	(°C)		(eV)	10^{19} (cm^{-2})	(nm)	10^{-5} (nm^3/ions)
Mo#4	RT	yes	60	0.56	0	0
Mo#7	RT	yes	60	1.8	0	0
Mo#12	RT	yes	200	3.0	∼40	13.3
Mo#3	RT	yes	200	6.8	∼166	24.4
Mo#8	∼100	yes	200	2.4	∼60	25.0
Mo#5	**∼200**	**no**	200	6.8	∼262	38.5
Mo#6	**∼200**	**no**	200	30	∼990	33
Mo#11	**∼200**	**no**	wide	17	∼994	58.4
Mo#13	**∼200**	**no**	50	1.9	0	0
Mo#13	RT	yes	wide	2.6	118	45.4

4.1.3 Characterizations

The total and diffuse reflectivity of the mirrors were measured using the spectrophotometer. Preparation of the coatings and the XPS measurements were performed at Facility-I.

In order to obtain information about the surface morphology of the non-delaminated Mo mirrors which were tested at 200 °C, an intermittent contact mode AFM experiment was performed by means of a Nanosurf Mobile S operated in ambient conditions.

Surface imaging and cross sectioning were performed by a scanning electron microscope (SEM) combined with a focused ion beam facility (FIB) using 30 keV Ga$^+$ ions for cutting (NanoLab 600 Helios, FEI company). The ion beam gun is tilted by 52° with respect to the electron beam. The sample surface at the cross section edge is protected by a coating layer which is deposited with a precursor processing gas of $C_9H_{16}Pt$ (Methylcyclopentadienyl [Trimethyl] Platinum) by the Ga ion beam. The layer consists of a mixture of Pt, H, C, and Ga and is around 1 μm thick (brighter unstructured upper region in Figure 4.2(b)).

4.2 Results and discussion

It is desired that the Mo mirrors retain their smooth surfaces during plasma exposure. However, there are two mechanisms which change the surface morphology of the coatings in the microscopic and macroscopic range. The microscopic changes in surface morphology appear as a milky white color of the surface, typical for highly diffusely reflecting media (Figure 4.1(b)). The macroscopic surface corrugation can also be observed by visual inspection (Figure 4.1(c)). The first (microscopic) mechanism is the physical sputtering of the surface which dynamically roughens the surface. The second (macroscopic) mechanism is the partial delamination of the coated films from the substrate and is related to temporal processes like deuterium ion flux and bulk diffusion.
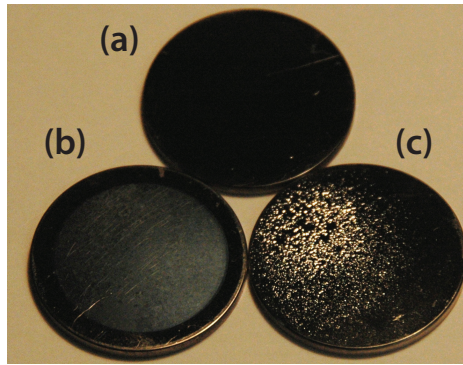
Figure 4.1: Photograph of (a) as-coated Mo mirror, (b) mirror with milky white color due to microscopic surface corrugations and (c) mirror with macroscopic surface corrugations.

4.2.1 Modifications of the surface morphology

Temperature dependent delamination

The third column of Table 4.1 gives the list of the samples, on which strong morphological changes of the Mo film had occurred during exposure to deuterium plasma. It can be clearly seen that these changes did not take place for the samples which were externally heated to 200 °C during exposure.

At first sight, optical microscope and top view SEM images (Figure 4.2(a)) suggest that the surface is blistered. Blistering is typical for polycrystalline metals, where implanted ions diffuse through the grain boundaries and get stuck between two grains, resulting in their deformation [45, 46]. Nanocrystalline coatings, however, when prepared at low temperatures consist of columnar grains (in-plane column $\varnothing \sim$ 70-100 nm) which themselves consist of individual crystallites ($\varnothing \sim$ 11 nm) [10]. Implanted deuterium can thus easily diffuse along the grain boundaries towards the surface. This reduces the dynamic deuterium inventory in the Mo and thus its tendency to blister [143, 144].

However, the features visible in Figure 4.2(a) are not the typical blisters observed in polycrystalline samples. As shown in Figure 4.2(b), the films crack at the interface. Such a delamination can occur as a consequence of excessive compressive stress in the film. As previously mentioned, the coatings were prepared with a coating speed higher than 1 nm/s in order to be in the compressive stress state which results in a high reflectivity [114, 115]. Upon exposure to the deuterium plasma at high fluxes and low sample temperatures, the deuterium concentration in the Mo layer can by far exceed the deuterium solubility. Apparently, the additional compressive stress caused by this over-saturation causes the films to buckle. In addition, deuterium can also accumulate at the coating interface, which may enhance cracking at this location.

At elevated exposure temperatures deuterium diffusion out of the sample as well as into the steel substrate occurs at a higher rate. This reduces the dynamic deuterium inventory in the film during the implantation and, thereby, the additional stress caused by this inventory. Furthermore, the thermal expansion coefficient of SS316L (typically around 1.6×10^{-5} K^{-1}) is higher than that for Mo (5.2×10^{-6} K^{-1}). The elevated temperature, therefore, partly relaxes the compressive stress in the Mo film. Finally, also the increased ductility of Mo and steel at elevated temperatures can play a role in reducing the stress at the interface by partial relaxation

due to ductile deformation. As a result, at elevated temperatures the stress in the Mo does not exceed the threshold for buckling and the surfaces appear macroscopically smooth after deuterium plasma exposure.
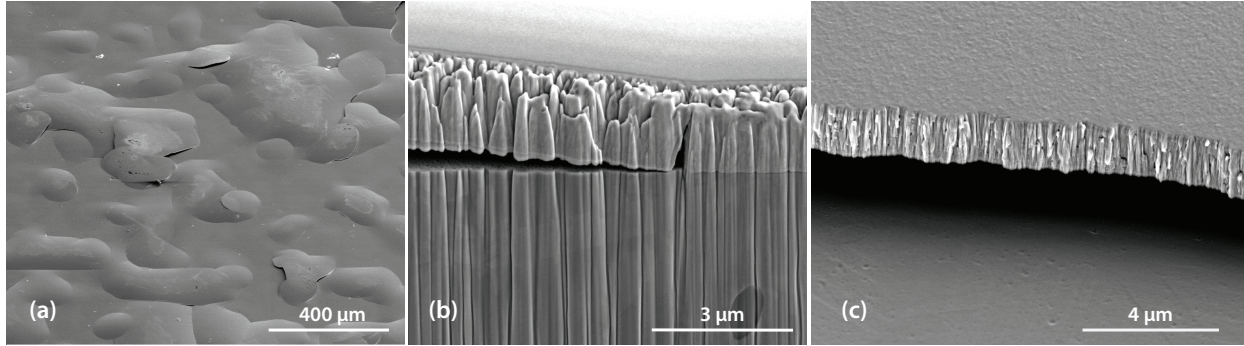
Figure 4.2: (a) Top view SEM image of a highly corrugated surface of Mo#12 after deuterium plasma exposure at room temperature. (b) Cross section and (c) tilted view SEM images clearly show that cracking occurred at the coating interface. The vertical structures in (b) are an artefact of non-ideal conditions during ion-beam polishing (the so-called curtaining effect).

The author considers such coatings with macroscopic surface corrugation as failed samples. However, since the mirrors are expected to be at elevated temperatures in ITER [4, 125], further characterizations were performed on those coatings that remained intact.

Energy dependence and dynamics of surface roughening

Samples of which the surface temperature was kept at 200 °C (Mo#5, Mo#6 and Mo#11), as expected at the ITER wall, did not show any delamination of the coated films. Therefore, these samples were further investigated in order to understand the effects of exposure time and ion energy on the microscopic surface roughening.

The samples Mo#5 and Mo#6 were exposed under the same conditions (-200 V bias and 200 °C). However, Mo#6 was exposed 4.35 times longer than Mo#5, eroding around 3.8 times more. On the other hand, Mo#6 and Mo#11 showed a similar amount of erosion, among which the energy deposition by deuterons during exposure was higher for Mo#11, which was subjected to 1.8 times less fluence than that of Mo#6. Figure 4.3 shows the topography images of these samples after being exposed to deuterium plasma. Table 4.2 summarizes the roughness values obtained from the images of Figure 4.3, and Figure 4.4 presents typical height profiles obtained from the same images. It can be seen from Figures 4.3, 4.4 and Table 4.2 that an increase of energy deposition by deuterons resulted in increased roughness, whereas the effect of the exposure time on the roughness appears to be less.

In 1988, Bradley and Harper [145] extended the sputtering theory of Sigmund [35, 36] and proposed a model explaining the periodic height generation of amorphous solids during ion bombardment. In the case of metals, the model has to be adapted to account for the higher diffusivity and non-directional character of the metallic bonds which leads to negligible amorphization [146]. It was demonstrated that crystalline quality is maintained even after prolonged sputtering [147, 148]. The Bradley and Harper model for metals for the normal ion incidence
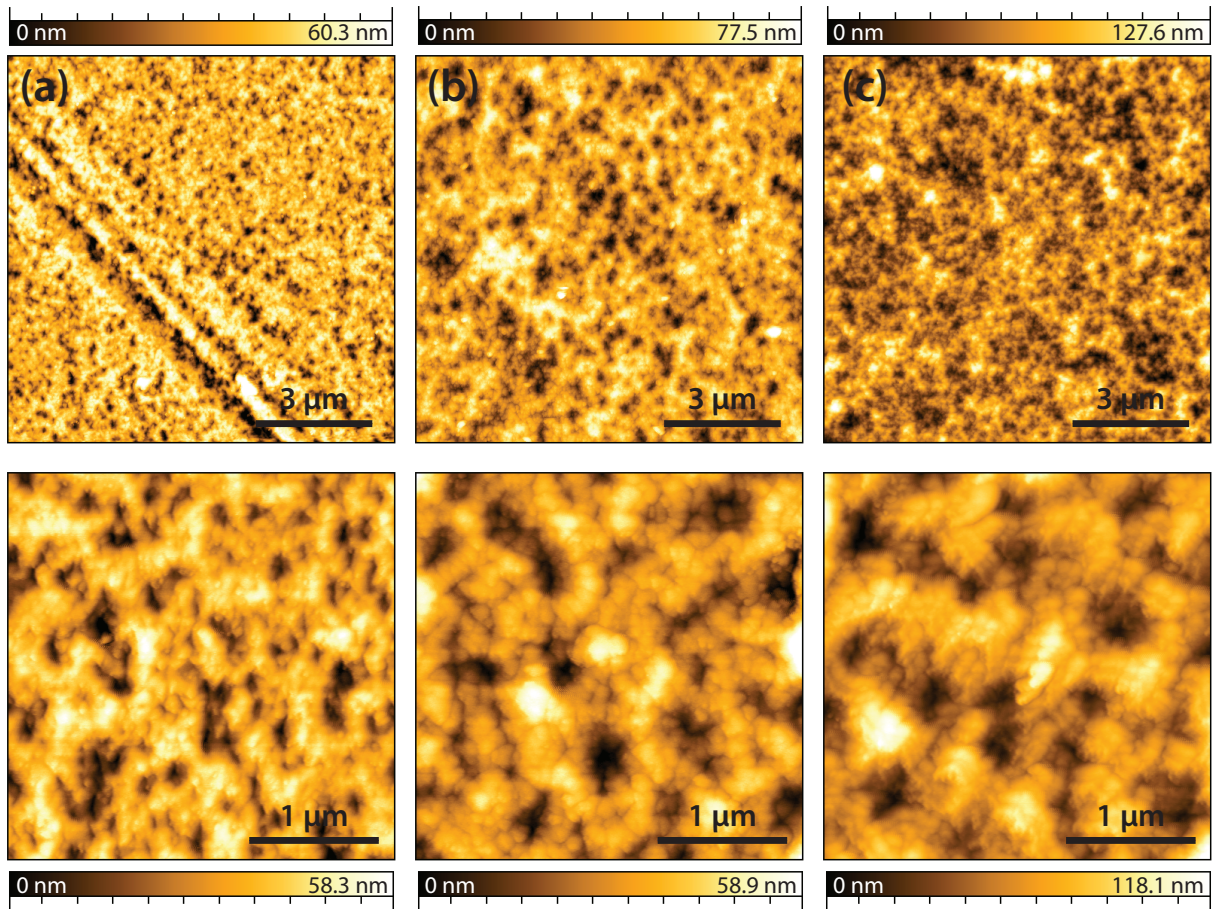
Figure 4.3: Topography images of the deuterium plasma exposed (a) Mo#5 , (b) Mo#6 and (c) Mo#11 samples obtained with intermittent contact mode atomic force microscopy in ambient conditions. Upper panel: large scale images of $10 \times 10 \ \mu m^2$. Lower panel: zoomed images of $3 \times 3 \ \mu m^2$.

Table 4.2: Summary of the surface metrology values obtained from $3 \times 3 \ \mu m^2$ images (bottom panel) of figure 4.3 presented together with the average ion energy and the eroded thickness. r_a and r_{rms} correspond to average and root mean square roughness values, respectively. r_a and r_{rms} prior to plasma exposure was 4.1 and 5.2 nm, respectively.

	r_a (nm)	r_{rms} (nm)	Average ion energy (eV)	Eroded thickness (nm)
Mo#5	7.4	9.1	200	~262
Mo#6	8.0	10.1	200	~990
Mo#11	14.3	17.9	600	~994
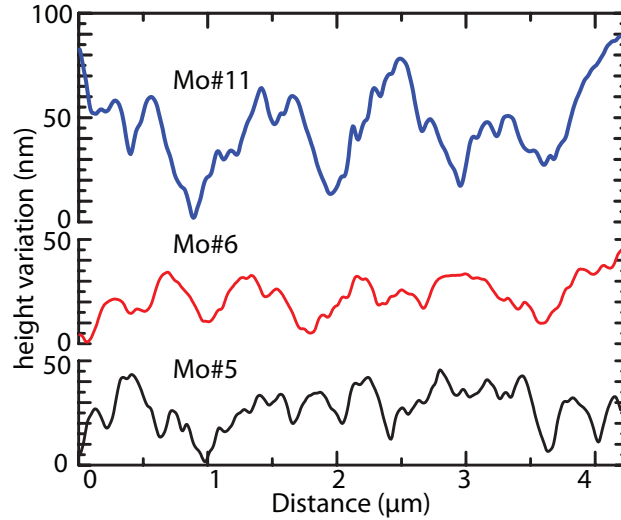
Figure 4.4: Topographical profiles obtained from 3×3 μm^2 images (bottom panel) of figure 4.3. Profile line is taken from the bottom left corner to the upper right corner of the images, with a smoothing effect due to weighted averaging of 5 pixels from both sides of the line.

can be expressed with the following formula:

$$\frac{\partial h}{\partial t} = -v_0 + \nu_x \frac{\partial^2 h}{\partial x^2} + \nu_y \frac{\partial^2 h}{\partial y^2} - D_x \frac{\partial^4 h}{\partial x^4} - D_y \frac{\partial^4 h}{\partial y^4} \tag{4.1}$$

where h(x, y, t) is the height of the eroded surface, x and y are the independent surface coordinates, t is the time, v_0 is the erosion velocity of a plane surface, ν_x and ν_y are the surface tension coefficients which depend on parameters such as the atomic volume, the uniform ion flux, ion penetration depth, sputtering yield and a coefficient governing the erosion rate dependence on the local surface curvature. For normal incidence, $\nu_{x,y}$ are negative and drives the surface to be rough. $D_{x,y}$ are the surface diffusion constants which smoothen the surface and are related to surface diffusion barriers ($E_{x,y}^D$): $D_{x,y} \propto e^{(-E_{x,y}^D/k_B T)}$. $D_{x,y}$ depend on parameters such as surface diffusivity, concentration, free surface energy, atomic volume and the thermal energy. The equation implies the following:

1. At low temperatures the surface will roughen randomly without any oriented surface morphology.

2. As the temperature increases the unstable erosion term ($-|\nu| \partial^2 h$) and the smoothening surface diffusion term ($-D\partial^4 h$) will balance, hence ripples with a wavelength of $2\pi\sqrt{2D/|\nu|}$ will be generated [149].

3. At higher temperatures, $\nu_{x,y}$ term cannot dominate over the $D_{x,y}$ term anymore and the surface will be smooth [146].

This linear model is successful in predicting the ripple formation and wavelength, but fails to explain saturation of the ripple amplitude and kinetic roughening [149]. The model has to be

extended to general Kuramoto-Sivanshisky equation which also includes nonlinear terms that provide a saturation mechanism [150–152]:

$$\frac{\partial h}{\partial t} = -v_0 + \nu_x \frac{\partial^2 h}{\partial x^2} + \nu_y \frac{\partial^2 h}{\partial y^2} - D_x \frac{\partial^4 h}{\partial x^4} - D_y \frac{\partial^4 h}{\partial y^4} + \frac{\lambda_x}{2}(\frac{\partial h}{\partial x})^2 + \frac{\lambda_y}{2}(\frac{\partial h}{\partial y})^2 + \eta \qquad (4.2)$$

where η is the noise due to randomness of the flux and $\lambda_{x,y}$ are tilt-dependent erosion rates, which are negative in the current case. Details of $\lambda_{x,y}$ can be found in Ref. [149, 152].

Of course, nanocrystalline coatings do not have a preferred crystal orientation, therefore it is not possible for oriented ripples to form. Furthermore, with the high fluences in this current work, the surface is expected to be in the kinetic roughening regime [149], which implies that the nonlinear terms would destroy the ripple structures even if they were initially formed. The morphology observed in Figures 4.3 and 4.4 is typical of the morphology obtained in the kinetic roughening regime. Nevertheless, it is possible to advocate a periodicity in the structures after the autocorrelation (autocorrelation is the cross-correlation of a signal by itself, and is a frequently used mathematical tool to disclose repeated signals obscured by noise. In surface imaging, a 2D discrete formulation is used in order to unveil hidden periodic patterns) of the $3 \times 3 \ \mu m^2$ images of Figure 4.3, which are shown in Figure 4.5. Recently, an introduction of a second nonlinear term to Eq. (4.2) was suggested by Castro *et al* [153], which depending on the ratio of the nonlinear terms may lead to ordered structures separated by defects. The use of the autocorrelation function was also suggested to visualize such patterns. For semiconductor surfaces, an ordered pattern in this regime is found to exist only for an ion energy range from few hundreds to a few thousands of eV and for temperatures below 550 K [154]. Though the parameters used in this work are in this regime, a more dedicated study is needed to explore such a behavior on metal surfaces. Redeposition of the sputtered material can also be included to Eq. (4.2) as a nonlinear term, which, however, would be not the physical mechanism responsible of the formation of the patterned structures [155].

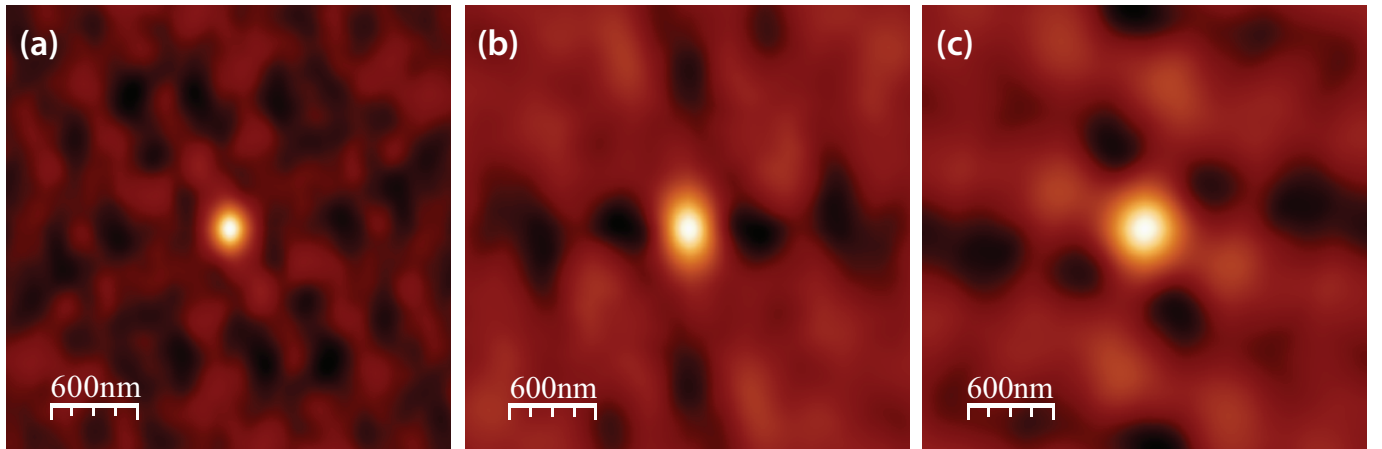
Figure 4.5: Autocorrelated images of $3 \times 3 \ \mu m^2$ images (bottom panel) of figure 4.3. (a) Mo#5 , (b) Mo#6 and (c) Mo#11. The wavelength of the periodicity is higher for Mo#6 and Mo#11 than it is for Mo#5.

The above mentioned equations are also very helpful to explain the roughness of the mirrors Mo#5, Mo#6 and Mo#11. As the energy carried by the ions increases, the sputtering yield

increases and the $\nu_{x,y}$ term starts to dominate over the $D_{x,y}$ term, which eventually leads to more pronounced surface modulations as predicted Eq. (4.1). This is the reason why Mo#11 sample has deeper trenches than Mo#6, even though same amount of material was eroded. Eq. (4.1) also implies that surface roughness has to increase as the erosion process continues, which is contradictory to the result obtained in this work, where the roughness of Mo#6 is measured to be slightly more than Mo#5. As the Mo films are exposed to deuterium plasma, a periodic structure starts to form on the surface which introduces a slope asymmetry on the surface. Such an asymmetry naturally activates the nonlinear terms ($\lambda_x \cdot \lambda_x > 0$) which decreases (even saturates) the increase in surface roughness [156]. This is the reason why Mo#6 roughness is only slightly more than that of Mo#5.

Another possible material choice for ITER FMs are single crystal Mo mirrors. Due to the non-directional nature of metallic bonds, energy dynamics regarding surface roughness generation could also be assumed to be applicable to these mirrors. This is however not really true for body centered cubic (bcc) metals which exhibit a mix of non-directional and directional (covalent) bonding, the latter originating from the quantum mechanical character of the bond [157]. Besides this fact, several other small factors also have to be considered: Eq. (4.1) requires an initial roughness for height modulation. ITER single crystal mirrors will be mechanically polished, and therefore will have a non-zero roughness values. Even if a perfect single crystal surface is considered, its atomic corrugation would initialize the above suggested surface modulations. At the initial states of roughening, some preferred ripple orientation can appear. In a long time exposure such as ITER operation, the surfaces will be in the kinetic roughening regime and therefore similar surface morphology and roughness values to those of nanocrystalline mirrors should be expected. Nonetheless, separate tests and AFM characterizations are necessary to comment on the evolution of the surface roughness of such mirrors.

The effects of roughening of mirrors Mo#5, Mo#6 and Mo#11 on their reflectivity is discussed in Section 4.2.2.

4.2.2 Reflectivity

The changes in the reflectivity can be categorized as effects which degrade the total reflectivity and effects which increase the diffuse reflectivity (i.e. reflection which is not mirror-like). The total reflectivity changes are solely due to changes in the electronic band structure of Mo due to presence of deuterium and deuterium induced defects as a result of deuterium implantation (Chapter 3). Increase of the diffuse reflectivity is due to the mechanical effects which increase the roughness of the surface of the Mo mirrors.

Effects of the electronic band structure

As a result of implantation and bulk diffusion, deuterium will be present in various forms in the Mo films. In the previous chapter, it was shown that exposure of Mo to deuterium plasma results in the degradation of Mo reflectivity due to the changes in the electronic band structure. Such a Mo/D system has a reduced density of states below the Fermi level, weakening the optical absorptions associated with interband transitions. The XPS measurements performed on the deuterium exposed samples (after storage in air) revealed a binding energy increase around 0.7 eV of the Mo 3d doublet (Figure 4.7(b)), which is attributed to reduced screening through valence band electrons on the Mo site due to charge carrier transfer from Mo site to deuterium site.
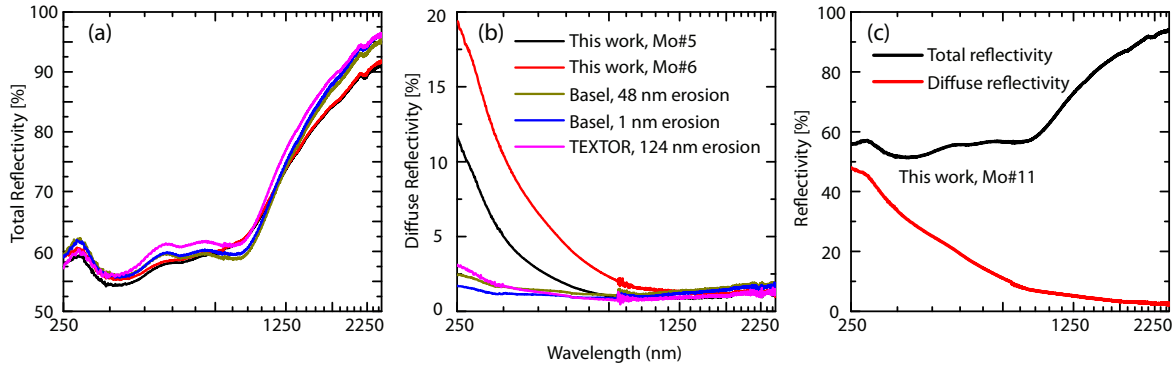
Figure 4.6: (a) Total and (b) diffuse reflectivity of plasma exposed Mo coatings when the ion energy was around 200 eV. The legends in (a) and (b) also apply to each other. (c) Total and diffuse reflectivity of a Mo coating after plasma exposure when the mean ion energy was around 500 eV. 'Basel' refers to the experiments presented in Chapter 3.

Moreover, after exposure there is also an increase of subsurface scatter events which degrades the reflectivity, especially in the infrared regime. Figure 4.6(a) shows the total reflectivity of the Mo coatings after exposure in different deuterium plasma exposure experiments. It is clear that the above mentioned phenomenon is valid both for a short, low flux (3.25×10^{15} cm^{-2}s^{-1}) exposure which results in a 1 nm erosion as well as for a high flux exposure in this experimental campaign which results in a 990 nm erosion with rigorous roughening. Since this phenomenon is not dependent of the flux, a degradation of reflectivity should be expected in the first plasma shot of ITER for all the Mo mirrors regardless of whether they are in net erosion or deposition conditions.

Effects of roughening

The effect of roughening on the specular reflectivity is often expressed with Bennett's formula (Eq. 1.5) [52]. The exponential increase in the diffuse reflectivity (Figures 4.6(b) and (c)) with decreasing wavelength can be modeled with this simple equation. The diffuse reflectivity of Mo#11 reaches almost 50% (Figure 4.6(c)) in the UV range after 1 μm of erosion, which is not acceptable for ITER. However, this sample was exposed with a wide ion energy distribution where the average ion energy was ≈500 eV. This value is higher than the edge conditions expected in most parts of the ITER wall [4, 125]. Mo#6, which also had eroded 1 μm, had a diffuse reflectivity of no more than 20%. Keeping in mind that these are very harsh but ITER-relevant conditions (high flux, high fluence), the author thinks that this is an acceptable result for certain diagnostics of ITER. However, this value is already above the acceptable limit for some modules. For instance, the diffuse reflectivity should not exceed 5% for the H-alpha diagnostics in order to obtain a high contrast image. On the other hand, average energy can reach 500 eV at certain parts of the first wall [158], implying that unprotected FMs at 200 °C will fail if placed close to those parts. Protective systems such as ducts, shutters or using a buffer gas are necessary to avoid such a scenario.

Let me also compare the current exposure with several estimated scenarios in ITER. The total ion flux in this campaign is 1.1×10^{16} cm^{-2}s^{-1}, which is comparable to the 1×10^{16}
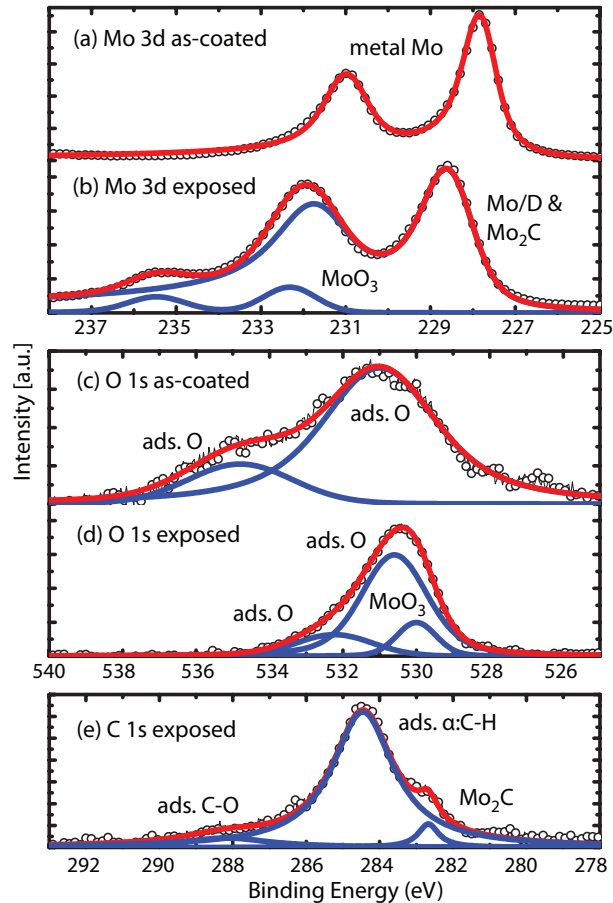
Figure 4.7: (a) Mo 3d and (c) O 1s core level XPS spectra of as-coated Mo mirrors. (b) Mo 3d, (d) O 1s, (e) C 1s core level XPS spectra of exposed Mo mirrors after storage in air. Circles are the raw data, blue curves are the individual peaks, whereas the red curves are the sum of these individual peaks. Peaks attributed to MoO_3 and adsorbed (ads.) carbon species are due to air storage. The main Mo $3d_{5/2}$ peak appears at a shifted higher binding energy of 0.7 eV. This is only slightly due to Mo_2C formation due to possible carbon impurities in the plasma. However, the main reason of this peak is the electron transfer from Mo site to deuterium site. Other peak positions are also thoroughly explained in Chapter 3.

$cm^{-2}s^{-1}$ deuterium/tritium flux expected at entrance of the equatorial ports in Ref. [129]. For the motional Stark effect diagnostics module, deuterium/tritium ion flux at the entrance of the module is estimated to be 3.6×10^{16} $cm^{-2}s^{-1}$, whereas the deuterium/tritium charge exchange neutral flux with energies above 10 eV are estimated to be 2.6×10^{16} $cm^{-2}s^{-1}$ [159]. However, for FMs which can be placed inside protective ducts, the incident particle flux can decrease at the mirror surface by several orders of magnitude [129,159,160]. The total ion flux at this campaign is in the same order of magnitude to the particle flux expected at the entrance of the ducts, and therefore reflects the worst case scenario, i.e. mirrors placed very close to the first outer wall. This scenario can actually turn out to be the reality to face, since not all of the mirrors can be placed in such protective ducts. Moreover, large discrepancies between the experiments and the calculations may not always be on our side [161]. Even for such a pessimistic outlook the mirrors will remain operational with a degradation of 20% in their specular reflectivity in the UV range. Since surface roughening is a dynamic process with saturation (Eq. (4.2)), a lifetime estimation based on a total fluence extrapolation is not considered.

Comparison to previous experiments

Table 4.3 summarizes the parameters and the results obtained in other exposure campaigns held at Facility-I (Chapter 3) and in TEXTOR [11]. Sample temperatures in both of these campaigns were elevated, and no delamination was observed. Samples which were not externally heated (80-85 °C) at Facility-I showed no delamination either [98]. This may be because of the fact that the total ion flux at the plasma exposure facility in Basel is 3.2 times lower than the ion flux used in the current chapter. As a result, the implanted deuterium in the Mo film has more time to diffuse out, hence not exceeding the solubility.

In terms of roughening, the results obtained in these two other campaigns are different from the results obtained in the current campaign. This is either because the sample temperature was higher or the ion flux was lower than the exposure in the Ukraine campaign. In the TEXTOR campaign, the sample temperature is much higher than the one used in this chapter. This would result in a higher diffusion of the surface Mo atoms, and as a result the surface tension term cannot dominate over the surface diffusion term. In the Basel campaign, the surface tension created during deuteron deposition is not high due to the low flux. Therefore, even at 150 °C the Mo atoms have enough time to diffuse laterally and smoothen the surface.

Table 4.3: Comparison of the surface roughening of Mo coatings exposed to deuterium plasma under ITER-relevant conditions. The plasma in the TEXTOR campaign has 50% hydrogen, 50% deuterium with typical impurities of 3% carbon and 1% oxygen. In the Basel campaign (Chapter 3), the rest of the ions are molecular deuterium ions.

Campaign name	Total ion flux	Total ion fluence	Eroded thickness	Energy deposition	Surface temperature	Surface roughening
	10^{15} $cm^{-2}s^{-1}$	10^{19} cm^{-2}	nm	(eV)	°C	
This chapter (Mo#6)	11.25 (82% D^+)	30	990	67-200	200	Yes
Basel	3.5 (45% D^+)	65	48	67-200	150	No
TEXTOR	- (50% D^+)	140	120	200-250	670-1240	No

What is particularly peculiar with the current exposure is that the sputtering rate is an order of magnitude higher than what is expected in literature [6]. This was also the case for

exposure of rhodium coatings in the same experimental setup [162]. In the current campaign, the background gas and plasma contains some impurities. It is also clear from the C 1s peak of the XPS spectrum which is attributed to Mo_2C, that these impurities had a certain effect on the sample surface. However, the exposure in TEXTOR resulted in a sputtering yield which is also an order of magnitude less than the current exposure, even though it also had 3% carbon impurity (The TEXTOR plasma mixture also includes hydrogen and oxygen [11], including further sputtering and redeposition channels as well as further uncertainly to the actual predominant sputtering mechanism, though the predominant reflectivity degradation mechanism is deuterium implantation [13]). The reason behind this behavior is not clear, and within the scope of this chapter the author is not going to speculate further about possible reasons of such a difference.

4.3 Outcomes

In this chapter, Mo coatings which were exposed to deuterium plasma in very harsh erosion conditions were addressed. The roughening and reflection degradation limits of such coatings were tested. In summary, Mo coatings will remain functional in most of the cases in the ITER environment under expected conditions. However, changes in the expected conditions such as higher energy of impinging charge exchange neutrals or lower surface temperature of the coatings will lead to gradual or sudden failure of the coatings.

4.3.1 Summary of precautions for ITER

1- Mo coatings which will be subject to high flux deuterium plasma has to be kept at a temperature of over 150 °C. Lower temperatures result in delamination risk.

2- Mo coatings (and maybe single crystal Mo as well) which will be subject to high ion energies have to be heated in order to enhance surface diffusion to avoid intense roughening.

Chapter 5

Properties of deuterium plasma treated Rh

5.1 Motivation

Rh, being an active catalyst in many reactions involving hydrogen, aroused interest in research between 1950 and 1970 [163–168]. From 1950 onwards, this was followed by extensive research on the interaction of protium and deuterium with polycrystalline [166, 169–171], and single crystalline Rh surfaces [172–179] in order to understand the nature of the interactions between these two materials. More recently, in the fusion community, a particular interest in the optical performance of Rh in deuterium dominated plasmas has arisen. This particular interest of the fusion community requires the extension of the previous research concerning interactions of Rh surfaces with low energy hydrogen to interactions associated with high energy ions. Such interactions involve not only the surface, but also the subsurface of Rh within the depth in which the ions lose their initial energy, or even deeper if bulk diffusion criteria can be fulfilled.

As mentioned in the introduction, nanocrystalline Rh coatings produced by magnetron sputtering are important FM canditates [15, 16]. Different from the interaction of hydrogen gas with single and polycrystalline Rh, surface hydride formation was recently reported on such coatings, which was attributed to the low coordination number of surface Rh atoms [180]. Because of the very low solubility of hydrogen in Rh [181], a stable bulk rhodium hydride has been reported only for very high gas pressures [182, 183]. Especially, x-ray diffraction results in Ref. [183] unambiguously prove hydride formation. The question arises whether a bulk effect can be observed during interactions with hydrogen plasma, since energetic ions would be implanted directly into the subsurface of Rh. Moreover, atomic hydrogen can also be incorporated into the subsurface from the grain boundaries of the nanocrystals. Would such a possible phenomenon affect the reflectivity of Rh mirrors which are planned to be used in fusion reactors?

5.2 Experimental preparations

The coating of the Rh films [15, 16], and deuterium plasma exposures were done at Facility-I, at a typical background pressure of 5 $\times 10^{-5}$ Pa. 300 nm thick coatings were prepared by magnetron sputtering on SS316L substrates (25 mm diameter, 2 mm thick), which were mechanically polished.

During plasma exposure, the Rh films were biased to -200 V and they were externally heated to 150 °C (unless otherwise stated). The total ion flux, including molecular ions, is estimated at 3.25×10^{15} cm^{-2}s^{-1}, with a 45% contribution from D$^+$. The *in situ* reflectometry system was used to monitor the evolution of $\check{R}(\phi=52\,°)$, the reflectivity between 400 and 800 nm relative to the initial reflectivity, during plasma exposure and the subsequent storage either in air or argon.

The *ex situ* UV-VIS-NIR reflectivity of the mirrors was measured before and after deuterium LTP exposure using the spectrophotometer (250-2500 nm). All the coatings prepared showed reflectivity very similar to handbook reflectivity of Rh [7]. The r_a values of the films were measured by the profilometer. The r_a measurements were done on SS316L substrates, on the coatings before and after exposure. The coating process did not result in a significant change in r_a. The surface morphology of the films was investigated by AFM topography images. r_{rms} values were extracted from these images which were taken with a Nanosurf Mobile S microscope with a Tap190-G silicon cantilever from BudgetSensors operated in ambient conditions.

Apart from the experiments on thick films, two specific electrical resistivity tests were done on thin Rh films. During these tests, the sheet resistivity of Rh was recorded without breaking the vacuum, and it was multiplied by the thickness of the Rh films in order to obtain the specific resistivity of the film. In the first test, Rh was coated on a Si(100) surface with steps of 10 nm and the sheet resistivity of the film was recorded in between each step. This way, the trend of the resistivity with increasing film thickness was obtained. In the second test, the influence of the deuterium LTP exposure to specific resistivity of Rh was investigated. In this test, ~20 nm of Rh was coated on a Si(100) surface. The sample was exposed to deuterium plasma without external heating and the applied sample bias is indicated in the results section. When a bias was applied, the estimated remaining thickness was used for specific resistivity calculation.

5.3 Results and discussion

Since the plasma is a mixture of atomic and molecular deuterium ions, an average mass of 4 amu was used for plasma characterization, which results in a plasma potential around 40 V. With this energy, TRIM simulations estimate an average implantation depth of 1.5 nm and a maximum penetration depth of ~ 5 nm [126]. The -200 V bias applied on the mirrors results in an acceleration energy 240 eV of impinging deuterium ions, which results in deuteron deposition energies of 80, 120 and 240 eV. For instance, for the deuterons with 240 eV deposition energy, the average implantation depth is estimated as 3.5 nm and a maximum penetration is estimated as ~ 11 nm (or e.g. 2.5 nm and 8 nm for 120 eV deuterons). In addition to implantation, the D$^+$ ions would physically sputter the Rh surface [6]. Both for the biased and non-biased samples, it can be roughly estimated that at least the first 4-5 nm of Rh would be heavily affected by the deuterium LTP exposure, even if the diffusion of atomic deuterium further into Rh lattice is excluded. Taking the deposition energy values as 67, 100 and 200 eV has only a slight influence in the implantation depth estimations.

5.3.1 Reflectivity degradation and recovery cycles

Figure 5.1 shows $\check{R}$ of a Rh film after exposure to a deuterium plasma with a total ion fluence of 1.6×10^{20} cm^{-2}. It can be clearly seen that the reflectivity drops during exposure and increases very slowly during subsequent storage in high vacuum. The reflectivity drop starts without any

bias being applied on the sample and the degradation accelerates when a bias of -200 V was applied. This is probably due to deeper implantation of deuterium under this condition.
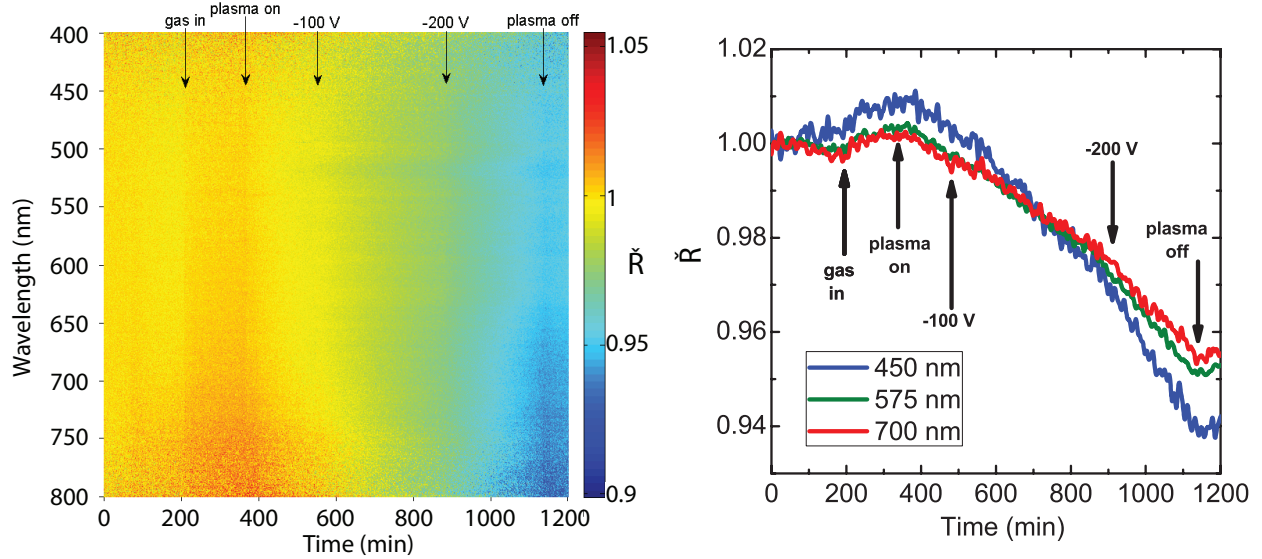
Figure 5.1: Relative reflectivity change ($\check{R}$, ϕ=52°) of Rh during exposure to deuterium plasma in the visible (400-800 nm) range.

After air (p=1 atm) was introduced into the chamber, the reflectivity started to increase very rapidly, which was then followed by a relatively slower increase (Figure 5.2). Cycles of reflectivity drop and recovery are obtained by deuterium plasma exposures and air flush. *Ex situ* measurements (not shown here) performed with the spectrophotometer showed complete recovery (less than ±0.5% change for 8 different samples tested) of the initial reflectivity after air storage, without significant increase in diffuse reflectivity. Figure 5.3 shows the AFM topography images of the Rh coating which was subjected to plasma exposure in Figure 5.1. No kinetic roughening, which would have caused a irreversible deterioration in specular reflectivity, was observed on any of the samples where the r_{rms} values remained below 2 nm. Similarly, no significant change in the r_a values was observed after exposure in the measurements performed with the alpha stepper.

Palladium (Pd) is another platinum group metal, which is well known to form a hydride in hydrogen atmosphere. In the case of Rh, this is only possible with very high pressures [182, 183] due to the very low solubility of hydrogen in Rh [184]. In literature, it was already reported that palladium hydrides (PdH$_x$, x≤1) have different optical constants than Pd [185]. Furthermore, very similar reflectivity drop (hydrogen loading) and recovery (hydrogen unloading) cycles were reported [186]. With this in mind, it can be anticipated that Rh is also forming a hydride as a result of interactions with deuterium LTP, in a similar manner to Pd. As in the case of PdH$_x$, rhodium hydride is metallic Rh with a substantial amount of hydrogen within its crystal lattice and is a pseudo-alloy presented with a chemical formula of RhH$_x$ (RhD$_x$ when deuterium isotope is considered), where H≤2. In the case of Pd, hydrogen loading and unloading require neither plasma creation nor air dosing, and can be achieved by hydrogen dosing cycles. In terms of the change in the reflectivity, the following question has to be answered: Is the reflectivity change
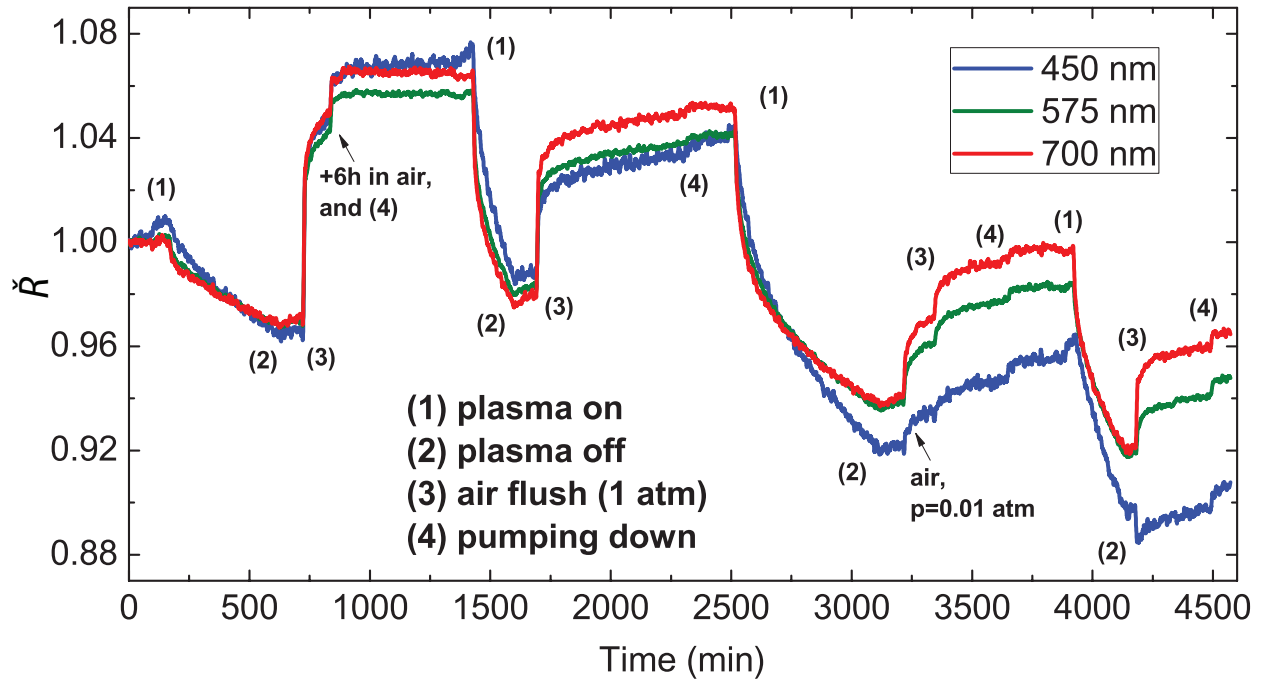
Figure 5.2: Relative reflectivity change ($\check{R}$, $\phi=52°$) of Rh during four cycles of exposure to deuterium plasma (1), storage in vacuum (2), storage in air (3) and repumping the chamber (4). In a similar manner, Figure 5.1 represents one cycle of steps (1), (2) and (3).
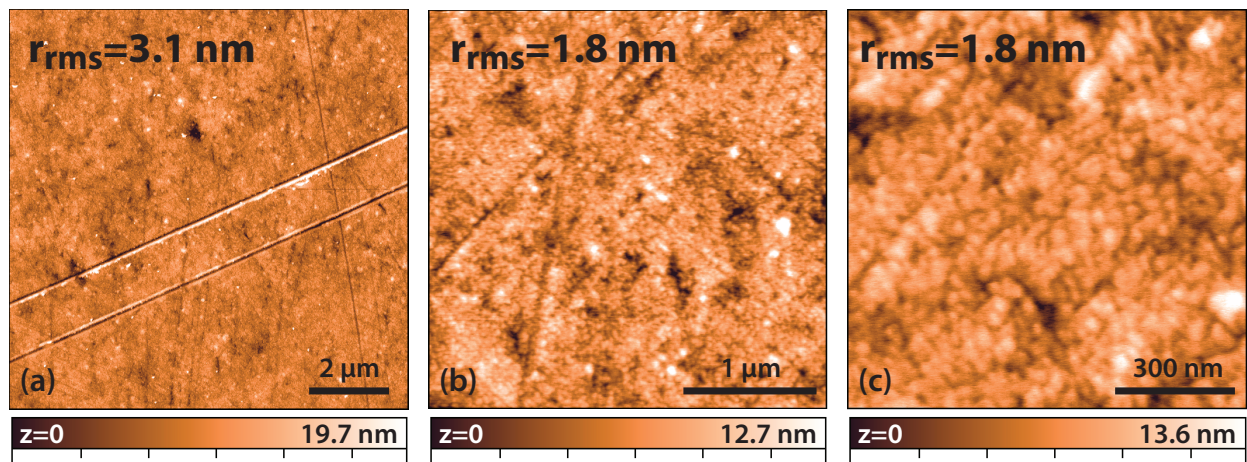
Figure 5.3: (a) 10×10 μm^2 (b) 3×3 μm^2 and (c) 1×1 μm^2 AFM topography images of the Rh coating which was subjected to deuterium plasma exposure in Figure 5.1. The roughness is only due to initial effects: 1- Grain boundaries. 2- The straight lines which are traces of the mechanical polishing of the stainless steel substrate. In (a), such lines increase r_{rms} to 3.1.

solely due changes in the electronic band structure caused by deuteride formation, or is it also due to the introduction of new scattering centers in the form of impurities and defects? A possible contribution from scattering is investigated with surface resistivity measurements in Section 5.3.2, whereas the electronic band structure is investigated with XPS and UPS measurements in Section 5.3.3.

Besides the clear cycles of reflectivity decay during plasma exposure and subsequent recovery upon exposure to air, an overall decline of the reflectivity is also apparent in Figure 5.2. In addition, the decline is stronger in the blue region of the spectrum than in the red. Although a definitive explanation of this phenomenon eludes the author at present, it is safe to say that the roughness is too small to account for the effect and it may be postulated that a complete recovery would have been obtained eventually after sufficiently long exposure to air. Even when the gradual decrease should prove to be technical in origin, the qualitative, cyclic features remain.

Two additional tests were performed to demonstrate that the sudden reflectivity changes are not due to thermomechanical instabilities of the setup. In the first test, in which SS316L and Mo samples were used instead of Rh, no reflectivity recovery was observed after air flush. Moreover, unlike in the case of Rh, the *ex situ* reflectivity measurements of these two samples revealed similar values as the *in situ* measurements [98]. In the second test, in which an exposed Rh sample was stored in argon, the reflectivity recovered very slowly, just as it did in vacuum. These two tests show that the reflectivity drop and recovery cycles are dependent on the material which is being exposed and the gas which is used for flushing the chamber; therefore not due to the measurement system itself.

Interestingly, it can also be observed that deuterium gas introduction into the chamber results in a small increase in the reflectivity. This might be an effect related to adsorption of hydrogen or desorption of air contaminants, though speculation as to the origin of this phenomenon is outside the scope of this thesis.

5.3.2 Specific resistivity during exposure

In literature, the change in the specific electrical resistivity (ρ) has often ben used as an indicator of hydride formation. In the case of PdH_x formation, the data vary from a prominent drop of the resistivity [187] to an order of magnitude increase [188]. This case may be different from the RhH_x case, since excess lattice expansions and contractions during loading/unloading cycles lead to permanent damage. It is, therefore, important to recall the origin of resistivity in metals before evaluating the effect of the LTP exposure on Rh films.

The specific electrical resistivity of thin metal films has three main components. The first component is the resistivity inside the crystal grains of the film due to isotropic background scattering (electron scattering by phonons and point defects), i.e. the bulk resistivity if a single crystal metal is considered. The second and third components originate from grain boundary and surface scattering, which scale inversely with grain boundary diameter and film thickness respectively [118, 189]. With a sufficient film thickness (d) the effects of surface scattering can be diminished, and a ρ of 260 nΩ·m was obtained for the thin Rh films for a thickness greater than 30 nm (Figure 5.4 inset). This value is higher than the values obtained for thick films (85 nΩ·m [190], 120 nΩ·m [191], bulk resistivity of Rh 45 nΩ·m [192]). This is probably due to the facts that no surface scattering takes place in thick films and grain boundary scattering gets diminished due to well-structured grains. For lower d values, ρ scales linearly with decreasing

thickness due to the increasing effect of surface scattering (Figure 5.4 inset). A typical approach when presenting the results is plotting $\rho * d$ vs. d, which will exclude the surface scattering term. In the Rh coating used in this work, a linear trend can be observed (Figure 5.4 black line); suggesting that isotropic background scattering and grain boundary scattering are invariant between a d of 10 to 70 nm. Recall that this coating was done in steps of 10 nm, in order to obtain similar grain sizes for each measurement.
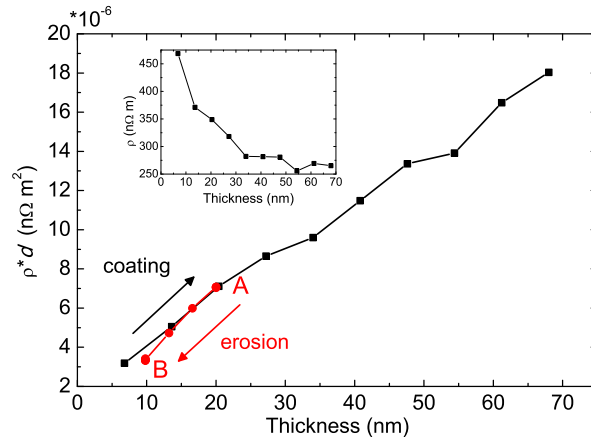
Figure 5.4: $\rho * d$ vs. d plot of a Rh coating with steps of 10 nm (black) and of a Rh coating when biased to -200 V and exposed to a deuterium LTP (red). Point A represents the constant $\rho * d$ value during exposure without any bias applied to the sample. Point B represent the constant $\rho * d$ value after the exposure, during storage in vacuum and in air.

For the exposure test, a 20 nm Rh coating was prepared which had a ρ of 353 nΩ·m. When this film was exposed to deuterium LTP without any bias applied to it, no change in ρ was observed. In other words, the $\rho * d$ value stayed constant at point A on the red line of Figure 5.4 for a 4h exposure, where the surface resistivity was measured each hour. For the second part of the exposure test, a bias of -200 V was applied to the sample. This bias is estimated to lead to an erosion rate of 3.4 nm/hour. This estimation was done by means of weight loss measurements performed with a Mettler M 3 micro balance (with 1 μg repeatability). The $\rho * d$ vs. d trend obtained during erosion of the film (red line) is very similar to the trend during the coating (black line). Moreover, ρ stayed constant during storage in vacuum and afterwards in air. These results mean that the $\rho * d$ value of the films does not depend on the possible effects of the plasma exposure or air storage, and is only dependent of the thickness of the Rh film. In other words, the deuterium LTP exposures, with or without bias, has no noticeable effect on the density of the scattering centers of the Rh films. This would also mean that other scattering mechanisms such as defect or impurity scattering were not introduced during exposure. Accordingly, it can be concluded that deuterium is not strongly bound to defect sites, and is rather evenly distributed in the Rh lattice.

In the Drude theory of metals, the dc resistivity is inversely proportional to the intraband relaxation time, based on the assumption that the same scattering mechanism holds for electrons in response to dc and optical fields. Therefore, given that the resistivity was found to be invariant, the change of the reflectivity cannot be attributed to a new scattering mechanism induced by the LTP exposure.

5.3.3 XPS and UPS before and after exposure

In the survey XPS spectra of the films after preparation and after exposure (Figure 5.5(a)), no impurity peaks such as oxygen or carbon were observed. XPS is not sensitive to direct detection of hydrogen. Both after coating and exposure, only Rh peaks were observed, which precludes any possible interpretation of the results in terms of surface contamination effects.
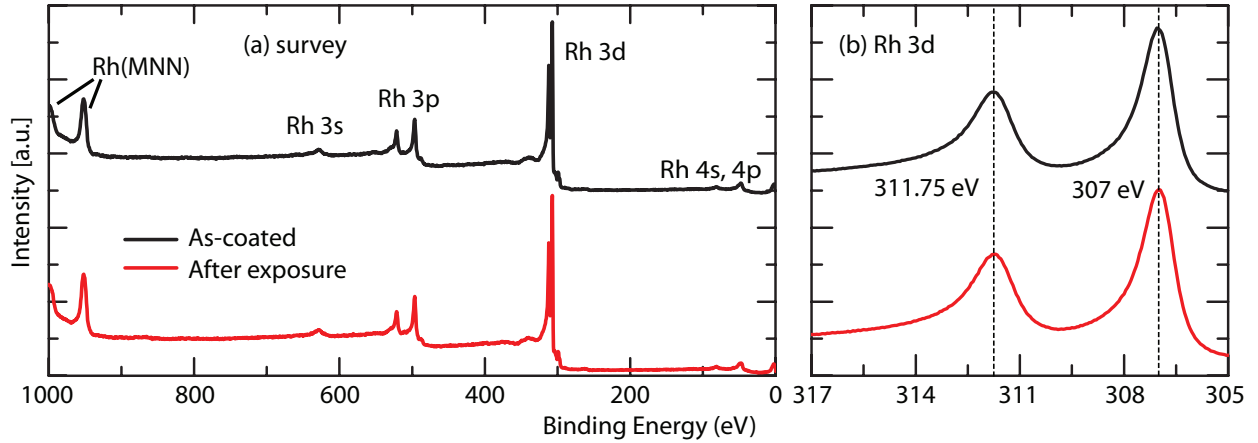
Figure 5.5: XPS (a) survey and (b) Rh 3d spectra before and after exposure to deuterium plasma.

The top panel of Figure 5.6 shows the HeI UPS spectra of as-coated Rh at 3 different polar angles (i.e. the angle between the entrance slit of the analyzer and surface normal). Since the nanocrystalline films do not have any specific texture, the UPS spectrum does not reflect a particular crystal orientation, but rather is an average of all orientations present. On account of this, different angles correspond to different sampling depths. For instance, it was recently reported for noble metal coatings that the measurement geometry can have an influence on the measured valence band spectra [193]. At normal incidence, the UPS spectrum near E_f consists of two bulk Rh 4d peaks (Figure 5.6, B peaks), whereas for higher polar angles these two peaks appear as a single peak and the peak just below the Fermi edge (Figure 5.6, C peak) gets sharper. Both phenomena are somehow related to the fact that the photoemission process is taking place closer to the surface for higher polar angles.

After exposure (Figure 5.6 bottom panel), the work function of the Rh surface increases around 0.3 eV (shown with line A and also (a)-magnified), which is attributed to deuterium adsorbates heavily populating the Rh surface during plasma exposure [173, 180]. Surface deuteride formation might also take place [180]. The spectra after exposure retain the general characteristics of Rh, however they exhibit some small differences from the spectra before. The most important change is decrease of the relative intensity of peak C and the gain in the relative intensity of the nonbonding d-band peak (Figure 5.6(b) and (c)). A similar change was reported for Rh/Si alloys [194, 195], which was more prominent for that case. This phenomenon can be explained as follows:

Rh DOS calculations reveal an intense unfilled peak just above E_f [196, 197]. This can also be suspected from Figure 5.6(b) and (c), since the most intense peak is the one closest to E_f. The DOS below the E_f could increase if there is a positive shift (negative in terms of binding
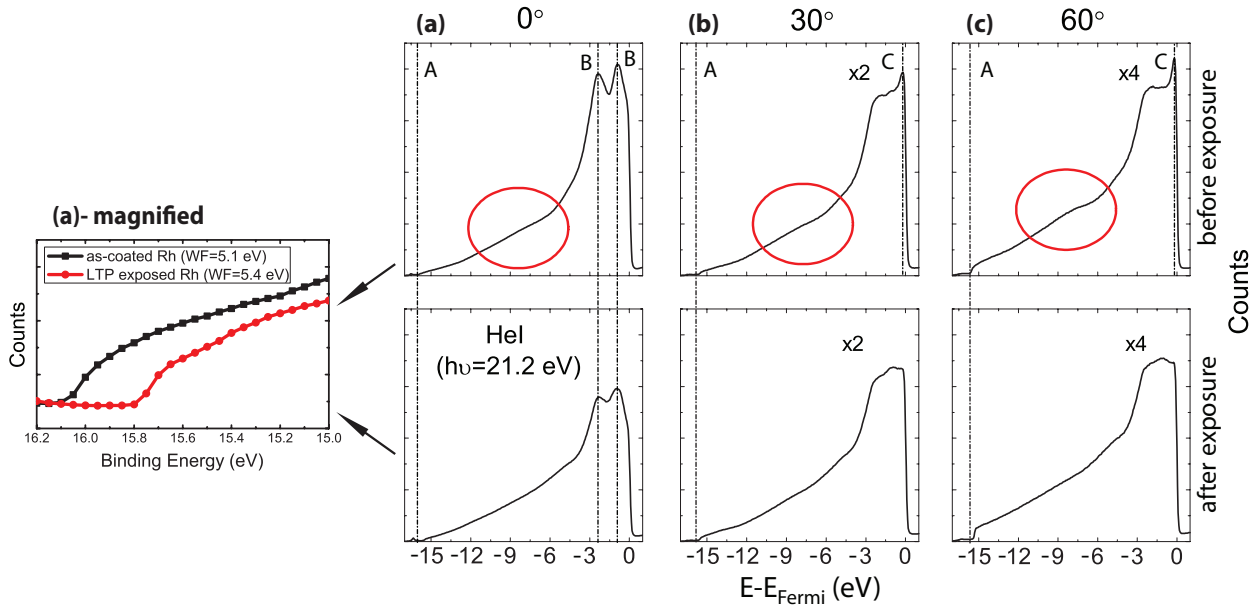
Figure 5.6: Valence level UPS spectra of Rh at polar angles of $0\,^\circ$ (a), $30\,^\circ$ (b) and $60\,^\circ$ (c) before (top panel) and after (bottom panel) deuterium LTP exposures. Eyeguide lines A, B, C are provided to show the cut-off, filled 4d states and the peak close to the Fermi edge of as-coated Rh respectively. (a) is magnified around the cut-off, in order to present the change in the work function clearly.

energy) of the E_f as the d-band gets filled with more electrons. In RhH_x DOS calculation in Ref. [198], such a change is expected to exist upon hydride formation. It can be assumed that the structure of the Rh matrix is maintained to a large extent, since the maximum unit-cell volume expansion has been measured to be 21.2% [183]. Let me also assume that the Rh/D has no or negligible covalent character. In this case, one can think of rigid-band filled with electrons from deuterium, where this electron donation would cause relative increase of DOS just below the E_f and relative decrease of DOS above E_f. Such a change would manifest itself as decrease of the relative intensity of the peak close to the Fermi edge, and increase of relative intensity of the nonbonding d-band peak in broadened DOS, exactly as it is in the UPS spectra of Figure 5.6. Such a Rh/D system describes an alloy formation between Rh and deuterium, which is defined as RhD_x.

Changes in the reflectivity may be understood from the discussion above: Deuterium donates electrons to Rh which shifts the E_f to the tail of 4d peak which was initially unfilled. As the number of states above the E_f decreases, optical transitions reduce and the reflectivity drops. The same phenomenon has already been explained for Pd/H system in Ref. [199].

Contrary to the above discussion regarding the UPS spectra, no significant change in the shape and position of the core level Rh 3d peaks were observed after LTP exposure (Figure 5.5(b) for $0\,^\circ$, also valid for $30\,^\circ$ and $60\,^\circ$). Even for Rh/Si alloys [194] where the changes in valence band structure was much more pronounced than Rh/D case, the change in the Rh 3d B.E. was reported as only -0.1 eV. Probably, a relaxation due to increase of DOS below E_f would not be that effective as in the case of Rh/Si and a possible negative shift would be below the detection

limit of the analyzer. In the case of Pd, the story is different. Pd has an atomic electronic configuration of 4d10, and therefore the nonbonding d-band will be completely occupied even for little electron transfer. As a result, a shift of 0.3 eV to higher B.E. is typical for the Pd/H system [140].

Two other changes can also be observed in the UPS spectra after exposure: (i) The bumps shown in red circles in Figure 5.6 disappear after exposure. This may be due to some smaller changes in the electronic structure as a result of deuteride formation. Alternatively, it may also be due to less number of secondary photoelectrons, which originate from inelastic scattering from filled bands to unoccupied bands during photoemission process. As the d-band gets slightly more filled by the electrons donated from deuterium, in a way analogous to reduction of reflectivity, there are less states where these electrons may scatter into. (ii) The UPS spectra have lower number of counts after exposure, which can also be attributed to the E_f shift. Similar to reflectivity, valence band photoemission spectrum is also governed by the Fermi golden rule, requiring optical transitions of the photoelectrons to unoccupied states. The reduction of joint DOS measured in the UPS spectra implies a reduction in the imaginary part of the complex permittivity, $\epsilon 2$, hence a reduction in reflectivity for all visible spectrum.

After introduction of air into the chamber, the Rh surface gets populated with an unknown amount of hydrocarbon, hydroxide and water adsorbents and possibly slightly oxidizes as well. This makes UPS spectra after air storage rich in contributions from oxygen and carbon, and therefore not conclusive about the recovery process.

5.4 Overview

The reflectivity drop of a metallic sample can be explained by presence of another element, either in the form of a compound (e.g. oxides or nitrides) or in the form of an alloy with another metal. No element other than Rh was present in the XPS spectra after exposure, which rules out the possibility of a compound or a non-hydride alloy formation. Another possible explanation is the introduction of defect or impurity sites in the metal subsurface which either introduces scattering centers or changes the electronic structure of the metal, which was reported in Chapter 3. The authors thinks that this phenomenon is also not the case here, since (i) such a change in the electronic structure would have manifested itself as broadening of XPS and UPS peaks, (ii) the reflectivity would not be recoverable by storage in air, (iii) the resistivity would not be invariant to new scattering centers. It is also not possible to attribute the reflectivity changes to surface damage, since such a change would be observed as increase of roughness and would also be detected in *ex-situ* reflectivity measurements (more to this point, the *in-situ* reflectivity would not be reversible). The only possible explanation is that the newly formed Rh/D system has a different electronic structure than Rh, which is supported by the changes in the UPS spectra. Such a Rh/D system can be interpreted as RhD_x formation. In literature [182, 183], rhodium hydride formation was only observed at very high pressures of hydrogen due to the very low solubility of hydrogen in Rh. However, in the current case the energetic ions can simply be implanted into the Rh lattice. Moreover, atomic deuterium may also be incorporated into Rh from the grain boundaries of the nanocrystals.

The impinging deuterium ions get implanted into the subsurface layers of Rh (Figure 5.7(b)). These ions are not strongly bound to defect sites and rather are evenly distributed in the fcc lattice of Rh. This creates a RhD_x thin film on the Rh surface, which has different optical

constants than those of pure Rh (Figure 5.7(c)). As a result, reflectivity drops. The Rh surface is heavily populated with deuterium adsorbates and possibly with some surface deuterides, which result in a 0.3 eV increase in the work function. When the plasma is stopped and the chamber is evacuated, the adsorbates stay on the Rh surface. As a result, the interstitial deuterium diffuses very slowly to the surface and the reflectivity recovery is very slow (Figure 5.7(d)). Upon air flush, catalytic reaction between deuterium and oxygen occurs [163], and the adsorbates are released rapidly to air (Figure 5.7(e)). This is followed by the diffusion of deuterium from the subsurface first to the surface and then into the air, resulting in the recovery of the electronic structure and of the reflectivity of Rh after air flush (Figure 5.7(f)). Such a recovery would not be possibly if deuterium were strongly bound to defect sites.

5.5 Outcomes

1. Deuterium LTP exposure of Rh films results in a reversible degradation of the reflectivity. The author thinks that RhD_x may be forming as a result of this exposure on Rh coatings. In this scenario deuterium (and presumably protium would also) acts as an electron donor, filling the Rh 4d states above E_f. As a result, the number of states above E_f reduces, causing reduction in optical transitions and consequently decrease in reflectivity of Rh. Therefore, deuterium LTP exposed Rh has different optical constants than those of as-coated Rh.

2. Deuterium LTP exposure of Rh films results in a reversible degradation of the reflectivity. The author thinks that RhD_x may be forming as a result of this exposure on Rh coatings. In this scenario deuterium (and presumably protium would also) acts as an electron donor, filling the Rh 4d states above E_f. As a result, the number of states above E_f reduces, causing reduction in optical transitions and consequently decrease in reflectivity of Rh. Therefore, deuterium LTP exposed Rh has different optical constants than those of as-coated Rh.

3. If Rh is used as a mirror material in future fusion reactors, the reflectivity will degrade. The plasma in these reactors will also contain impurities such as C, W and Be. Further research is necessary in order to conclude if RhD_x can grow under these conditions.
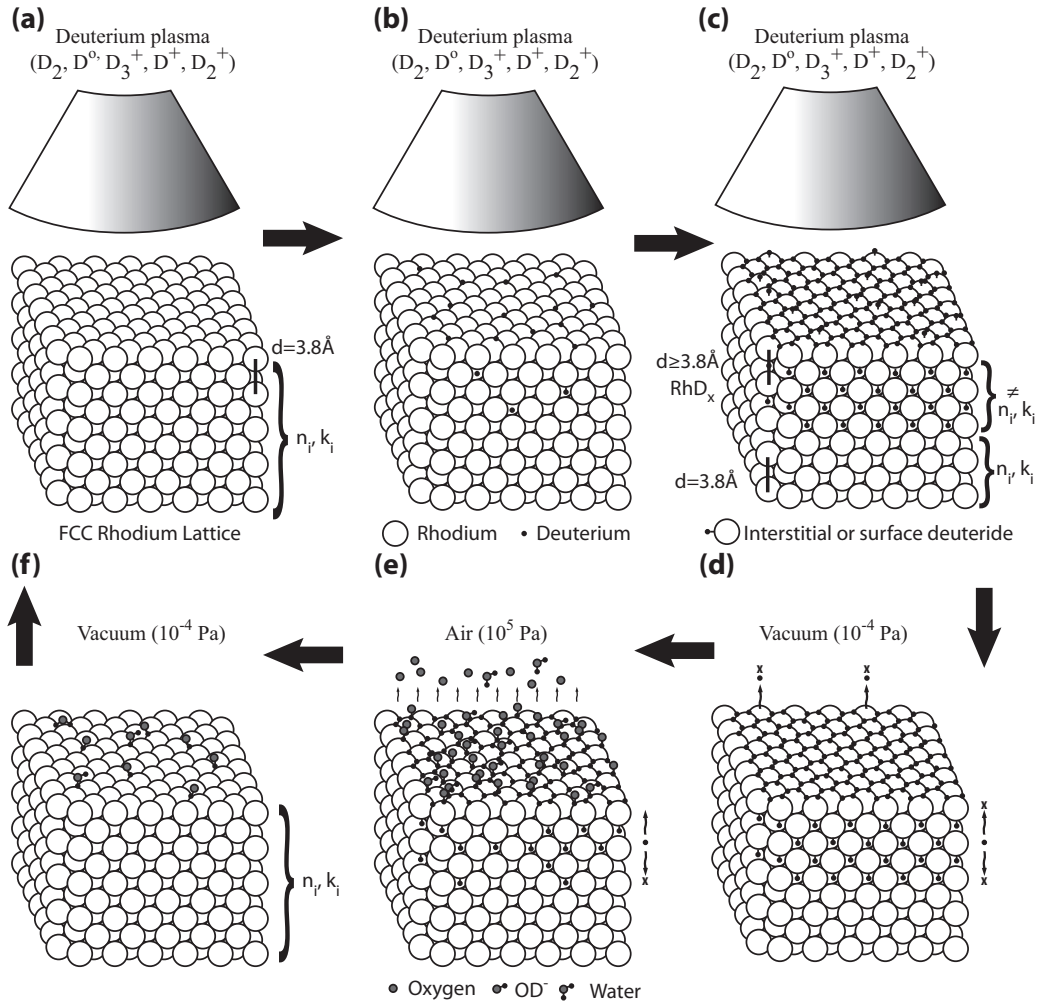
Figure 5.7: The overview of the surface and subsurface interactions taking place between deuterium plasma and fcc Rh lattice (a). Deuterium gets implanted and forms interstitial subsurface deuterides as well as being adsorbed on the surface. Surface deuteride formation is also possible (b, c). Surface adsorbates remain during vacuum storage (d). However during air storage, the adsorbates react with oxygen and leave the surface followed by diffusion of deuterium from subsurface into the surface and then to the air (e) until deuterium is completely removed from Rh subsurface (f).

Chapter 6

Introduction of typical impurities (W, Al, C) into deuterium plasma

Since the ITER plasma will consist mostly of deuterium, special attention was already given in Chapters 3 and 5 to understand how Mo and Rh surfaces would behave during pure deuterium plasma exposure. However, erosion of plasma facing components will cause impurities such as W, Be and C to enter the ITER plasma, where depending on the local plasma parameters FMs may be subject either to erosion or deposition. The actual amount of C impurity will depend on the choice of the divertor (a part of a tokamak) material, where the current choice is in the favor of not using any C [200]. At the University of Basel, it is not allowed to work with Be because of its toxicity. Therefore Al was employed as a replacement for Be due to the chemical similarities between these two metals.

In this chapter, several possible plasma mixtures relevant to ITER which includes W-C and W-Al impurities were produced, while monitoring the *in situ* reflectivity of the mirrors, which had been prepared by magnetron sputtering coating. It was aimed to experimentally simulate the effects of such impurities on the chemical composition of the mirror surface, and on the reflectivity accordingly.

6.1   Can Al replace Be?

The toxicity of Be prohibits its use in the experimental facilities at the University of Basel, as well as many others including majority of the tokamaks. A possible solution may be to use Al as a surrogate of Be [201]. Since the electronegativity of Al is similar to Be, they form similar oxides and hydrides. In this respect, Al can potentially replace Be. In terms of the chemical properties of their oxides, the most important difference appears in diffusion. Contrary to Al_2O_3, BeO layers allow diffusion of Be through the surface oxide layers above 600 °C [202]. For lower temperatures, Al is a very good substitute for Be when the interest of research is chemical modifications (such as the current case). Table 6.1 summarizes the most important chemical properties of Al and Be [201]. In terms of physical properties, Al lacks similarities with Be: Its melting temperature is 600 °C lower than that of Be, has a different cubic structure from Be, and has different sputtering yield from Be due to the difference in atomic mass.

Table 6.1: Chemical properties of Al and Be. The most important properties are written in bold characters.

	Al	Be
Oxidation states	+3	+2
Atomic radius (nm)	0.143	0.112
Ionic radius (nm)	0.68	0.59
Charge: ionic radius	4.4	3.4
Electronegativity (Pauling scale)	**1.61**	**1.57**
Oxide	**Al_2O_3 Wurtzite structure** Melting point: 2072 °C Density: 4 g/cm^3 trigonal	**BeO Wurtzite structure** Melting point: 2072 °C Density: 3.01 g/cm^3 hexagonal
Hydride	**Covalent bonding $(AlH_3)_x$** Melting point: 150 °C Density: 1.48 g/cm^3 α-Alane has a cubic or rhombohedral structure	**Covalent bonding $(BeH_2)_x$** Melting point: 250 °C Density: 0.68 g/cm^3 hexagonal crystalline form
Alloys with W	$Al_{12}W$, Al_5W, A_4W	Be_2W, $Be_{12}W$, $Be_{22}W$
Alloys with Mo	Al_7Mo, $Al_{12}Mo$, Al_5Mo, Al_4Mo, Al_3Mo, Al_8Mo_3, $AlMo_3$	$BeMo_3$, Be_2Mo, $Be_{12}Mo$, $Be_{22}Mo$
Alloys with Rh	Al_5Rh_2, $AlRh$	Be_7Rh, $BeRh$

6.2 Experimental preparations

The experiments were conducted at Facility-I. As illustrated in Figure 6.1, two magnetrons were mounted to the experiment chamber vertically, such that they can act as W and Al impurity sources. The deuterium pressure was fixed to 3 Pa, whereas the methane (CH_4) pressure was varied (acting as the C impurity in deuterium). No additional gas (e.g. argon) was necessary to start the magnetrons (even without CH_4 addition), and the impurity influx was controlled by changing the pulsed-DC power applied to them. A drawback of the system in these conditions including impurities, is that the viewports are also coated slightly during experiments, resulting in overestimation of the reduction in reflectivity. Industrially prepared Mo and Rh mirrors [203] with handbook reflectivities [7] and with diameter Ø=25 mm were tested. A 150 °C mirror temperature and a 200 eV particle energy are the expected wall conditions in ITER [4, 125]. Therefore, the substrates were heated to 150 °C by resistive heating and biased to -200 V during plasma exposure
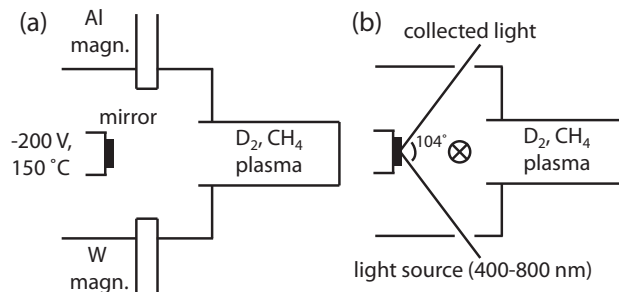

Figure 6.1: Cross-section (a) and top-view (b) sketches of the experiment chamber of Facility-I which is built around 2 magnetrons, one RF plasma source and an *in situ* spectral reflectometer.

Table 6.2: List of samples, plasma exposure time, impurities added into deuterium and the atomic concentrations of Mo and Rh mirror surfaces after plasma exposure. Atomic concentrations of compounds are given as the sum of concentration of the individual atoms (e.g. Mo_2C is 67 % Mo and 33 % C at binding energies of 228.3 eV and 283.3 eV, possible Al-enrichment of Al_2O_3 is not considered). 1h of plasma exposure time corresponds to a D^+ fluence of 5.6×10^{18} cm^{-2} [13]. CH_4 amount is given as its partial pressure percentage. W and Al impurities are represented as pulsed-DC power applied to magnetrons as Watts (W stands for Watt and not tungsten in this case). Abbreviations mag., ox., a-C:D and ads. refer to magnetron, oxides, amorphous hydrocarbon (probably deuterized) and adsorbed oxygen species (e.g. heavy water, DO^-), respectively.

		Impurities			Atomic concentration of the surface								
	exp. time	W mag.	Al mag.	% CH_4	Mo Mo/D	Mo_2C	Rh	W & W/D	W_2C & WC	W ox.	Al ox.	a-C:D	ads. O
Mo#1	7h02'	110W	off	3.3	-	-	-	-	48	-	-	52	-
Mo#2	5h49'	110W	off	3.6	-	33	-	-	18	-	-	47	2
Mo#3	4h15'	110W	off	1	-	54	-	-	7	10	-	26	3
Mo#4	4h36'	110W	off	2.5	-	55	-	-	6	6	-	30	3
Mo#5	3h41'	110W	35W	0	23	-	-	4	-	5	60	-	8
Rh#1	6h17'	110W	off	3.5	-	-	16	-	29	-	-	55	-
Rh#2	3h51'	110W	off	4.95	-	-	70	-	6	-	-	24	-
Rh#3	4h47'	40W	off	8.3	-	-	53	-	8	-	-	39	-
Rh#4	2h13'	110W	60W	0	-	-	2	-	-	4	86	-	7
Rh#5	4h33'	110W	36W	0	-	-	6	-	-	9	77	-	8

6.3 Results and discussion

Table 6.2 lists the plasma exposure time and the impurities added to the plasma and summarizes the atomic concentration of different species present on the mirror surfaces after exposure, measured with *in situ* XPS. The fitting procedure for XPS peaks was described before. A direct correlation between the magnetron powers and chemical composition does not exist. The sputtering rate of the magnetrons was highly dependent on the intrinsic impedance, which changes during exposure. This is due the thinning of the magnetron target as well as changes in its chemical composition. Therefore, the atomic concentration of the mirror surface is the only valid criterion to decide whether a mirror was in erosion or deposition condition. Accordingly, for the exposures including CH_4, one can conclude that Mo#1 and Rh #1 were in net deposition conditions, whereas Mo#2, Mo#3, Mo#4, Rh#2 and Rh#3 were in erosion conditions. However, even in erosion conditions the surface contained some impurity material. The Rh mirrors did not oxidize or carbidize during exposure, whereas Mo always appeared in carbidized form. Though carbides can be efficiently sputtered [204], this might still turn out to be a drawback of Mo coatings, since the actual mirror material is being sputtered. A possible carbidization will not be homogeneous over the surface due to difference of local plasma parameters near the mirror surface. Cleaning of such an inhomogeneous surface may lead to a roughened surface, which would change the reflectivity of the Mo mirrors. On the other hand, the current choice of the divertor material might not include carbon [200]. In this case, the carbidization associated with Mo would no longer be a concern.

Mirrors Mo#5, Rh#4 and Rh#5 were exposed to a plasma containing W and Al. The W

and Al deposits on the mirror surfaces appeared as oxides due to the residual species in the chamber. The electropositive Al adatoms reacted with electronegative oxygen faster than they coalesce with each other, resulting in completely oxidized deposits. Since Be and Al form similar kinds of oxides due to their very similar electropositivity, one can also expect Be to appear as oxides [205, 206]. However, the particle flux will be higher in ITER and therefore it can be expected that larger structures and porous films will form. Even in this case, an oxidized Be deposit was reported [207]. It is important to mention here that some FM candidates were recently tested in JET, where similar results regarding the surface composition were obtained [208]: (i) Carbidization was observed on Mo mirrors. (ii) Be was deposited as oxides. FMs in ITER which will be subject to deposition have to be cleaned either by plasma sputtering or laser ablation techniques. Plasma cleaning of oxides would require tricks such as applying an oscillating bias on the mirror in order to overcome charging effects and damages [209].

Figure 6.2 presents examples of the changes in the surface morphology of the mirrors due to exposure. Prior to exposure (Figure 6.2(a)), the mirror surfaces consisted of dense columnar grains, whereas a structureless amorphous morphology was apparent after exposure (Figure 6.2(b-d)). This amorphous material formed on the mirror surfaces was either hydrocarbons, carbidized metal or oxide deposits. Figure 6.3 shows how the surface topography of Mo mirrors in net deposition conditions look like. Figure 6.3(a) is Mo#1 with a W-C deposit and Figure 6.3(b) is Mo#5 with an Al_2O_3-W deposit. In addition, another deposit was also prepared by adding 46% argon into deuterium in order to see if crystallite deposits can be obtained with the increased deposition rate. Figure 6.3(c) shows the topography image of this sample, where the deposit is in the form of very porous Al-Al_2O_3-W crystallites. The roughness is too high in this case, dropping the specular reflectivity almost to zero. Experiments regarding the reflectivity degradation and recovery/cleaning of the mirrors deposited with such kind of structures are investigated in a different study (Master thesis of Lucas Moser at the University of Basel [210]).

The reflectance of mirrors during a plasma exposure or during storage in high vacuum may be quite different from their reflectivity after these mirrors have been stored in air. Figure 6.4(a) and (b) show an example of an *in situ* reflectance measurement performed during exposure in at Facility-I. Figure 6.4(d) is the comparison between the reflectivity of the last time slice relative to the first time slice (Ř) of Figure 6.4(a) and the ratio of specular reflectivity measured before and after experiments (Figure 6.4(c)). As can be seen, the two measurements did not produce the same result. Table 6.3 summarizes the *in situ* and *ex situ* results obtained from the data similar to that of Figure 6.4 for wavelengths of 450, 575 and 700 nm.

It can be seen in Table 6.3 that the mirrors in net deposition conditions were subject to a high loss of reflectivity. This degradation of the reflectivity was larger for *in situ* measurements, probably due to the degradation of the transparency of the viewports of the light beam. Moreover, reflectivity is an angle dependent quantity and coatings might actually result in more severe degradation for higher angles. For Mo mirrors in erosion conditions, the change in reflectivity was lower and comparable to the changes of the mirrors exposed to pure deuterium plasma (Chapter 3). This suggests that in erosion conditions, deuterium implantation has a stronger effect on the reflectivity than other impurities. For mirrors Mo#3 and Mo#5, the *in situ* measurements revealed a sudden increase in reflectivity when the plasma was started, which results in over 100% relative reflectivity in Table 6.3. Coatings have higher surface energy than polished surfaces, which may result in thicker oxide layers formed during storage in ambient conditions. The sudden increase of reflectivity is attributed to rapid removal of this native oxide
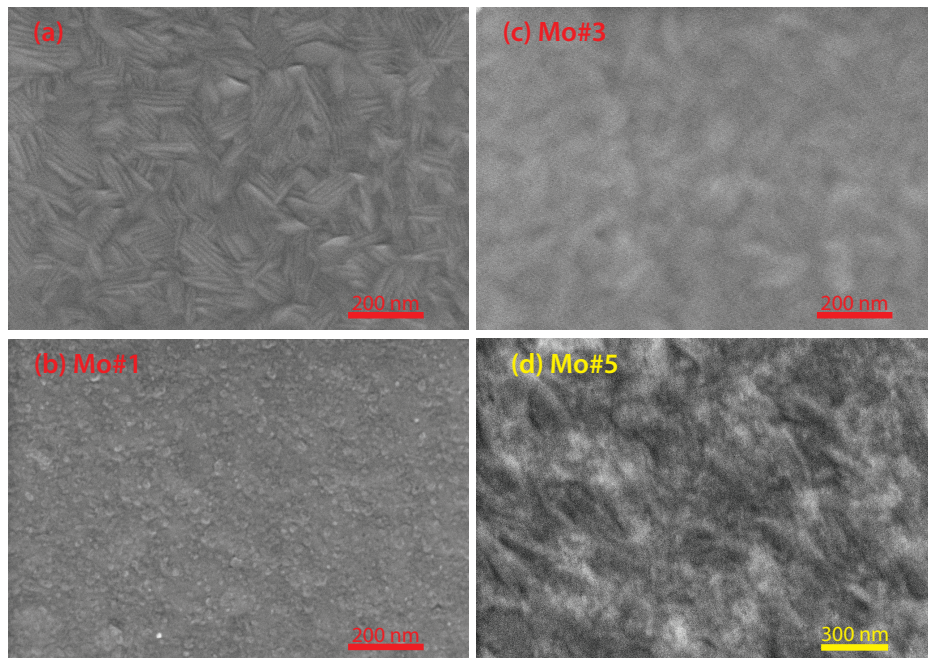
Figure 6.2: Typical surface morphology of a Mo mirror prepared by magnetron sputtering (a) and after exposure to ITER-like mixed environment (b-d). (b), (c) and (d) are Mo samples #1, #3 and #5 respectively. In (a), the surface consists of spikes as a result of dense columnar growth. In (b), (c) and (d) the surfaces are rather structureless suggesting an amorphous deposit growth. In (d), the lighter contrast corresponds to AlO_x.
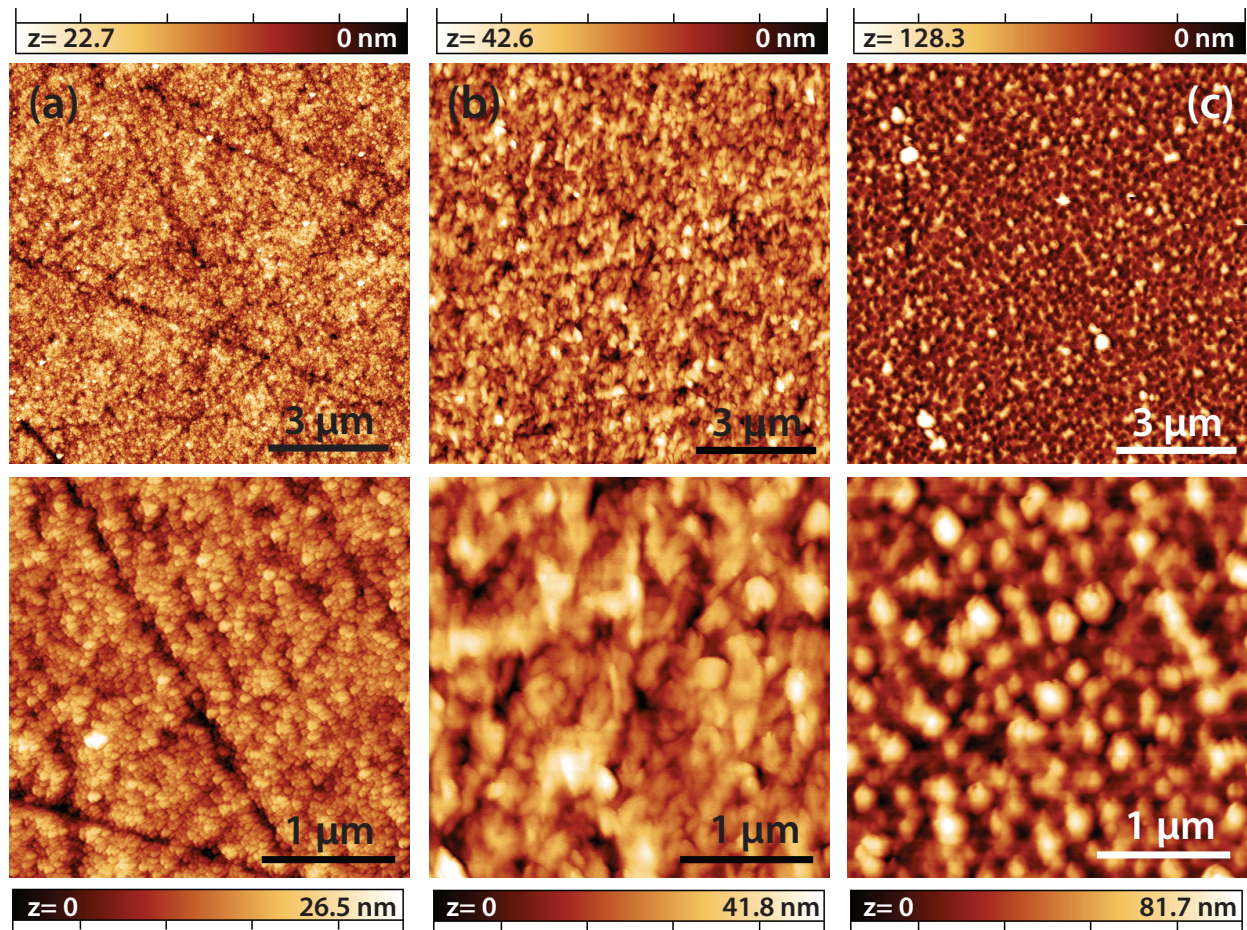
Figure 6.3: AFM topography images (upper panel: 10×10 m^2, lower panel: 3×3 m^2) of Mo mirrors tested with different impurity conditions: (a) Amorphous W-C deposits, (b) amorphous Al$_2$O$_3$-W deposits (c) crystalline Al-Al$_2$O$_3$-W deposits. All deposits contain unknown amount of deuterium. Lower panel is the magnified images of the upper panel with the following r$_{rms}$ values estimated: 3.6 nm for (a), 6.8 nm for (b) and 17.4 nm for (c). The first two values are comparable to those of bare coatings, but the roughness of crystalline deposits is to high, increasing the diffuse reflectivity to total reflectivity at lower wavelengths (Eq. 1.5).
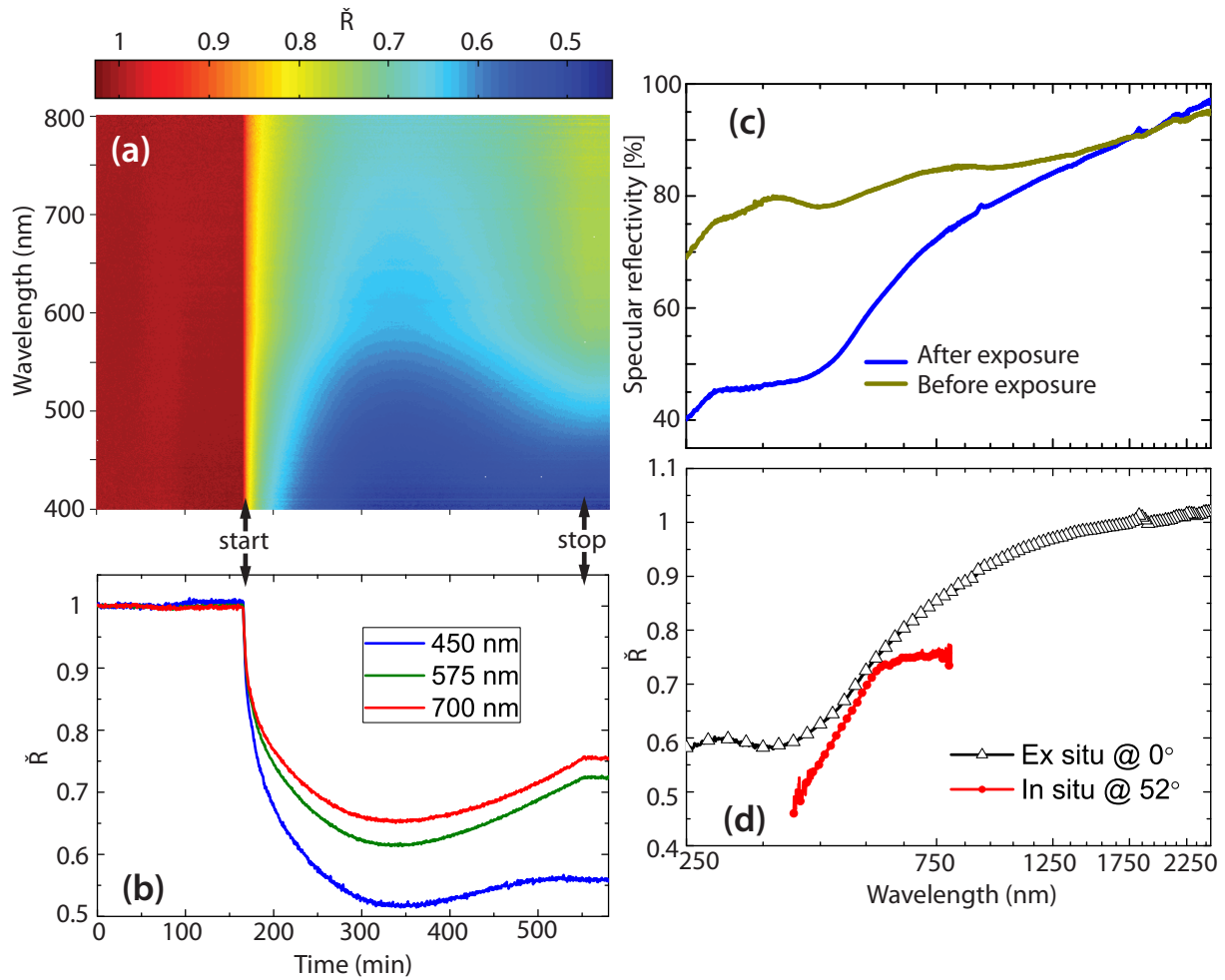
Figure 6.4: Example (Rh#1) of an *in situ* relative reflectivity (Ř) measurement (a, b), initial and final *ex situ* specular reflectivity of the mirror for a wavelength range between 250 to 2500 nm, and the comparison between these two measurements (d). The black curve in (d) is simply calculated as the ratio of the two curves in (c). @ 0° and @ 52° refer to the angle between the incident light beam and normal of the surface plane.

Table 6.3: Summary of the reflectivity change of the mirrors relative to their initial reflectivity. Values are presented as percentages. *In situ* measurements of Mo#3 and Mo#5 samples had a sudden increase in the reflectivity of $\sim 3\%$ and 5%, respectively. n/a refers to measurements where data acquisition was not applicable due to system instabilities.

	in situ refl. @ 52 °			spectrophotometer @ 0 °		
	450nm	575nm	700nm	450nm	575nm	700nm
Mo#1	56	75	95	79	88	93
Mo#2	91	96	98	95	96	98
Mo#3	n/a	103	102	99	99	99
Mo#4	n/a	80	83	96	98	98
Mo#5	100	99	98	94	96	97
Rh#1	56	72	75	63	75	83
Rh#2	n/a	88	92	97	98	98
Rh#3	75	82	85	76	84	89
Rh#4	97	96	96	97	98	98
Rh#5	99	98	97	98	99	99

layer on the Mo surface after deuterium plasma was started.

In Chapter 5, it is shown that a deuteride film grows on the surface during pure deuterium plasma exposure, which decreases its *in situ* reflectivity. The reflectivity degradation observed in any of the Rh samples in this chapter may have some contribution from a possible deuteride formation. However, due to the complexity of the gas mixture of the plasma in current exposures, it is not possible to determine this effect.

Mirrors Mo#5, Rh#4 and Rh#5 retained their initial reflectivity after exposure. This is probably due to the very low optical thickness of the oxides formed on their surface, together with the fact that the surface remained rather smooth ($r_{rms} = 5.5$ nm). In [210], thicker nanocrystalline coatings are shown to decrease the specular reflectivity due to an increase of the diffuse reflectivity as a result of rough ($r_{rms} = 17.4$ nm) deposits grown on the surface. In terms of the optical constants of the deposits, further investigation is still necessary to determine the critical thickness of such deposits at which the reflectivity starts to degrade.

None of the mirrors presented in this chapter had a significant increase in the diffuse reflectivity after exposure, suggesting a negligible change in the surface roughness of the samples.

6.4 Outcomes

Except the mirrors in net deposition conditions including carbon, the tested mirrors did not experience a severe change in their reflectivity. In carbon free plasma, Al and W impurities were deposited as oxides with very low optical thicknesses. Therefore, current experiments are not conclusive about reflectivity degradation concerning thicker coatings. Cleaning techniques have to be developed for all mirrors in deposition conditions, keeping in mind that amorphous oxides and carbides are more likely to grow on the metal surface than metallic W or Al. Depending on to the current choice of divertor material [200], ITER plasma might be carbon free. In this case, the drawback of Mo mirrors in terms of carbidization is no longer a concern.

The results presented in this chapter are the first results obtained in Facility-I that involves ITER-relevant plasma mixture. This first step had already paved the way for further work which includes measurements of the *in situ* reflectivity changes during the laser and/or plasma

cleaning of mirrors, on which impurity deposits will be grown in Facility-I or in outside facilities (e.g. tokamaks). The big picture is to experimentally simulate impurity deposition and cleaning cycles of FMs, which will be a part of the routine ITER operation. The first results with laser [211] and plasma cleaning [210] techniques are obtained during the course of this thesis using the impurity deposition parameters provided in this chapter.

Chapter 7

Properties of protium plasma treated gold films

In this chapter, buckling of the 100 nm thick gold films after a protium plasma treatment with low ion impact energies ($\approx$30 eV) is reported. Films grown by the Volmer-Weber mechanism have vast number of defect sites in the film and at the coating interface. The compressive stress causing the buckling is associated with protium trapping and accumulation inside these sites, ultimately leading to delamination from the substrate. The delaminated parts appear as circular blisters on the surface.

7.1 Literature Review

Depending on the growth stage of the nanocrystalline metallic films which nucleate and grow by the Volmer-Weber mechanism, different stress regimes exist [212, 213]. The films initially experience a tensile stress which is associated with the grain boundary formation during island coalescence [214–217]. Gold atoms have high mobility even at RT. For such high atomic mobility, the tensile stress drops and often becomes compressive until it reaches saturation. However, upon interruption of the coating process, the compressive stress state changes reversibly in the tensile direction [218–223]. Moreover, the dynamics of the coating process in magnetron sputtering are highly dependent on the coating parameters such as coating speed, process gas pressure, etc. [114, 115, 224]. Depending on these parameters, the residual stress in a film after sufficient time of relaxation may be tensile or compressive.

A typical fingerprint of compressive stress is buckling of the films [225–227], occurring as a result of stress relaxation [228–230]. Recently, buckling of 630 nm gold films during preparation by physical vapor deposition on Si(100) substrates which arose as a result of the relief of this compressive stress was reported [227]. This buckling of the films was localized within the boundary of delamination and the buckled structures were classified as well-defined circular blisters [227]. More recently, super-imposed blisters (blisters on top of other blisters) of gold films were also reported [231].

Another mechanism which can result in blistering and partial delamination of the films is implantation of highly energetic (in the range of keV) ions [232–234]. Here, the blister formation is localized in a region around the mean penetration depth of the implanted ions. Another pathway for obtaining a comparable effect is via introducing a buried, hydrogenating, compressive layer

acting as defect/trap layer for protium atoms [47–49]. Similar to buckling during the coating process, the protium induced film buckling is also associated with the relief of the compressive stress.

In this chapter, buckling of 100 nm thick gold films are reported after being exposed to protium plasma with low ion impact energies ($\approx$30 eV). A buried, hydrogenating (or hydride forming), compressive layer is not present in the current case. Films grown by the Volmer-Weber mechanism have a vast number of defect sites in the film and at the coating interface. The compressive stress causing the buckling is associated with protium trapping and accumulation inside these sites, ultimately leading to delamination from the substrate.

7.2   Experimental preparations

Both the coating and the plasma exposure processes were performed in the preparation chamber of Facility-II when the background pressure was better than 1×10^{-5} Pa. For the coating process, a round gold target (99.9% purity, 2 cm in diameter) was positioned at a distance of ~10 cm from the substrate. ~100 nm nanocrystalline gold films were prepared by water cooled magnetron sputtering on Si(100) substrates at RT. Argon was used as the process gas with a fixed pressure of 1 Pa. The magnetron was operated with a pulsed-DC power of 40 W for a duration of 5 minutes. 0.34 nm/s nominal coating rate was measured with a quartz crystal microbalance with these parameters. *In situ* XPS and UPS measurements of the coatings revealed pure gold and typical electronic characteristics of nanocrystalline gold [193], respectively.

The protium plasma treatment was performed at Facility-II, with the plasma having a potential of $\approx$30 V with respect to ground (other parameters described in Chapter 2). The plasma particles consist of neutral species (H_3, H_2 and H), electrons, photons, metastable negative ions, molecular (H_3^+ and H_2^+) and atomic (H^+) positive ions. Among these, the positive ions play the most crucial role. The samples were kept electrically grounded, which results in an acceleration potential of 30 V, hence an ion impact energy of 30 eV. The molecular ions (H_3^+ and H_2^+) dissociate during the impact and deposit energies of 10 and 15 eV/H on the surface, while the atomic protium ions (protons) deposit an energy of 30 eV/H [43]. The exact concentration of the plasma ions is not known. All samples were treated for 60 minutes unless stated otherwise.

The films were characterized with SEM and XRD before and after protium plasma treatment. For the determination of the size of the blisters, an intermittent contact mode AFM experiment was performed using a Nanosurf Mobile S operated in ambient conditions. A separate 1 μm film was coated on a Si(100) substrate for nanoindentation measurements performed with a Hysitron device operated with a Berkovich tip geometry. The indentation depth was not more than $1/10^{th}$ of the total thickness of the film. The hardness and the reduced Young's modulus (E_r) were calculated as 1.86 $\pm$ 0.1 GPa and 137 $\pm$ 3 GPa from the contact stiffness, respectively, using the Oliver and Pharr method [235] after tests on 25 different points with a load of 1 mN. As the gold films possess a strong (111) fiber texture (shown later), they are transversely elastically isotropic. Hence, the indentation modulus may be written as:

$$E_r = \frac{E_\perp}{1 - \nu_{13}^2} \tag{7.1}$$

where $E_\perp$=125 GPa is the orientation dependent modulus along the loading axis in the indenter and ν_{13}=0.3 is the in plane Poisson's ratio. In Eq. 7.1, the indenter component is ignored because of the very low compliance of the diamond indenter.

Texture characterizations and residual stress analyses were carried out using a four-circle diffractometer (Seifert XRD 3003) operating at 40 kV and 30 mA, with a Cu x-ray tube ($\lambda =$ 0.15418 nm) equipped with a 1×1 mm^2 point focus and a Ni filter on the direct beam path to absorb the Cu Kβ radiation. The incident beam was collimated using a collimator 1 mm in diameter and targeted on the samples mounted on an Eulerian cradle for Ψ tilting. Since the gold films are textured (shown later), the x-ray measurements have been performed in the pole direction corresponding to two independent plane families, namely {331} and {420} [236]. The residual stress state was calculated from the lattice strains assuming a planar equi-biaxial stress state [236] and using the x-ray elastic constants of {111} fiber textured gold films [237].

7.3 Results and discussion

7.3.1 Properties of the gold films

Figures 7.1(a) and (b) show the 1×1 μm^2 AFM topography images of the 100 nm gold films prepared on Si(100) before and after protium plasma treatment, respectively. No significant change in the surface morphology of the films can be identified after the plasma exposure. SEM image of a gold film is presented in Figure 7.1(c), which shows similar features to the AFM images. Figure 7.1(d) presents the x-ray diffraction pattern of the films measured with a θ-2θ configuration. It can be deduced from these spectra that the films had a (111) texture and consisted of nanocrystals with a diameter around 32 nm calculated from the Scherrer's formula. The same measurement with a glancing incidence of $1°$ (Figure 7.1(e)) resulted in a polycrystalline distribution. Treatment of the films with protium plasma did not result in any significant changes in the crystal orientation of the films. The inset in Figure 7.1(d) is the χ-scan over the (111) peak, also revealing a texture in the film both before and after the plasma treatment. The residual stress analyses carried out before and after the protium plasma treatment both resulted in a compressive stress of -30 $\pm$ 6 MPa. As will be presented later, the density of the locally plastically deformed areas was not more than 5% of the entire surface; thus the residual stress measurements after the plasma treatment are assumed to reveal the stress in the zones without any deformation. It can be concluded accordingly that the protium plasma treatment did not change the stress state of the undeformed zones.

7.3.2 Blister formation

No buckling or any other kind of plastic deformation was observed in the prepared gold films (even for 1 μm thick coatings) prior to plasma treatment. The gold films were stored for a sufficient time (more than an hour) in high vacuum for stress relaxation before plasma treatment. After exposure of the gold films to protium plasma for 1 hour (total ion fluence of around 5.4 $\times$ 10^{18} cm^{-2}), a blurring of the yellow color of the gold due to the diffuse reflectivity associated with surface roughening was visible to the naked eye. Plasma treated gold films were further investigated under a light microscope (Figures 7.2(a) and (b)). It can be seen that the surface contains circular blisters as a result of buckling of the gold film under compression. Figures 7.2(c), (d) and (e) are the SEM images of the blisters, and reveal two types of them: One being smaller sized single blisters and the other one being larger sized super-imposed blisters similar to the suggestions in Ref. [227] and [231], respectively. It can be seen from the cross section view of a small sized blister in Figure 7.2(f) that the delamination is occurring at the interface between
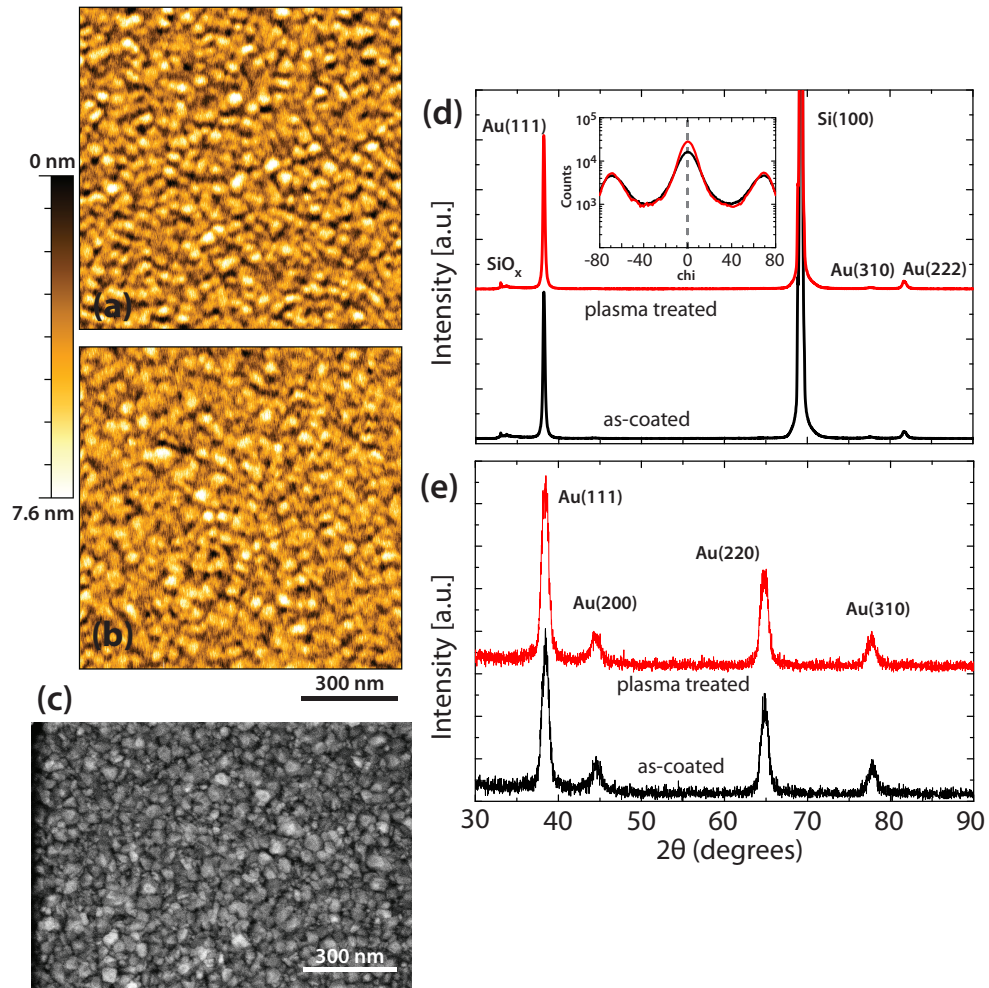
Figure 7.1: 1×1 μm^2 AFM topography images of the gold films (a) before and (b) after exposure to protium plasma. (c) SEM image of a gold film. X-ray diffraction patterns of the gold films (d) with the θ-2θ configuration and (e) with a glancing incidence of $1°$. Black lines of (d) and (e) are the XRD spectra of the gold films prior to plasma treatment, whereas the red lines are after plasma treatment. The inset in (d) is the chi scan over the (111) peak.

Figure 7.2: (a) and (b) are the optical microscopy images of the protium induced blisters of gold films prepared on a Si(100) substrate. The superimposed blisters, such as the one presented in (e), appear larger than the single blisters and are asymmetric. (c), (d) and (e) are the SEM images of such blisters. (f) is a SEM cross-section view image of a blister, revealing that delamination is taking place in the interface between the film and the substrate. (g) and (h) are the 90.4 × 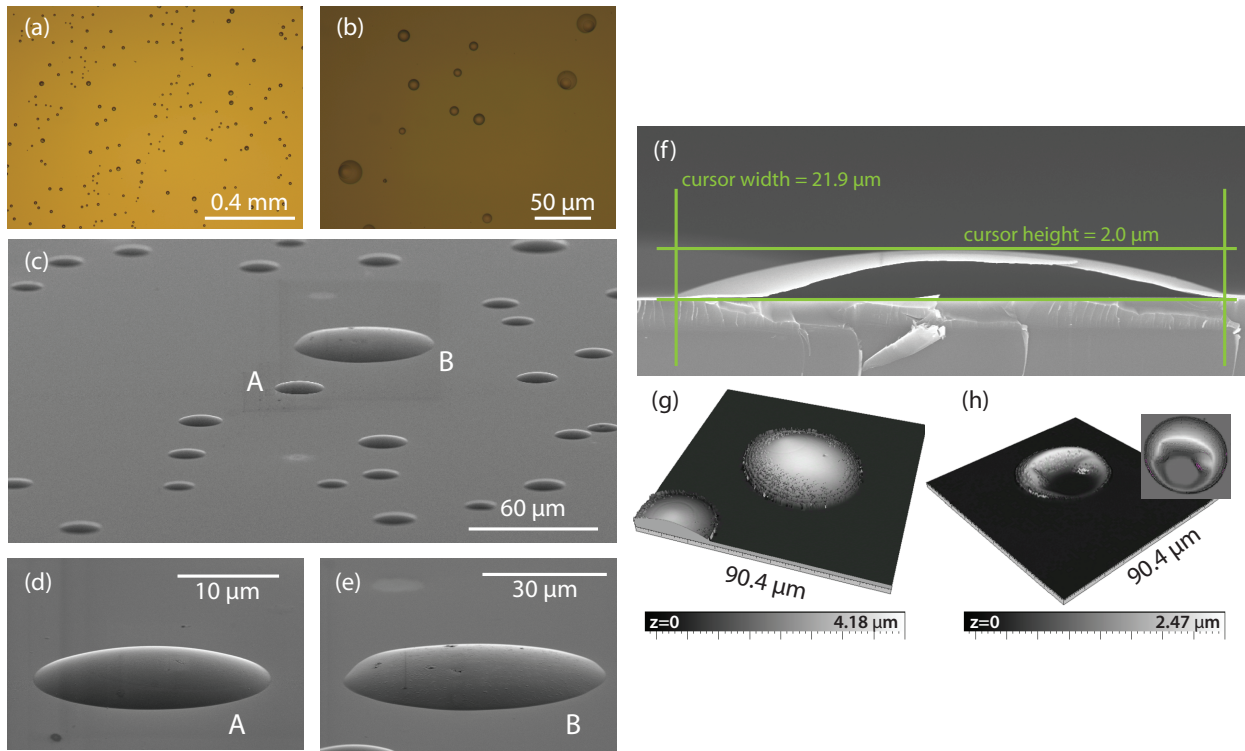90.4 μm^2 confocal images of a stepped blister and a smashed blister, respectively, which both are not the commonly observed cases.

the substrate and the coating. Figure 7.2(g) is a confocal image of a blister where the sidewalls have a stepped structure. It should be noted that this is not the general case, but nevertheless suggests that delamination can also occur stepwise. Figure 7.2(h) is another confocal image of another uncommon observation, where a certain part of the circular blister appeared collapsed on the substrate. A crack formation was not observed in any of the blisters. The blisters are stress relaxation zones occurring when the compressive stress in the film exceeds the critical stress during protium plasma treatment [225, 227].

It has been previously argued that there are two kinds of mechanisms that can lead to protium induced blistering [49]. The first case requires the presence of energetic ions, which have the potential to introduce new blister initiation sites. The second pathway to blister formation is the hydrogenation process which does not require energetic ions but availability of existing initiation sites. Previous works involving compressively stressed buried layers [47,48] and multilayer stacks [49] have shown blister formation due to this hydrogenation. In these cases, the layers under compression had vacancy accumulations where protium atoms have hydrogenated the dangling bonds of Si, which subsequently lead to the formation of H platelets and ultimately
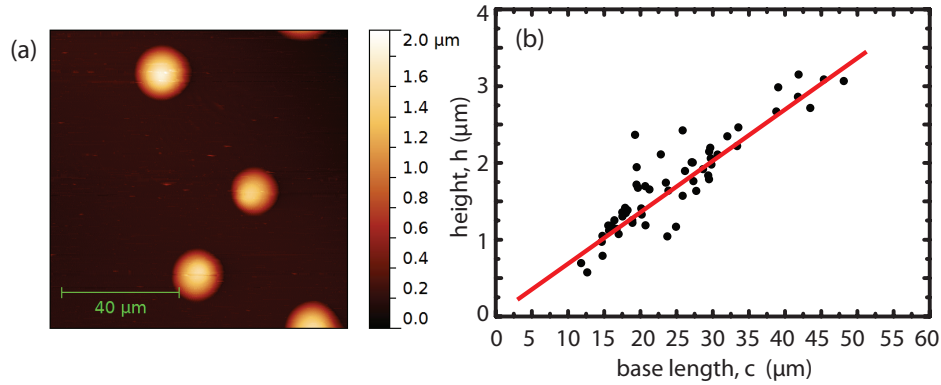
Figure 7.3: (a) AFM topography image of a blistered surface. (b) Statistics of the dimensions of the blisters obtained from a set of images similar to the one shown in (a). $\Theta = 2 \cdot \tan^{-1}(2h/c)$. The size parameters of the blisters are in the Euler column buckling regime.

to the formation of H_2 gas bubbles.

   Both of these mechanisms are not available in the current case. The damage introduced by the plasma ions can be neglected since the sputtering threshold of protium on gold is over 100 eV [6]. TRIM simulations suggest the maximum ion implantation depth as ∼4 nm for the 30 eV/H ions [126], leaving only bulk diffusion of atomic protium as the effective transport phenomenon leading to protium loading of the entire film. The implanted ions can overcome the diffusion activation energy and diffuse to the grain boundaries, through which they can further diffuse inside the bulk. Since further diffusion to the substrate material is limited, the gold films are loaded with atomic protium during the plasma treatment. If the dynamic protium inventory in the film exceeds the solubility of protium in gold, excess protium will nucleate and accumulate at the defect sites such as voids and lattice distortions. As a result, compressive stress will build up due to over-pressurized protium gas trapped at these sites. In this scenario, there is no need for hydrogenation as opposed to previous works [47–49]. In fact, gold does not form any binary compound with protium [238]. In the current case, the gold films were grown by the Volmer-Weber mechanics and, therefore, have a vast number of defect sites at the coating interface and inside the film which facilitate protium seeding without requiring hydrogenation.

   The blisters are stress relaxation zones spontaneously occurring when the compressive stress in the film reaches the critical stress during protium plasma treatment [225, 227]. In order to address the stress during the plasma treatment which results in blistering, the geometrical parameters of the blisters have to be determined. The most critical geometrical parameter is the ratio between the height (h, interface separation at the center point of deflection) and the base length (c) of the blisters. Since the sidewalls of all the blisters on the Si(100) substrate are oriented with an angle (Θ) greater than $\sqrt{4.88 \times 6 \frac{t}{c}}$, the non-linear Föppl von Kármán's theory derived in [225] from the elastic Euler column equations are valid for all of the blisters observed [227]. AFM technique is used to determine the size of the blisters (a sample image is presented in figure 7.3(a)). Figure 7.3(b) shows the size statistics of randomly chosen protium induced blisters formed on the gold films prepared on the Si(100) substrate. Using this collection of the AFM images, a linear relation between between h and c can be obtained. Finally, the intrinsic stress can be calculated from the post-buckling reponse as:

$$|\sigma| = |\sigma_c| + 4.88kE_r \left(\frac{h}{c}\right)^2 \tag{7.2a}$$

$$\sigma_c = -4.88E_r \left(\frac{t}{c}\right)^2 \tag{7.2b}$$

$$k = 0.2473[(1 + \nu_{13}) + 0.2331(1 - \nu_{13}^2)] \tag{7.2c}$$

where $-\sigma = \sigma_{rr} = \sigma_{\theta\theta}$ is the uniform biaxial compressive stress in the initially flat thin film and, σ_c is the classical critical stress for buckling, above which the Euler column ($\Theta = 0°$) appears. Again, assuming transverse anistoropy and using in-plane Poisson's ratio (ν_{13}=0.3), the second term in Eq. 7.2a can be calculated as -1.2 ± 0.3 GPa for the blisters. The first term is different for all of the blisters, but it is two orders of magnitude smaller than the second term and can be ignored.

An alternative thin film deformation mechanism which manifests itself similar to buckling is bulging, i.e. deflection of the film away from its substrate over a region which is not attached by applying a pressure p to the coating interface. This pathway would, of course, require partially debonded zones as well as weak adhesion between the film and the substrate for an effective diffusion of protium along the coating interface to these debonded zones. The equation governing bulging for a membrane-like response is: [239, 240]

$$p = \frac{16\sigma th}{c^2} + \frac{128Et}{3c^4(1 - \nu)}h^3 \tag{7.3}$$

The role of the residual stress in Eq. 7.3 would be to soften or stiffen the response of the bulging film to applied pressure. The equation becomes irrational for films under high compression, because virtually all films under compression should buckle, thus negative local gas pressures are sufficient. Of course, a combined effect of bulging and buckling can be considered: Bulging for films in compression results in wrinkling of the blisters because the compressive stress around the edge of the blisters cannot be relieved while the center of the blister is under tension [239, 240]. The only assymety observed in the current case is superimposed blisters, which is typically observed for buckled films [226]. Moreover to this point, if bulging is considered as the primary mechanism of deformation, the linear scaling law observed in Figure 7.3(b) would have been sheer luck. At this point, we also would like to recall that it is widely accepted that nanocrystalline coatings should not be subject to bulging-induced blistering during protium loading, since protium which should have been stuck at the interface can indeed diffuse through the grain boundaries to external surfaces [143, 144]. Moreover, no blistering was observed in the previous chapters when rhodium, molybdenum or tungsten films on Si(100) or steel substrates with thicknesses ranging between 10 to 100 nm were treated for hours with protium or deuterium plasma. Same tests performed on molybdenum and tungsten foils resulted in blistering due to the well-known fact of protium accumulation between macroscopic grains. Given all these facts, the author concludse that bulging does not play a major role in the current case.

7.3.3 How to avoid blistering?

Protium induced buckling can result in a catastrophic failure for some technological applications involving protium plasma treatment of gold coatings. For instance, Figure 7.4(a) shows the

optical microscopy image when the sample was exposed for 8 hours to protium plasma, where the blisters have already started to get linked to each other. Therefore, four possible ways were investigated in order to suppress blistering:

1- Decreasing the ion impact energy: The plasma used in these experiments has an electron temperature of 3.5 eV. If the sample is kept electrically floating instead of grounded, the ion impact energy will decrease. In the floating sample case, as explained in Chapter 2, the ion impact energy is 12.6 ± 1.8 eV. This will result in proton deposition energies of 4.2, 6.3 and 12.6 eV/H. Only a few blisters (one or two per cm^2) were observed under this condition.

In low temperature protium plasma, atomic protium is much more abundant than the ions, which can be claimed to diffuse through the columnar grain boundaries (typical of Volmer-Weber films) all the way down to the coating interface. Previous results showed that atomic protium is not responsible for the excess loading of the thin films with protium, which ultimately leads to failure [49]. Current results extend this, and suggest that a certain energy threshold has to be overcome to cause buckling of the films. This may be related to the mean implantation depth of the impinging ions, which is ≈ 6 Å for 13 eV/H energy, whereas ≈ 9 Å for 30 eV/H energy. In the lower energy case, the implanted ions can diffuse out from the surface more efficiently. Here, the low coordination number of the surface atoms (i.e. cycloid-shaped surfaces of the grains (Figure 2.12(a))) may also play a role. The percentage of backscattering is $\approx 31.5\%$ in both cases.

2- Increasing the protium solubility of gold by increasing the temperature: This was tested by increasing the temperature of the sample to 150 °C via resistive heating. It was not possible to suppress blistering, and an optical microscope image similar to Figure 7.2(a) was obtained.

3- Performing plasma exposure in cycles to release protium: During this test, plasma exposure was performed in cycles consisting of 1 minute of plasma treatment followed by 5 minutes of storage in high vacuum to let protium diffuse out from the film. After $\sim$15 cycles, one could start to see blister formation with the naked eye from the viewports of the vacuum vessel. After $\sim$25 cycles, the surface was already blurred; thus further exposure deemed unnecessary. Here, a drawback has to be pointed out: Gold has a higher linear expansion coefficient than that of silicon, which results in compressive thermal stress during the thermal treatment.

4- Changing the substrate: Protium trapping in the film should be dependent on the further diffusion of atomic protium into the substrate material. In order to address this, protium plasma treatment with the same parameters and exposure time was also performed on 100 nm gold films which were prepared on mechanically polished SS316L and polycrystalline tungsten substrates. No blistering was observed when the plasma was applied to a gold coating on an SS316L substrate. The substrate acts as a sink, where the excess protium in the gold film can diffuse into. The diffusion coefficient of protium in SS316L at RT is in the 10^{-10} cm^2s^{-1} range for SS316L [241], and thus an order of magnitude higher than that for protium in silicon [242]. Therefore, the effective number of protium trapped at the interface or in the gold film is lower when it is prepared on SS316L in comparison to silicon. Of course, changing the substrate can only be a solution for mild plasma conditions. For instance, when the plasma was ignited with 90 W instead of 49 W (ion flux estimated as $2.8 \pm 0.5 \times 10^{15}$ $cm^{-2}s^{-1}$, approximately 2 times higher), large and homogenously distributed blisters appeared on the gold film prepared on the SS316L substrate (Figure 7.4(b)).

However, this simple diffusion model is not quite realistic, since the coating interface consists of native oxides with different diffusion coefficients and hydrocarbon contamination from air.
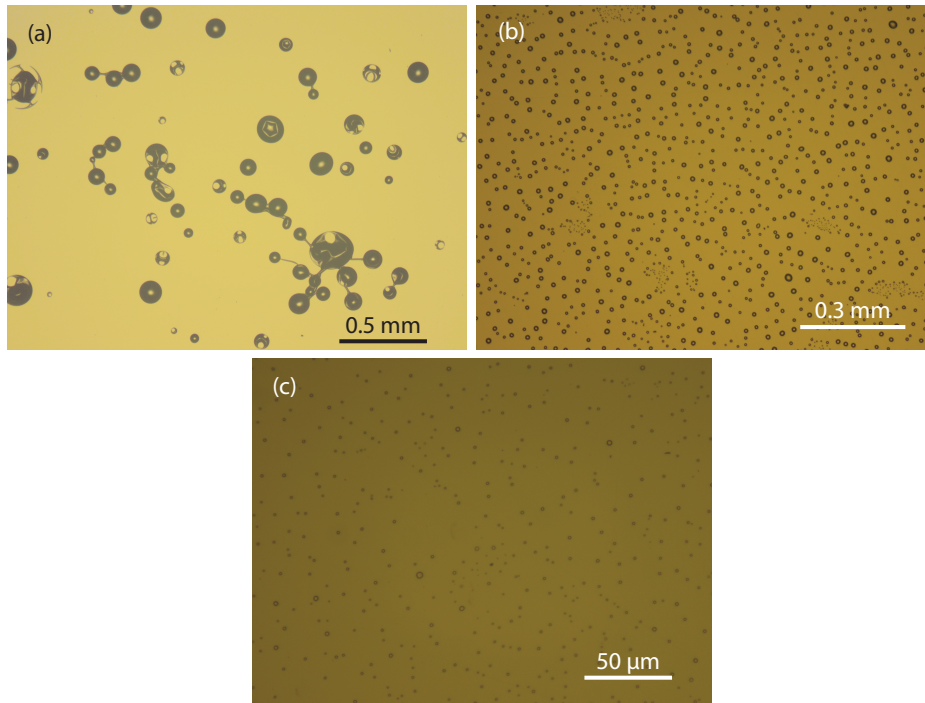
Figure 7.4: Optical microscopy images of the blister formation after protium plasma treatment of 100 nm thick gold films prepared on (a) silicon after 8 hours of exposure at 49 W, (b) mechanically polished SS316L after 1 hour of exposure at 90 W and (c) polycrystalline tungsten after 1 hour of exposure at 49 W.

For instance, the diffusion coefficient of protium in tungsten at RT is in the range of 10^{-9} cm^2s^{-1} [243], an order of magnitude higher than that of SS316L. In contradiction with the above discussion, very small-sized blisters occurred during the plasma treatment of gold films prepared on the polycrystalline tungsten substrates (Figure 7.4(c)). Moreover, polished tungsten surface typically has a higher roughness than polished SS316L and, therefore, initially has more defect sites at the coating interface. The actual sample temperature is also slightly higher than RT during the plasma treatment due to the ion impact, which changes the diffusion coefficients; adding more uncertainty to the actual effect of the substrate choice. It is noteworthy to mention that due to mechanical polishing, tungsten and SS316L surfaces initially have large defect sites interface, where protium gas can accumulate and cause local bulging of the gold film. In fact, no superimposed blisters (signature of post-buckling response) were observed on these samples. It is indeed, not possible to neglegt bulging when such rough substrate surfaces are used.

As a result, it can be concluded that no method can fully suppress blister formation. The most efficient method among the ones presented would be letting the sample electrically float in order to reduce the impact energy of the ions.

7.4   Outcomes

The compressive stress causing the buckling is associated with over-pressurized protium trapped in the film and at the coating interface. The plasma is the protium source, the gold film is the reservoir and the substrate material acts as the sink. Dynamic protium inventory in the film gradually builds up a compressive stress in the film until this stress reaches the buckling threshold. This leads to buckling delamination of the film from the substrate, which releases the protium induced stress.

The blistering intensity is also found to be related to the impact energy of the ions. Higher energy ions (30 eV) result in heavy blistering of the surface, whereas lower energy ions (12.6 eV) result only in a few blisters.

The vast majority of the films used in technological applications are grown by the Volmer-Weber growth mechanism. The buckling of such films during protium plasma treatment is an undesired situation, limiting plasma processing of samples containing parts coated with gold. In a more positive perspective, this situation can be exploited in a similar manner to the commercial ion-cut technologies [244]; thus the gold films can be cleaved off from their substrates to be transferred onto somewhere else.

Chapter 8

Properties of protium plasma treated HOPG

This chapter explains the characterization of hydrogenated highly ordered pyrolytic graphite (HOPG) and graphene with various experimental techniques such as photoelectron spectroscopy, Raman spectroscopy, atomic force microscopy, scanning tunneling microscopy and spectroscopy. Hydrogenation was achieved by exposure of single and multilayer graphene and HOPG to pure protium LTP at Facility-II. The aim of this chapter is to show the efficiency of the hydrogenation and recovery processes using pure protium plasma treatment and thermal annealing. This is done by presenting the electronic, phononic and topographical differences between the pristine and plasma treated HOPG surfaces.

8.1 Motivation

Being an sp^2-hybridized single layer of carbon atoms arranged in a densely packed honeycomb lattice with a true atomic thickness (Figure 8.1(a)), graphene possesses unusual electronic and mechanical properties [20, 21]. A new perspective is the chemical modification of graphene, especially the incisive idea of attaching atomic hydrogen to both sides of the graphene lattice to produce graphane (Figure 8.1(b)); an sp^3-hybridized insulating derivative of graphene [22–25]. Graphane offers a brand new playground for physicists and engineers, particularly as a prospect for two dimensional electronic applications. Nanowire [245] or transistor concepts consisting of only graphene and graphane could be realized. Another possible application is its characteristic for hydrogen storage. It has a volumetric capacity of 0.12 kg H_2/liter which is higher than the Unites States Department of Energy target of 0.081 kg H_2/liter for the year 2015 [22].

A prerequisite for graphane synthesis is the abundance of protons to react with unsaturated C-C bonds of graphene; subsequently leading to C-H bond formation on both sides of the graphene. The elegant yet simple solution to obtain such a chemisorption may be to use a pure protium LTP with a typical average electron temperature (T_e) of 2-5 eV, where the protium would be easily dissociated (required energy as T_e: 4.52 eV) and chemisorbed on the surface, and a small portion will be ionized (required energy as T_e: 13.6 eV). The atomic ion implantation might also hydrogenate the other side of the surface layer and even some other subsurface layers. The 3.5 eV plasma used in this work results in an ion impact energy of 12.6 eV on the sample surface (as explained in Chapter 2). With this technique, proton deposition energies can be

obtained which are high enough to overcome the energy barrier (3.7 eV) to penetrate the center of the hexagonal carbon [246], without physically sputtering (36 eV) the carbon atoms [6, 247]. Moreover protium ions can even be implanted deeper into the first 4-5 layers of HOPG, suggested by the SRIM simulations [126].

The question is: Will graphane form after the plasma exposure and if it does, is it possible to distinguish its existence from other possible surface rearrangements caused by the exposure? Before starting, it should be clearly stated that graphane is a reserved word for graphene which is fully hydrogenated from both sides. In reality, there will always be protium deficiencies and point defects and the obtained material would not be a perfect graphane. Therefore, hydrogenated graphene will be used for the rest of this thesis referring to a graphane-like structure.

The interaction of hydrogen with graphitic surfaces had been investigated various times in the last decades. The earlier research concentrated on the physisorption of hydrogen molecules on such surfaces [248–250]. This was followed by theoretical [251], and experimental works focusing on the chemisorption of atomic hydrogen [252–256]. A new research focus is the interactions of hydrogen containing plasmas with graphitic surfaces [24, 257]. Particularly the work of Elias *et al.* is interesting, in which graphane growth was claimed after exposure of free-standing graphene to a plasma containing 10% hydrogen [24]. In this chapter, single and multilayer graphene and HOPG were exposed to a pure protium LTP and various techniques such as photoelectron spectroscopy, Raman spectroscopy and scanning probe microscopy were employed for its characterization. However, due to the insufficient electrical conductance and high amount of hydrocarbon contamination from air, it was not possible to use photoelectron spectroscopy and scanning tunneling microscopy techniques for graphene on SiO_2.

On the contrary to plasma treatments in previous works [24, 257], mixing a second gas was avoided in this work. Introduction of a high-Z gas such as argon would have cooled down the plasma due to increasing number of recombinations, which would have hindered protium implantation. This might be the reason why graphane formation was claimed only for free-standing graphene by Elias *et al.* Also, low energy argon ions result in changes in the atomic structure of HOPG and, therefore, are not desired in this experiment [258].

8.2   Experimental preparations

Details of the plasma parameters have been given in Chapter 2. In summary, ion impact energy: 12.6 eV, ion flux: $1.5 \pm 0.5 \times 10^{15}$ cm^{-2}s^{-1}. The author thinks that double side hydrogenation might be achieved under these plasma conditions. It is also possible to achieve single surface hydrogenation, anisotropic chemical etching [259] or physical sputtering of HOPG by changing the plasma parameters or sample conditions.

Implantation is a homogeneous process taking place all over the HOPG subsurface layers. With a pessimistic approach, one can assume that only 10% of the impinging ions are atomic, where half of them get backscattered, physisorbed or chemisorbed on the surface, leaving only 7.5×10^{13} cm^{-2}s^{-1} of them getting implanted as protons. Also taking the H-H combinations in the HOPG into account, the necessary ion fluence to hydrogenate the subsurface layers of the HOPG (surface density is 3.8×10^{15} cm^{-2} and hydrogen uptake is 1:1 for graphane formation) would be several minutes.

During protium plasma exposure, the samples were electrically floating while they were being heated resistively. HOPG samples were cleaved in air before they were introduced to the UHV

environment. Temperature calibration was done in a separate exposure using a chromel/alumel thermocouple mounted on the sample as it was monitored with a pyrometer during actual exposures. Graphene flakes for Raman spectroscopy measurements were prepared by exfoliation of HOPG using a PDMS stamp and transferring them on SiO_2 [260]. The number of layers was determined from the 2D peak of the Raman spectra which was acquired prior to plasma treatment.

8.3 Results and discussion

8.3.1 Raman spectroscopy

Raman spectroscopy is a frequently used tool for the analysis of graphitic materials. The Raman spectrum of graphite consists of the D and G peaks, around 1350 cm^{-1} and 1585 cm^{-1} respectively, which arise from vibrations of sp^2-hybridized carbon atoms [261–264]. The D peak is caused by breathing-like modes corresponding to transverse optical phonons near the K point of the Brillouin zone. It is an intervalley double-resonance Raman process which is initiated only by a deviation from the defectless two dimensional character [261, 262, 264]. On account of this, both hydrogenation and any kind of disorder manifest itself as the rise of this peak and a distinction between these two phenomena is not possible. Its overtone, the 2D peak which appears around 2700 cm^{-1}, is a second order process involving two inelastic scatterings and it is always present. The shape of this 2D peak is defined by the number of graphene layers (i.e. two peaks at 2682 cm^{-1} and 2723 cm^{-1} for graphite whereas a single peak at 2671 cm^{-1} for single layer graphene) [263]. The G peak represents the optical E_{2g} phonons at the center of the Brillouin zone. The cross-section for the C-C sp^3 vibrations, when available, are negligible for visible excitation.

Upon protium plasma exposure of a single layer graphene (Figure 8.1(c) 2nd panel), a sharp D' peak around 1620 cm^{-1} appears as a result of intervalley double-resonance process due to deviation from the defectless two dimensional character, as well as a D peak around 1350 cm^{-1}. The G peak preserves its position at 1585 cm^{-1} and a significant broadening is not observed. The sharpness of these peaks signifies that amorphization is negligible [262]. A D:G height ratio of 4.5 is observed which anticipates a strong atomic rearrangement. In the work of Elias *et al.* [24], such a D:G ratio, being almost twice as much as of the ratio obtained after single surface hydrogenation, was interpreted as graphane formation. In contrast to this, the plasma exposure of HOPG results in the appearance of the D and D' peaks with lower relative intensities (Figure 8.1(d) 2nd panel), which is attributed to the contribution of the bulk layers where no hydrogenation takes place. This assumption is consolidated with the observation of a decreasing D:G ratio with an increasing number of graphene layers which were simultaneously exposed to a protium plasma (Figure 8.1(c) 3rd and bottom panels). The plasma exposure time between 5 and 60 minutes did not result in a significant difference in the Raman spectrum of the HOPG (not shown here). The D and D' peaks of the Raman spectrum of the protium plasma exposed HOPG can be reduced or completely suppressed by annealing at $450\,°C$ (soft annealing) for 30 minutes or over $1000\,°C$ for 10 minutes (hard annealing) respectively (Figure 8.1(d) 3rd and bottom panels). All annealings were performed in UHV conditions. The latter value is around $200\,°C$ lower than the theoretical calculations [265], which predict a full transformation from graphane back to graphene. In contradiction to Ref. [24], a significant change of the Raman
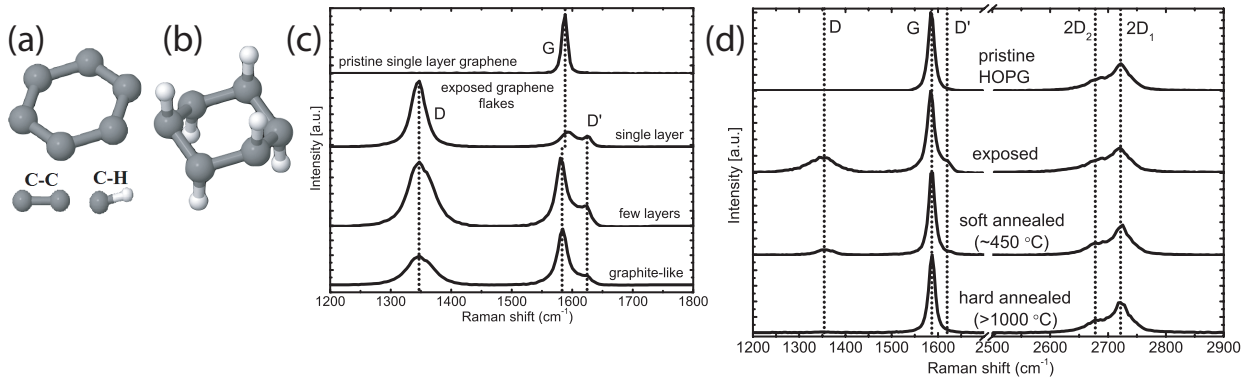
Figure 8.1: The two dimensional material consisting of carbon atoms in honeycomb orientation, graphene (a), loses its sp^2 hybridization upon hydrogenation from both sides resulting into its insulating derivative, graphane (b). This transformation might be achieved with a pure protium LTP exposure, which results in a D:G height ratio of 4.5 in the Raman spectrum of single layer graphene (c). The sample was kept at 450 °C during 5 minutes of exposure, where the same plasma exposure results in a smaller D:G ratio for multilayer graphene (c) and for HOPG (d), due to contributions from pristine layers beneath protium implantation depth. Soft annealing at 450 °C diminishes the D and D' peaks; however a complete suppression, which signifies reversibility to graphene, is achieved only after an annealing over 1000 °C.

spectrum of LTP exposed single layer graphene was not observed after it was being annealed at 400 °C for 24 hours in an argon atmosphere.

8.3.2   Atomic force microscopy

Though Raman spectroscopy is a strong tool for the analysis of graphitic materials, it does not provide direct evidence of hydrogenation. In order to understand the nature of the D and D' peaks of the Raman spectra, AFM and photoemission spectroscopy of HOPG were conducted before and after exposing it to plasma. Electron microscopy on the HOPG samples is avoided because the electron beam energy might ionize H_2O and NH_3 adsorbates and cause additional effects [266]. Although the pristine HOPG exhibits a relatively flat surface, the protium plasma exposed HOPG shows two important differences: (i) The surface becomes rougher, (ii) blisters start to form which are more pronounced for longer time plasma exposures (Figures 8.2(a) and (b)). Regarding these AFM measurements, it is clear that both surface roughening and blister formation contribute to D and D' peaks of the Raman spectrum. The surface roughening can neither be attributed to physical sputtering since the impact energy of the ions is well below theoretical threshold ($\epsilon_i \sim 36$ eV) [6, 247], nor to chemical etching which would have been formed large hexagonal pits [259, 267]. The author thinks that some of the implanted atomic and molecular protium ions recombine to form protium gas intercalated between two graphite layers which builds up mechanical stress and deforms the entire surface. Moreover, this gas is free to diffuse in the lateral direction between the layers [268], which results in accumulation of protium gas at certain points. Subsequently, the graphite layers start to deform more rigorously and blisters start to appear on the surface. The different phase contrast of the blisters from the rest of the surface suggests that they have different local elastic properties than elsewhere on the
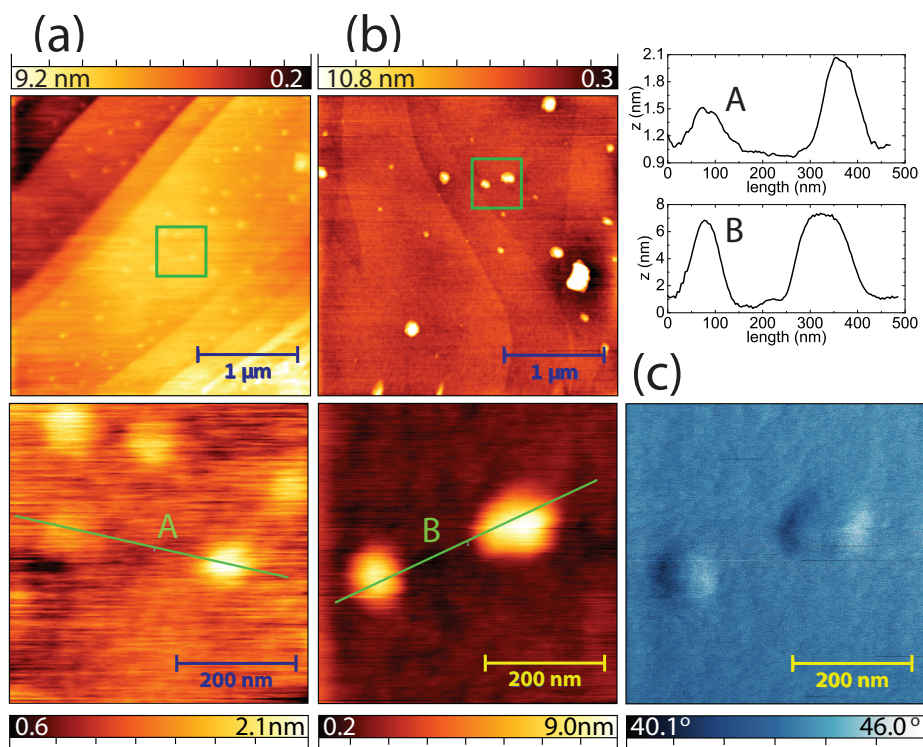
Figure 8.2: AFM measurements of the HOPG after hydrogen plasma exposure at 450 °C, where round shaped blisters appear on the topography images of the HOPG surface, with a relative height depending on the plasma exposure time ((a) 5 minutes, (b) 60 minutes). Line profiles of two blisters in (a) and (b) are presented as A and B. Blisters also reveal a phase contrast different from the rest of the surface (c). Nanosurf FlexAFM device was used.

HOPG (Figure 8.2(c)). It is, however, not clear whether these blisters still contain hydrogen gas underneath them during storage of HOPG in ambient conditions. Similar blister formation was observed after thermal sorption of hydrogen into graphite and hydrogen gas storage was claimed via thermal desorption experiments [269]. AFM topography images of single layer graphene on SiO$_2$ do not reveal any significant roughening or blister formation (shown in the next chapter). The changes in the Raman spectrum of graphene is solely due to atomic rearrangements, either as a result of hydrogenation or corrugation at the atomic level. Since it was shown that low energy argon plasma treatment also results in similar atomic rearrangements due to corrugation [258], but not to a rise of the D peak [24], it can be claimed that protium plasma treatment of the graphene layer results in its hydrogenation.

8.3.3   Photoelectron spectroscopy

X-ray and ultraviolet photoelectron spectroscopy (XPS and UPS) were used to monitor the changes in the core level and valence band structures of the HOPG after plasma exposure and subsequently after soft annealing. After exposure to protium plasma, the core level C 1s spectrum gets broadened due to roughening, whereas it recovers its initial width after soft annealing (Figure 8.3(a)). It was already stated that even when there is C-H bonding, this change in the shape of the C 1s peak is not due to a chemical shift as a result of this bonding, but is rather due to the increase in the difference between the upper valence band edge and E$_f$ [270]. Such a broadening was also observed for HOPG which was exposed to a low energy argon plasma, and the reason behind it was stated as geometrical defects (roughening) without any contribution from vacancy formation or hydrogenation [258]. In a similar manner, the broadening of the C 1s peak in the current case is also due to displacement of the carbon atoms and its recovery is due to flattening after soft annealing. The shake-up satellite peak due to π-π^* transition exists for all the spectra (Figure 8.3(a) inset).

As previously studied [270–272], the valence band spectrum of pristine HOPG (8.3(b) upper panel) contains 5 peaks around 3.2, 5.3, 6.7, 8.5 and 14.2 eV below E$_f$. The peak at a B.E. around 14.2 eV is a secondary peak arising from photoelectrons inelastically scattered into unoccupied states. The peak at a B.E. of 3.2 eV is attributed to π bonds which makes graphite a semimetal. The other three peaks lie where the π and σ bands overlap but they have their contribution mainly from the σ band. After exposure to hydrogen plasma, the UPS spectrum looks very similar to the spectrum obtained 20 years ago by Ugolini *et al.*, where HOPG was exposed to hydrogen ions of a Penning ion source [270]. From this spectrum (8.3(b) middle panel) alone, an energetically favorable hydrogenated network of carbon atoms was suggested even at that time. The π peak at 3.2 eV still exists, denoting that the structure still has some aromatic nature (not fully saturated with protium). The remnant of the secondary peak indicates that the structure still consists of carbon rings. Since the UPS spectrum of graphite is highly dependent on the polar angle (i.e. the angle between the entrance slit of the analyzer and surface normal) [273], intensity contributions from different polar angles are smeared out and appear as one broad peak 7 eV below E$_f$ as a result of surface roughening after plasma exposure. After soft annealing (8.3(b) bottom panel), the secondary peak rises due to the flattening of the layers. The broadening effect is reduced and the σ peaks reappear at shifted positions of 8.3 and 10.2 eV below E$_f$. As suggested by the theoretical calculation of hydrogenated graphite from Allouche *et al.* [272], full hydrogenation of graphite results in a σ band structure very similar to diamond, an sp^3 hybridized carbon allotrope [271, 274]. From this point of view, it
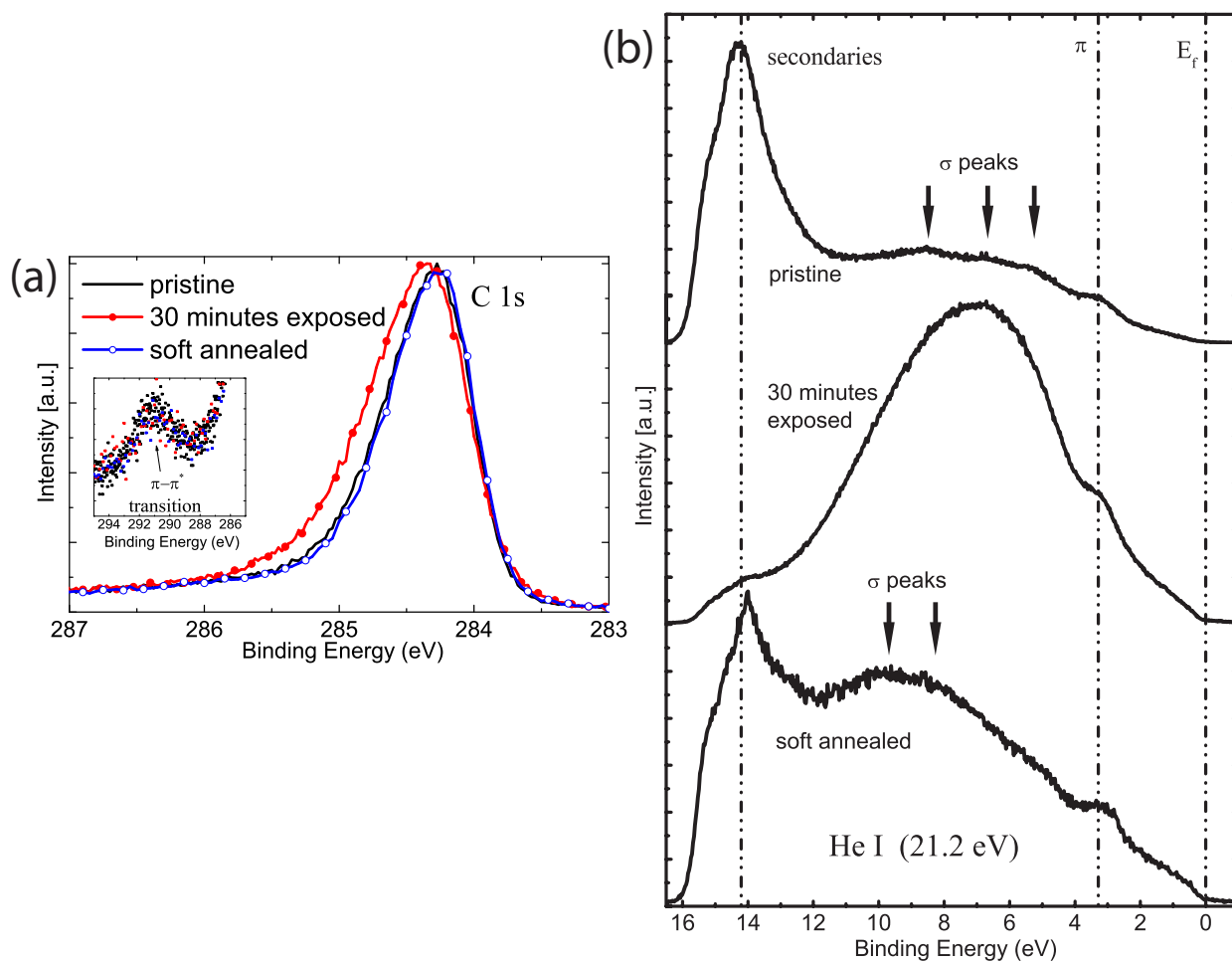
Figure 8.3: XPS (a) and UPS (b) spectra of the HOPG before exposure, after 30 minutes of exposure and after an annealing at 450 °C were used to monitor the transformation from graphene to hydrogenated graphene. In (b), the positions of the π and the σ peaks, and the eyeguides for E_f and the secondary electrons are provided.

can be claimed that this UPS spectrum is the valence band spectrum of hydrogenated HOPG, containing some features analogous to those of cubic diamond. In the next section, it is shown that the surface still has slight corrugation, which could also have a small contribution to the UPS spectrum as the remnant of the broad peak at 7 eV. After soft annealing, the D and D' peaks in the Raman spectrum of the HOPG are diminished (8.1(d) 3rd panel), where this partial suppression is due to flattening; however the contribution from the atomic rearrangement of the C atoms, which is possibly due the C-H bonding, is still present. The shift of the σ peak positions towards sp^3 hybridization proves this assumption.

8.3.4   Scanning tunneling microscopy and spectroscopy

In order to corroborate the discussions in spectroscopy techniques further, STM was used. STM image of pristine HOPG consists of a hexagonal pattern generated by the charge density of the electrons [275]. As it is shown in Figure 8.4(a), these patterns appear as triangles due to coupling with the other layers as a result of AB stacking. After exposure to protium plasma, the surface still consists of a hexagonal pattern but on a highly corrugated plane (Figure 8.4(b)). Soft annealing leads to a flatter surface. However it still has a corrugation in the form of ripples and valleys at certain points (Figure 8.4(c)). This surface corrugation matches well with the theoretical calculation of a suspended graphane layer, which predicts a corrugation in the form of ripples with an amplitude of a few hundred picometers [265]. The hexagonal ring patterns in Figure 8.5 appear in different distorted forms. The STM images in the current work are similar to those obtained locally around the step edges of graphite, where the step edges were terminated with atomic protium [276]. Since STM probes the local DOS [275], this distortion in the ring patterns might arise from surface corrugation [276]. On the other hand, it should not be disregarded that graphane has different possible stable C-H conformations and these conformers do have distorted ring structures [22, 23], which might also explain the variety of different distorted STM contrasts observed even on relatively flat surfaces. Moreover, it can be seen that the same atomic patterns can be observed on both light and dark contrast sites. It can also be observed from Figures 8.4(b) and (c) that the triangular appearance of the surface due to AB stacking dissapears, and the hexagonal features become visible. This suggests a decoupling of the surface layer from the rest of the layers, either due to hydrogenation, due to hydrogen gas inside the graphite lamellae, or due to both of them simultaneously.

The STM results confirm that a new network of carbon atoms on a rippled plane, different from surface [256] and local step edge hydrogenations [276] was obtained. However, it has to be mentioned that before the introduction of hypothetical graphane in 2007, a very similar protium LTP exposure to the one presented here was performed by Ruffieux *et al* [277]. With the STM method, they recorded very similar current patterns. They have attributed these patterns solely to defects induced by the hydrogen plasma. With respect to this point, STM method by itself is not conclusive enough to substantiate the claim of hydrogenation of HOPG.

STS measurements done on relatively flat parts of the surface reveal a very different characteristic from the typical V-shape of graphite (Figure 8.6(a)) [278], where two distinctive features can be observed. The first one is the bandgap-like feature at E_f, which is reported to occur as a result of opening of an inelastic tunneling channel via the excitation of out-of-plane phonons at the K/K' points of the graphene reciprocal lattice [279]. Assuming that the surface layer is decoupled from the rest, observation of such a phenomenon is comparable to the previous observations of the same phenomenon for single layer graphene on insulating surfaces [280].
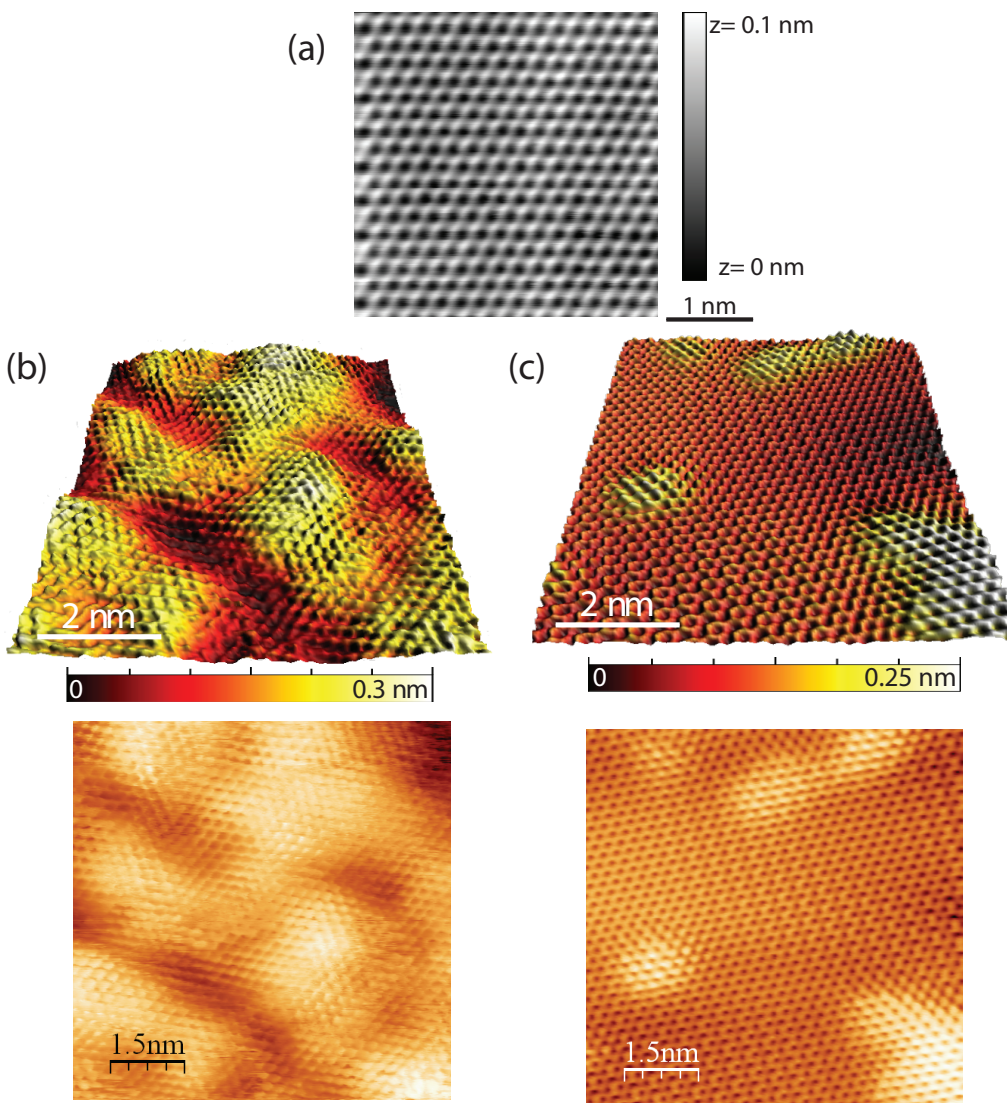
Figure 8.4: (a) STM image of pristine HOPG surface consisting of hexagonal patterns appearing as triangles. STM images of the HOPG after 5 minutes of hydrogen plasma exposure at 450 °C (b) and after an annealing at 350-400 °C for 60 minutes (c), clearly show the flattening of the surface as a result of soft annealing. In (b) and (c), the hexagonal rings appear more clearly than (a), possibly due to decoupling of the surface layer from the rest of the surface. Parameters used for imaging: $V_{tip} = 50$ mV and $I = 70$ pA.
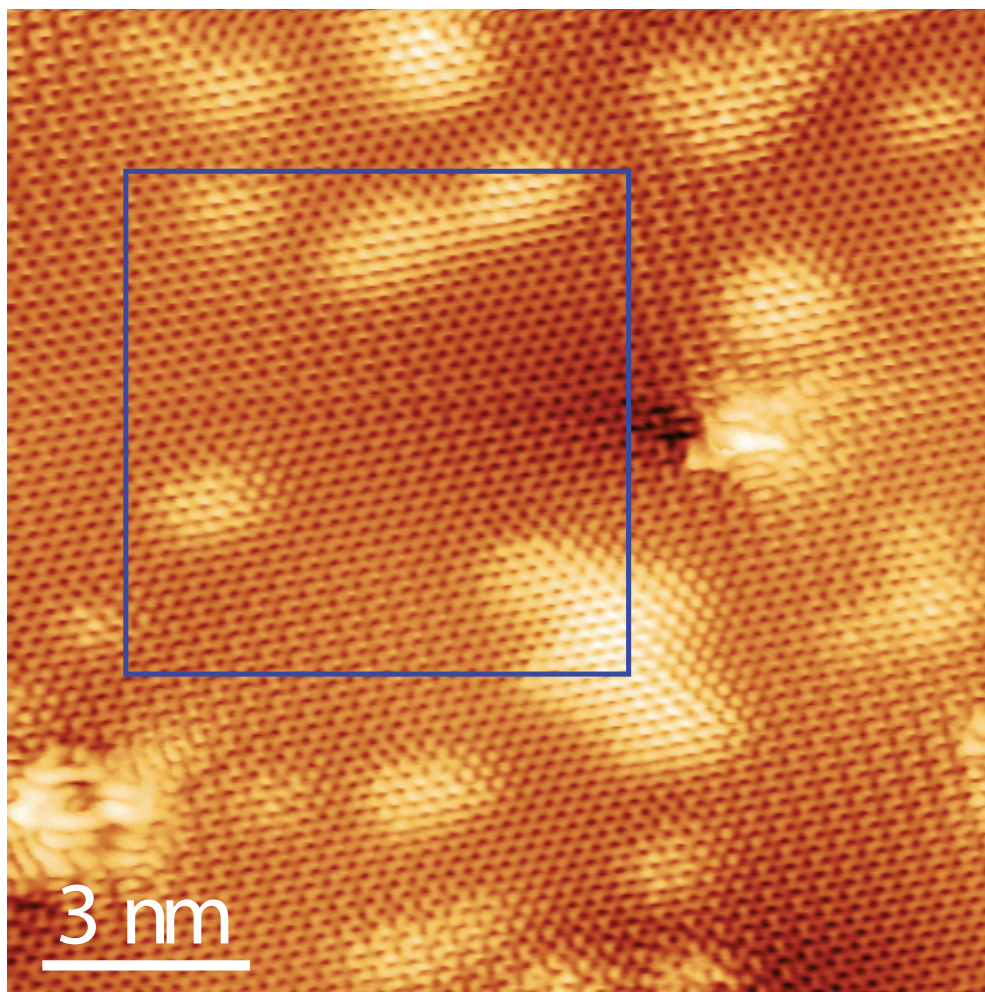
Figure 8.5: STM image of the surface consisting of various atomic-scale patterns where a very low defect density can be observed. The inset is also shown in Figure 8.4(b).

The second feature is the opening of a bandgap of 80 meV (Figure 8.6(b)). This value is lower than the expected values of around 3.5 eV for hypothetical graphane calculations [281–283]. The difference is due to the geometrical imperfections (corrugation) of the surface, defect states, hydrogen deficiency [284] and conductive surface states due to this hydrogen deficiency [272]. There is also a $T^{1/3}$ dependence of the electron mobility reported in literature [24, 55], which suggests a thermally activated conduction mechanism due to defect and hydrogen deficiency states lying in the bandgap. In respect to such a thermal dependence of the electron mobility, a separate STS study at 4 K, possibly on different STM patterns, has to be performed in future. The STS spectrum in Figure 8.6(b) also shows a 150 meV separation between the Dirac point and E_f, suggesting an n-type of doping due to hydrogenation [280]. Substracting the energy of the inelastic phonon excitation of 63 meV [279], the actual shift of the Diract point can be estimated as around 90 meV. In the next chapter, the doping character of graphene as a result of hydrogen attachment is analyzed more in detail.
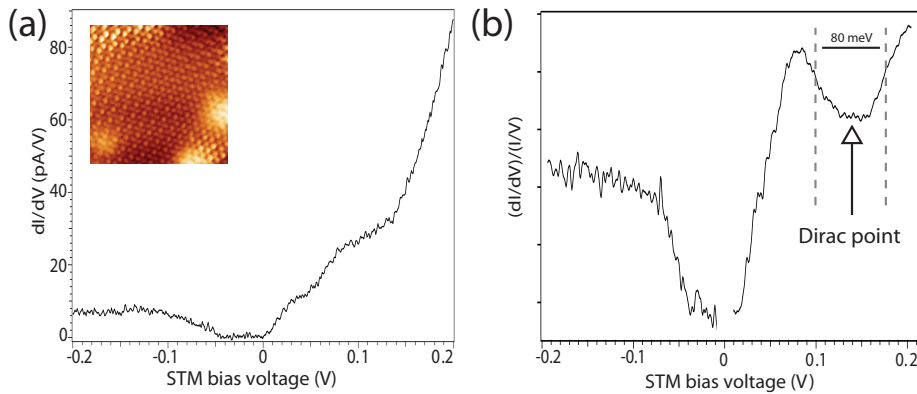

Figure 8.6: An example of a typical STS spectrum (a), which was acquired above a flat area (inset) reveals a relative bandgap of 80 meV after normalization (b).

8.4 Outcomes

1. Protium LTP exposed HOPG and graphene have been characterized with various techniques including photoelectron spectroscopy, Raman spectroscopy, scanning probe microscopy and spectroscopy. Protium LTP exposed HOPG surface consists of various atomic scale STM patterns, which may be due to different possible C-H conformations of hydrogenated graphene layers. On the other hand, surface corrugation or point defects caused after LTP exposure also have a contribution to these patterns. Regarding its valence band structure measured with UPS, protium LTP exposed HOPG has similar features to cubic diamond. Raman spectroscopy of hydrogen LTP treated single layer graphene reveals a

D peak to G peak ratio over 4, which is due to hydrogenation. Graphane is a reserved word for graphene which is hydrogenated from both sides. Though such case cannot be perfectly realized due to the hydrogen deficiencies and point defect created during the plasma treatment, the presented results, when considered all together, point to double side hydrogenation of the graphene layers.

2. Graphite might be an alternative solution for hydrogen storage. Since protium LTP exposed HOPG possesses a high thermal stability, unloading of chemically stored hydrogen requires annealing over $1000\,^\circ$C which may not be very feasible. However, protium gas which had caused blisters on the surface might still be stuck between the graphane layers, where the required unloading temperature is around $450\,^\circ$C.

Chapter 9

Properties of protium plasma treated graphene

In the previous chapter, protium plasma treated HOPG was characterized using various methods. In summary, the valence band structure and the surface electron density of HOPG, as well as the vibrational modes of both graphene and HOPG were found to have changed, which was attributed to hydrogenation of the graphene layers. In this chapter, a silicon stencil mask with a periodic hole structure was used in order to pattern altered and pristine graphene, which was grown by chemical vapor deposition (CVD) and transferred onto a Si/SiO_2 (p-doped Si, SiO_2 thickness is 86 nm) wafer. Raman and Kelvin probe force microscopy were used to image these patterns, indicating the changes in the vibrational modes and CPD after protium plasma treatment.

9.1 Experimental preparations

Single layer graphene was grown on a copper foil in a split quartz tube furnace using a CVD method involving methane and protium gases [285]. Transfer of the graphene layer onto the Si/SiO_2 substrate was achieved by the standard procedure involving PMMA coating, dissolving the copper foil in an iron nitrate solution, 'fishing' the polymer with the substrate, and the removal of PMMA in acetone [285]. The obtained graphene layers (with a size of more than 1 cm^2) showed a very weak response to pH changes, manifesting their quality thanks to the scarcity of defect-induced dangling bonds [286]. The protium plasma treatment with an electron temperature of 3.5 $\pm$ 0.5 eV and an ion flux of 1.5 $\pm$ 0.5 $\times$ 10^{15} $cm^{-2}s^{-1}$ was performed at Facility-II. The sample was kept electrically floating during 5 minutes of exposure. With this technique, proton deposition energies can be obtained which are high enough to overcome the energy barrier (3.7 eV) to penetrate the center of the hexagonal carbon [246], without physically sputtering (36 eV) the carbon atoms [247].

9.2 Results and discussion

Upon protium plasma exposure, a sharp D' peak around 1625 cm^{-1} appears in the Raman spectrum as a result of intervalley double-resonance process due to deviation from the defectless
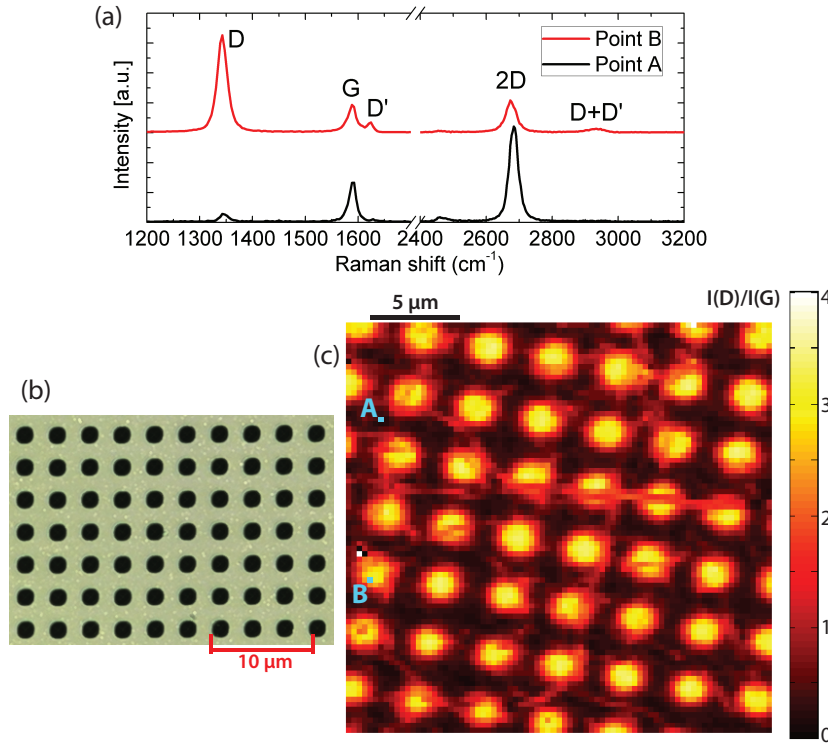
Figure 9.1: (a) Typical Raman spectra of covered (black) and plasma treated (red) parts of graphene supported on Si/SiO$_2$. (b) Optical microscope image of the silicon stencil mask used for plasma microlithography. (c) 20×20 μm^2 (80×80 pixels) Raman microscopy of patterned graphene, showing a clear increase of the D peak to G peak intensity ratio at the plasma treated areas.

two dimensional character as well as an increase in the D peak intensity (Figure 9.1(a) - red line). A negative shift can be observed at the 2D peak position after plasma treatment. This shift suggests an increase in the electron concentration (i.e. an upper shift of E$_f$) [287], suggesting electron donation from chemically bound protium atoms. However, the G peak preserves its position at 1590 cm^{-1}. The sharpness of the peaks signifies that amorphization is negligible [262].

Due to these differences of the Raman spectrum before and after exposure, monitoring the intensity ratio of the D peak to the G peak is an adequate solution for imaging the exposure patterns. A 20×20 μm^2 image was obtained by scanning the x-y stage with steps of 250 nm. An integration time of 1 second was used for each pixel. The Raman microscopy image showing the intensity ratio I(D)/I(G) (Figure 9.1(c)) of the hydrogen plasma exposed single layer graphene reveals the general shape of the patterns of the stencil mask (Figure 9.1(b)). A clear increase of this ratio of up to 4 was observed at the plasma treated areas, proving that the protium plasma microlithography of graphene can successfully be applied. This ratio was also obtained in various works involving protium plasma and was correlated with hydrogenation of graphene [24,55,56].

To address the question of the origin and the properties of the treated areas, KPFM was applied, which provides combined information on the topography and the surface potential. A

strong topographic corrugation related to plasma induced defects might be the origin of the increase in the D peak intensity. However, for a local hydrogenation of graphene, a change of WF in such areas is expected and can be measured by variations of CPD [288].

Figure 9.2 shows topography and CPD images of the untreated graphene layer transferred onto a Si/SiO_2 substrate measured by KPFM using a Nanosurf FlexAFM operated in ambient conditions in a controlled dry nitrogen atmosphere in a glove box. The scan range of the measurement was $10 \times 10 \ \mu m^2$. A commercially available Nanosensors PPP-EFM silicon cantilever with a Pt/Ir coating was used. The fundamental cantilever resonance frequency ($f_{1^{st}}$ $\sim$ 62 kHz) was excited to obtain topographical information, whereas the second flexural cantilever resonance ($f_{2^{nd}} \sim$ 400 kHz) was used for the CPD detection in the intermittent contact regime [289, 290]. While the AC voltage exciting the electrostatic force modulation was applied to the sample, the DC voltage was applied to the tip. The CPD data are represented in such a way that the bright areas correspond to areas with a larger work function values.

The measurements can be used for the estimation of the absolute WF. Under the assumption that the AFM tip remained unchanged before acquisition of Figure 9.2, Pt/Ir coated tips used in this thesis have a work function of 4.28 eV [291], revealing a WF of around 4.75 eV for the as prepared graphene on Si/SiO_2. Of course, this value may not be accurate and it can vary 100's of meV depending on the conditions of the tip, however the precision of the CPD variation is in the order of 10 meV. The work function of graphene supported on a Si/SiO_2 substrate, in the simplest picture, is the sum of the work function of free-standing graphene (4.23 eV [292, 293]) and the energy gain due to the surface charge density. This surface charge density is induced by electrostatic charging and charge rearrangements in the proximity of SiO_2, including the effects from the surface/interface contaminants. This, in a way, can be interpreted as p-type doping of graphene [21], as it is donating electrons into SiO_2 and/or to the contaminants at the interface. This process results in a downward shift of E_f, hence an increase in the work function of graphene [292]. Using the equation given in Ref. [292], it can be very roughly estimated that graphene is doped with 2×10^{13} holes/cm^2 for a V_f of 10^6 m/s. A recent KPFM measurement of the work function of graphene on 300 nm SiO_2 was reported to be 4.57 eV [294]. However, another recent study predicts rather an n-type behavior of graphene supported on Si/SiO_2, after removal of adsorbed gases in UHV [293]. In this respect, it can be anticipated that the hole doping originates from the surface/interface contaminants, e.g. water.

The pristine graphene films show some microscopic ripples and round-like protrusions with heights of up to 50 nm (Figure 9.2(a)). The ripples are due to the stress in the graphene film, generated during cool-down after CVD growth as well as imperfections during transfer onto the Si/SiO_2 substrate. Two of the ripples can also be observed in the same image with lower CPD values (Figure 9.2(b)). The ripples do not have contact with SiO_2, which results in a weaker electrostatic charging of graphene and therefore, they are observed as zones with a lower WF. Alternatively, these two ripples might also be domain boundaries of graphene, which are in fact bilayer graphene because of the overlap of two graphene layers. Similarly, in the Raman map presented in Figure 9.1(c), some ripple-like features are also present due to the increase in the D peak intensity. The round-like protrusions are left overs of the PMMA polymer during the transfer onto SiO_2, resulting in a reduced CPD of up to 80 meV.

Figure 9.3 shows the topography and CPD images of masked graphene after plasma exposure. The topography image shows no structural effects created by the plasma exposure, whereas the CPD image clearly reflects the patterns of the stencil mask used. This result shows the strength
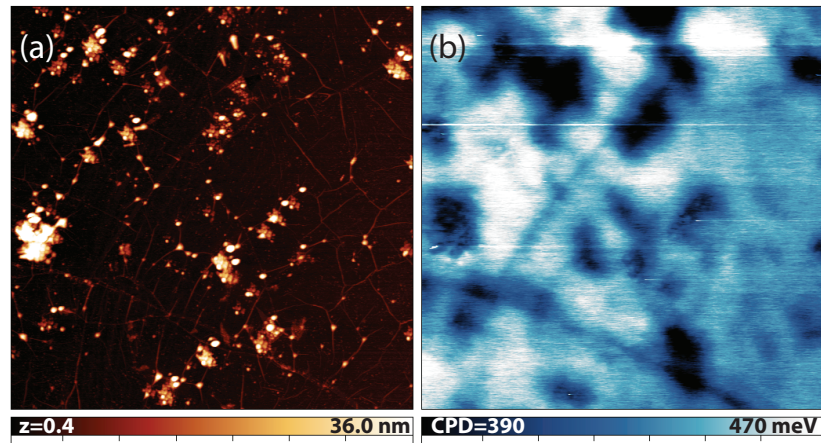
Figure 9.2: $10 \times 10 \ \mu m^2$ (a) topography and (b) CPD images of the pristine graphene layer supported on a Si/SiO_2 substrate, measured in a dry nitrogen atmosphere.
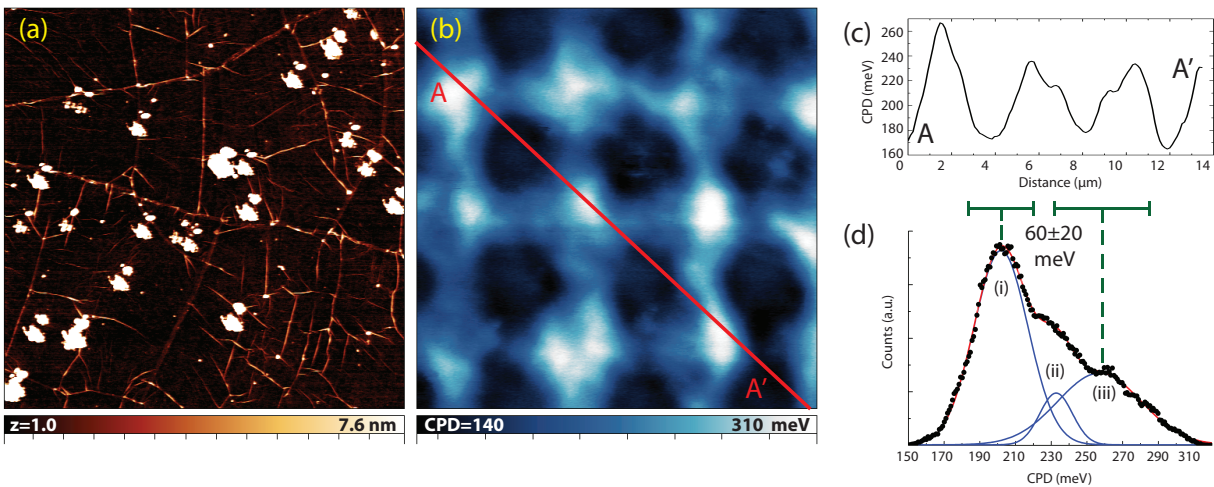

Figure 9.3: $10 \times 10 \ \mu m^2$ (a) topography and (b) CPD images of CVD grown graphene patterned with hydrogen plasma microlithography. Darker CPD contrasts are the plasma exposed areas. (c) CPD profile of the A-A' line in (b). The histogram of (b) is shown in (d), in which the three Gaussian peaks correspond to 3 different contrasts of the CPD image. The difference between peaks (i) and (iii) which correspond to the dark and bright areas is 60 ± 20 meV. Peak (ii) is due to the averaging effect and corresponds to the areas in between dark and bright areas.
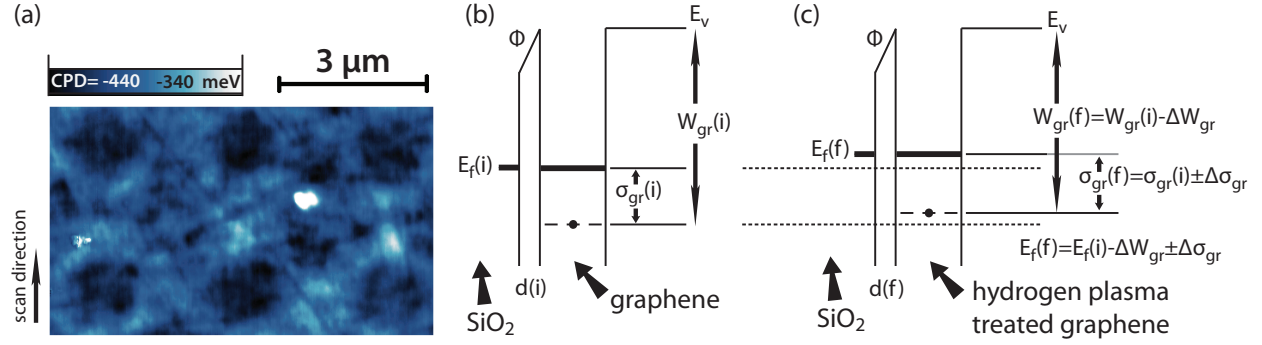
Figure 9.4: (a) CPD measurement in UHV. Potential diagram of graphene supported on Si/SiO_2 (b) before and (c) after protium plasma treatment. W_{gr} denotes the work function of a free standing graphene. ϕ is the potential drop across the graphene SiO_2 interface. E_v and E_f are the vacuum level and the Fermi level, respectively. σ_{gr} is the energy loss due to the surface charge density of graphene created as a result of electrostatic charging at equilibrium distance d with respect to the substrate. Subscripts i and f denote the pristine and protium plasma treated graphene, respectively.

of KPFM by resolving local work function variations, which appear solely due to chemical modifications of the surface, without any topographical contribution. The exposed areas exhibit patterns with reduced CPD of 60 ± 20 meV (Figure 9.3(b), (c) and (d)), indicating a lower WF for the protium plasma treated areas. A small averaging effect might even further increase the variation of CPD by several 10's of meV [295].

Finally, in order to address the effects of the surface and interface contaminants, the KPFM measurements were repeated in UHV conditions using a home-built AFM operated in constant height mode and a Nanonis control unit. Though the absolute work function of graphene on SiO_2 decreased gradually during storage in UHV, the relative CPD contrast between the hydrogen plasma treated and untreated areas remained unchanged. Furthermore, in order to degas/desorb the contaminants out from the interface more efficiently, the sample was annealed at 130 °C for 1 hour. Figure 9.4(a) shows the KPFM image, where the absolute work function of graphene on SiO_2 can be estimated as ∼3.9 eV, with a reduction of ∼60 meV for the hydrogen plasma treated zones. This result confirms the predictions that single layer graphene should have a net electron transfer from SiO_2 in the absence of any interface impurities [293, 296]

Figure 9.4(b) shows a model of a potential diagram of graphene on SiO_2. In this picture, WF of graphene supported on a Si/SiO_2 substrate is the sum of WF of a free standing graphene (W_{gr}) and the change in the surface potential ($-\sigma_{gr}$) in the proximity of SiO_2: E_v-$E_f(i) = 3.9$ eV $= W_{gr}$ - σ_{gr}. Figure 9.4(c) represents the potential diagram where the effects of protium plasma treatment of graphene are addressed. As free-standing graphene starts to be decorated with protium atoms from both sides, there is an upward shift of its E_f [288], which is represented as ΔW_{gr} in this model. This can be understood in terms of electronegativity, where less electronegative protium atoms behave like electron donors. In addition to this, hydrogenated graphene would also experience different electrostatic charging from the SiO_2 support, represented as $\Delta\sigma_{gr}$. With respect to the last point, variation in the measured CPD reflect the change of WF of graphene with a modulation related to the difference in electrostatic charging: ΔCPD
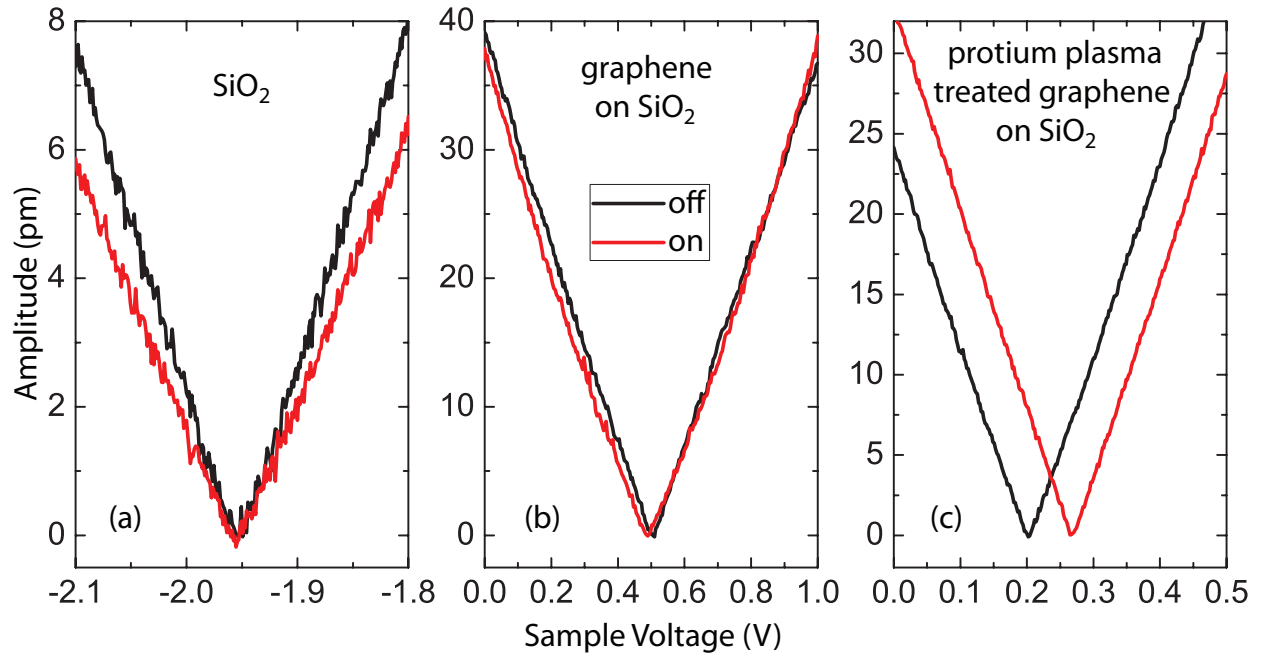
Figure 9.5: Bias voltage spectroscopy of (a) protium plasma exposed SiO_2, (b) CVD grown graphene on SiO_2 and (c) CVD grown graphene-on-SiO_2 after protium plasma exposure. CPD of SiO_2 and graphene remains invariant to white light illumination, whereas protium plasma treated graphene clearly shows a shift in the work function suggesting that it has a photoresponse.

$$= 60 \pm 20 \text{ meV} \leq E_f(i) - E_f(f) = \Delta W_{gr} \pm \Delta \sigma_{gr}.$$

9.3   Effects of white light illumination

Although hydrogenated graphene is predicted to exhibit a bandgap of 3.5 eV (discussed in Chapter 8), the characterizations performed at RT are far away from showing any insulating character. In fact, the typical $T^{1/3}$ dependence of the electron mobility of hydrogenated graphene reported in literature [24, 55] was also measured in my samples. Although hydrogenation does not result in an overall semiconducting character, some local hydrogen induced or defect induced states with an optical gap might be generated. Such states would have a tendency of photocurrent creation following a photon absorption in the visible range. As the first illumination test, a white LED source with a wavelength range between 1.8 and 3.1 eV was used. Figure 9.5 shows the bias spectroscopy performed on the plasma exposed bare substrate, graphene on SiO_2 and plasma exposed graphene on SiO_2. While SiO_2 and as-prepared graphene remain invariant to white light illumination, the plasma exposed graphene reveals a prominent shift in its CPD. This result suggests that the hydrogenated graphene has a photoresponse, and might be somehow a photoactive material. Further work with a variable wavelength source is necessary in order to understand the nature of such a behavior.

9.4 Outcomes

In summary, protium plasma microlithography on graphene was successfully employed. The obtained results can pave the way to nanolithography of graphene prepared by hard mask techniques. Raman and Kelvin probe force microscopy techniques were utilized for imaging the lithography pattern of graphene. Moreover, an absolute WF of around 3.9 eV was measured for single layer graphene supported on a Si/SiO_2 substrate, whereas this value is as high as 4.75 eV for as prepared single layer graphene on Si/SiO_2 due to hole doping from the surface and interface contaminants. Finally, it is shown that the protium plasma treatment of graphene on SiO_2 results in a WF reduction of around 60 ± 20 meV, which is explained by hydrogenation of the graphene layer. This may be an important step forward for the understanding of the properties of hydrogenated graphene.

Chapter 10

Conclusions and Outlook

10.1 Summary

This thesis was devoted to the study of the electronic, mechanical, optical and chemical properties of transition metals and layered carbon materials treated with hydrogen plasma. The first part of the thesis consisted of Chapters 1 and 2, which provided necessary theoretical and experimental notions for the reader. The second part of the thesis consisted of Chapters 3, 4, 5, 6 and 7, and dealt with transition metals exposed to hydrogen plasma. Among these, Chapters 3 to 6 were dedicated to deuterium plasma exposure of molybdenum and rhodium, the materials which are planned to be used as the first mirrors in the new generation nuclear fusion reactor ITER. Chapter 7 presented results from gold coatings treated to protium plasma, in order to address certain mechanical issues which can be encountered when transition metals are treated with hydrogen plasma. The third and last part of the thesis consisted of Chapters 8 and 9, discussing the hydrogenation of layered carbon materials as a result of protium plasma treatment.

10.2 Outcomes of the thesis for the fusion community

Optical characterization of deuterium plasma exposed molybdenum and rhodium in the fusion community was limited to *ex situ* reflectivity measurements performed after exposure in various tokamaks. This, of course, has some predictive power in terms of estimating the severity of reflectivity degradation of the FMs which will be placed in ITER. However, the descriptive power of such results is often limited due to the complexity of the plasma mixture in tokamak environments. Therefore, *in situ* characterizations during controlled plasma exposure were necessary to establish the physical phenomena, which can be responsible for the reflectivity degradation observed in tokamak experiments. For instance, in Chapter 3 of this thesis it was shown that reflectivity degradation observed in the 2009 TEXTOR campaign of Mo mirrors was mostly due to the effects of pure deuterium. Hydrogen in transition metals may act as an electron acceptor or donor, which can change the electronic structure of the host material even without any bond formation. As a result, the optical absorptions of the metal associated with interband transitions will also change. Moreover, hydrogen plasma treatment also introduces defect sites (e.g. vacancies, lattice distortions) in the lattice of the host material, increasing subsurface scatter events and thus reducing the intraband relaxation time. It was also shown in this chapter

that the degradation of the reflectivity saturates at a certain point, and the existence of a new Mo/D system with optical properties different from those of pristine Mo was proposed. Further characterization with photoelectron spectroscopy and surface imaging techniques confirmed the conclusion that the reflectivity change is related to changes in the electronic structure and not due to surface roughening. Chapter 4 extended the results of Chapter 3 by exposure of Mo mirrors to high flux deuterium plasma to roughen the surface, causing an increase of the diffuse reflectivity. The changes in the surface roughness were explained with linear and nonlinear Bradley-Harper models for metals, suggesting that the increase in surface roughness saturates after certain fluence is reached. In the same chapter, delamination of coatings from the substrate as a result of high flux deuterium plasma exposure was also shown to be a possible risk, which can, however, be suppressed at elevated sample temperatures relevant to ITER. In summary, all Mo mirrors in ITER will be subject to an initial degradation of the reflectivity due to the presence of deuterium and deuterium plasma induced defects in its lattice. Mirrors in erosion conditions may also be subject to surface roughening, but this will be an interplay of physical sputtering and surface diffusion and, therefore, can be minimized at high temperatures. If the mirror material will be a coating, temperatures below 100 °C pose a very serious delamination risk, which may lead to failure of the diagnostic unit.

The story is different for Rh exposed to deuterium plasma. The *ex situ* measurements performed after deuterium plasma exposure exhibited no significant change in the reflectivity, whereas a constant decay was observed during *in situ* measurements. It was claimed in Chapter 5 that the reflectivity degradation during plasma exposure is due to formation of a subsurface rhodium deuteride layer, with optical constants different from those of metallic Rh. The results were complemented with UPS measurements performed without breaking the vacuum, suggesting an electron donation from deuterium to Rh, filling the Rh 4d states above the initial E_f. As a result, E_f shifts to higher energies and the number of states above E_f decreases, causing a reduction in optical transitions and consequently a decrease in the reflectivity of Rh. Reflectivity recovery was possible after storage in air due to a catalytic reaction between oxygen and deuterium adsorbed on the surface, enabling deuterium permeation from the Rh surface to air. This is the reason why no reflectivity degradation was reported so far with *ex situ* measurements. Irreversible mechanisms such as surface roughening or deuterium which is strongly bound to defect sites in the Rh lattice have a negligible contribution to the reflectivity degradation.

Chapter 6 is the last chapter dealing with the first mirror problem in ITER. The ITER plasma will contain deuterium and tritium, together with fusion by-products (e.g. helium) and impurities sputtered from the wall materials (tungsten, beryllium and possibly carbon). Of course, the most abundant element in the ITER plasma will be deuterium and, therefore, its effects on metal reflectivity were discussed thoroughly in Chapters 3, 4 and 5. Here, several possible impurity situations were experimentally simulated in order to address the severity of the reflectivity degradation caused by plasma impurities. In net erosion conditions, reflectivity degradation was similar to the case of pure deuterium exposure. In net deposition conditions involving tungsten and carbon, the reflectivity degradation was high. In net deposition conditions involving tungsten and aluminum (a substitute for beryllium), the degradation in the reflectivity was low due to very low optical thickness of aluminum oxides. The deposition rate used in this work was rather low due to the low sputtering yield of Al with pure deuterium, resulting in an amorphous structure of the deposits. When some argon was added into the chamber, deposition rate had increased significantly and crystalline $Al\text{-}AlO_x$ deposits were formed. Such

deposits were very rough, decreasing the specular reflectivity significantly due to a substantial increase in the diffuse reflectivity. Our group is currently working on plasma and laser cleaning methods for removing such deposits from the mirror surfaces while minimizing the damage on the mirror surface. The most critical challenge which we have tackled successfully was removing the deposits with an oxide character, which charge up significantly during the plasma cleaning process.

10.3   Further work regarding the first mirrors

The author believes that the effects of implanted deuterium on the metal reflectivity are well established in this thesis. However, there are other critical problems regarding FMs in ITER, which remain to be solved. The current ITER plasma mixture models predict that most of the FMs will be under net deposition conditions. In this case, the mirror reflectivity would suffer from the rough deposits grown on the surface; requiring urgent development of the *in situ* cleaning methods to be operated in the diagnostic modules. In the scientific articles of Dr. Marco Wisse and in the master thesis of Lucas Moser at the University of Basel, it is shown that both laser and plasma cleaning can be successfully applied even to carbon free deposits with a metallic or oxide nature. The next challenge to be tackled at the University of Basel is the adaptation of our successfully developed techniques to engineering and design parameters more relevant to ITER, e.g. larger mirror size, smaller grounded electrode (outer wall), deposits including Be which are more relevant to ITER, etc.

10.4   Can hydrogen plasma cause failure of thin films: Gold example

When the compressive stress state in a thin film exceeds a certain threshold value, the film will buckle to release its stress. This may happen, for instance, during the physical vapor deposition process of a metal with highly mobile adatoms. Loading the thin film with excess hydrogen (possibly also with helium) may also lead to such kind of deformation. In this scenario, the dynamic hydrogen inventory in the film has to exceed the solubility of the film for a compressive stress to gradually build up. Although this should be a universal phenomenon for all of the metallic thin films, gold films grown by Volmer-Weber mechanism constitute a perfect example because of the following reasons: 1- Gold does not form any binary compound with hydrogen and, therefore, has a low solubility. 2- Gold has a low Young's modulus, facilitating buckling. 3- Gold films are typically (111) textured, decreasing the complexity of the system.

In Chapter 7, it is shown that the protium plasma treatment of 100 nm gold films results in their buckling in the form of well-structured, local, circular-shaped blisters homogeneously dispersed on their surface. In this scenario, the plasma is the proton source and gold film is the reservoir. The substrate acts as the sink, hence blister formation has a certain substrate dependence.

This phenomenon can result in catastrophic failure for nanotechnological applications involving thin films and hydrogen plasma. Among various methods which were tried to suppress blister formation in gold films, reducing the ion energy proved the most effective.

10.5 The new quasi-two dimensional material: Hydrogenated graphene

Starting from its isolation in 2004, graphene has been investigated extensively in the last decade thanks to its unusual electronic and mechanical attributes. A new approach is to covalently bond graphene to hydrogen from both sides in order to manufacture the hypothetical, quasi-two dimensional semiconducting material 'graphane'. This may be practically impossible, since in reality there will always be hydrogen deficiencies and point defects and the obtained material would not be a perfect graphane. Therefore, the term hydrogenated graphene is more adequate, referring to a graphene structure with an unknown number of hydrogen bonds and defects (e.g. point defects, geometrical defects, hydrogen deficiencies). The electronic character of this material would not only be a mixture of graphene and graphane, but would include many defect and hydrogen-induced states.

In Chapters 8 and 9, HOPG surface and single layer graphene exposed to hydrogen plasma was characterized, revealing some features expected from graphane: 1- Strong D peak intensity in Raman spectra due to atomic buckling associated with hydrogenation. 2- A hexagonal appearance of the surface with STM as a result of decoupling of the surface layer of HOPG from the rest. 3- Strong surface corrugations including blister formation due to plasma treatment. 4- Changes in the valence band structure, especially features resembling to those of diamond. 5- Decrease of the work function measured with STS and KPFM, associated with n-type of doping related to hydrogen bonding. Moreover, it was shown in Chapter 9 that hydrogenation can be achieved locally by using a silicon stencil mask, which can be mapped with Raman microscopy and with KPFM, without any contribution from the topographical features.

It should be accepted that graphene which is hydrogenated with plasma is not graphane; nevertheless it does indeed have certain differences from its pristine counterpart. The author is currently working on optical characterizations of hydrogenated graphene and differences in the nature of contamination of pristine and hydrogenated graphene and HOPG surfaces. These two on-going research topics aim to provide further insight into the possibility of using hydrogenated graphene in various applications in air ambient. Moreover, a new plasma source was recently added to a UHV RT-AFM at the University of Basel, which can be used to prepare hydrogenated graphene supported on metal substrates for atomic resolution imaging.

Bibliography

[1] www.iter.org.

[2] V. S. Voitsenya et al. *Rev. Sci. Instrum.*, 72:475, 2001.

[3] A. Litnovsky et al. *Nucl. Fus.*, 47:833, 2007.

[4] A. Litnovsky et al. *J. Nucl. Mater.*, 363-365:1395, 2007.

[5] G. De Temmerman. *On the lifetime of the first mirrors*. PhD thesis, University of Basel, online=http://edoc.unibas.ch/534/1/DissB_7768.pdf, 2006.

[6] Y. Yamamura and H. Tawara. *Atomic Data and Nuclear Data Tables*, 62:149, 1996.

[7] E.D. Palik. *Handbook of Optical Constants of Solids*. Academic New York, USA, 1985.

[8] M. Balden *et al. J. Nucl. Mater.*, 329-333:1515, 2004.

[9] A. Bardamid *et al. Vacuum*, 58:10, 2000.

[10] B. Eren *et al. Fus. Eng. Des.*, 86:2593, 2011.

[11] M. Matveeva *et al.* Material choice for first iter mirrors under erosion conditions *37th eps conference on plasma physics. Europhysics Conference Abstracts*, 34A:P2.105, 2010.

[12] A. Litnovsky *et al. Fus. Eng. Des.*, 86:1780, 2011.

[13] B. Eren *et al. Nucl. Fus.*, 51:103025, 2011.

[14] B. Eren *et al. Nucl. Fus.*, 53:113013, 2013.

[15] L. Marot *et al. Rev. Sci. Instrum.*, 78:103507, 2007.

[16] L. Marot *et al. Surf. Coat. Tech.*, 202:2837, 2008.

[17] B. Eren *et al. Appl. Surf. Sci.*, 273:94, 2013.

[18] B. Eren *et al. J. Nucl. Mater.*, 438:S852, 2013.

[19] B. Eren *et al.* Submitted for publication, 2013.

[20] A.K. Geim and K.S. Novoselov. *Nature Mater.*, 6:183, 2007.

[21] K.S. Novoselov *el al. Science*, 306:666, 2004.

[22] O.J. Sofo, A.S. Chaudhari, and G.D. Barber. *Phys. Rev. B*, 75:153401, 2007.

[23] O. Leenaerts, B. Partoens, and F.M. Peeters. *Phys. Rev. B*, 80:245422, 2009.

[24] D.C. Elias *el al. Science*, 323:610, 2009.

[25] D.W. Boukhvalov, M.I. Katsnelson, and A.I. Lichtenstein. *Phys. Rev. B*, 77:035427, 2008.

[26] B. Eren *et al. Beilstein J. Nanotech.*, 3:852, 2013.

[27] B. Eren *et al. Appl. Phys. Lett.*, 102:071602, 2013.

[28] R. Hippler *et al. Low Temperature Plasma Physics.* Wiley-Verlag Berlin, Germany, 2001.

[29] E. Zaremba and W. Kohn. *Phys. Rev. B*, 15:1769, 1977.

[30] A. Zangwill. *Physics at Surfaces.* Cambridge Univ. Press Cambridge, 1988.

[31] M. Inokuti. *Int. J. Quantum Chem.*, 57:1996, 1996.

[32] International Commission on Radiation Units and Measurements. *ICRU Report No. 49.* Bethesda, USA, 1993.

[33] R. Behrisch. *Sputtering by Particle Bombardment.* Springer Verlag, Heidelberg, Germany, 1983.

[34] H. Bethe. *Ann. Physik*, 5:325, 1930.

[35] P. Sigmund. *Phys. Rev.*, 184:383, 1969.

[36] P. Sigmund. *J. Mater. Sci.*, 8:1545, 1973.

[37] W. Eckstein. *Computer simulation of ion-solid interaction, Springer Series in Material Science.* Springer Verlag, Berlin, Germany, 1991.

[38] W. Eckstein *et al. Sputtering data, Max-Planck- Institut für Plasmaphysik, Report IPP,* 9/82, 1993.

[39] G.F. Matthews. *J. Nucl. Mat.*, 337-339:1, 2005.

[40] Y. Yamamura and J. Bohdansky. *Vacuum*, 35:561, 1985.

[41] M. Küstner *et al. J. Roth, Nucl. Inst. Meth. B*, 145:320, 1998.

[42] M. Balden *et al. J. Nucl. Mater.*, 329-333:1515, 2004.

[43] Ch. Steinbruechel. *Journal of Vacuum Science and Technology A*, 3:1913, 1985.

[44] H. F. Winters. *Radiation Effects and Defects in Solids*, 64:79, 1982.

[45] T. Sugie *et al. J. Nuclear Mater.*, 329-333:1481, 2004.

[46] V.Kh. Alimov, J. Roth, and S. Lindig. *J. Nuclear Mater.*, 381:267, 2008.

[47] L. Shao *et al. Appl. Phys. Lett.*, 87:091902, 2005.

[48] F. Okba *et al. Appl. Phys. Lett.*, 97:031917, 2010.

[49] A.S. Kuznetsov *et al. J. Phys.: Condens. Matter.*, 24:052203, 2012.

[50] M. Born and E. Wolf. *Principles of Optics.* Cambridge Univ. Press Cambridge, UK, 1999.

[51] Martin Dressel and George Grüner. *Electrodynamics of solids: Optical properties of electrons in matter.* Cambridge Univ. Press Cambridge, UK, 2002.

[52] H.E. Bennett and J.O. Porteus. *J. Opt. Soc. Am.*, 51:123, 1961.

[53] S. Sinha *et al. J. Less-Common Met.*, 134:229, 1987.

[54] Y. Fukai. *The Metal-Hydrogen System / Basic Bulk Properties.* Springer-Verlag Berlin Heidelberg, Germany, 2005.

[55] Y. Wang *et al. ACS Nano*, 4:6146, 2010.

[56] Z. Luo *et al. J. Phys. Chem. C,*, 115:1422, 2011.

[57] A. Einstein. *Ann. Physik*, 322:132, 1905.

[58] C. Nordling, E. Sokolowski, and K. Siegbahn. *Phys. Rev.*, 105:1676, 1957.

[59] S. Hüfner. *Photoelectron Spectroscopy - Principles and Applications.* Springer-Verlag Berlin, Germany, 2002.

[60] H.Y. Fan. *Phys. Rev.*, 68:43, 1945.

[61] H. Mayer and H. Thomas. *Z. Physik*, 147:419, 1957.

[62] H. Puff. *Phys. Stat. Sol.*, 1:636, 1961.

[63] C.N. Berglund and W.E. Spicer. *Phys. Rev.*, 136:1030, 1964.

[64] C.S. Fadley. *Prog. in Surf. Sci.*, 16:275, 1984.

[65] C.S. Fadley. *J. Elect. Spec.Rel. Phen.*, 178-179:2, 2010.

[66] B. Feuerbacher, B. Fitton, and R. F. Willis. *Photoemission and the Electronic Properties of Surfaces.* John Wiley & Sons New York, USA, 1978.

[67] Himpsel *et al. Phys. Rev. B*, 38:6086, 1988.

[68] S. Doniach and M. Sunjic. *J. Phys. C: Solid State Phys.*, 3:285, 1970.

[69] A.D. Shirley. *Phys. Rev. B*, 5:4709, 1972.

[70] R. Hesse *et al. J. Anal. Chem.*, 365:48, 1999.

[71] J.H. Scofield. *J. Electron Spectrosc. Relat. Phenom.*, 8:129, 1976.

[72] G. Binnig, C.F. Quate, and C. Gerber. *Phys. Rev. Lett.*, 56:930, 1986.

[73] G. Meyer and N.M. Amer. *Appl. Phys. Lett.*, 53:1045, 1988.

[74] Y. Martin, C.C. Williams, and H.K. Wickramasinghe. *J. Appl. Phys.*, 61:4723, 1987.

[75] Q. Zhong *et al. Surf. Sci. Lett.*, 290:L688, 1993.

[76] S. W. Thomson (Lord Kelvin). *Philosophical Magazine Series 5*, 46:82, 1898.

[77] D.W. Abraham *et al. J. Vac. Sci. Technol. B*, 9:703, 1991.

[78] M. Nonnenmacher, M. P. O'Boyle, and H. K. Wickramasinghe. *Appl. Phys. Lett.*, 58:2921, 1991.

[79] A. Rothen. *Rev. Sci. Instrum.*, 16:26, 1945.

[80] R.M.A. Azzam and N.M. Bashara. *Ellipsometry and polarized light.* North-Holland Amsterdam, The Netherlands, 1986.

[81] T.E. Jenkins. *J. Phys. D: Appl. Phys.*, 32:R45, 1999.

[82] A. Röseler. *Infrared spectroscopic ellipsometry.* Akademie Verlag Berlin, Germany, 1990.

[83] W.R. Weidner, J.J. Hsia, and B. Adams. *Appl. Optics*, 24:2225, 1985.

[84] I. Langmuir and H. Mott-Smith. *Phys. Rev.*, 28:727, 1926.

[85] R.L. Merlino. *Am. J. Phys.*, 75:1078, 2007.

[86] M. von Laue. *Nobel Lectures, Physics*, 1914.

[87] W.L. Bragg. *Nature*, 90, 1912.

[88] W.L. Bragg. *Proc. Cambridge Phil.Soc.*, 17, 1913.

[89] G. Binnig and H. Rohrer. *IBM Journal of Research and Development*, 30:4, 1986.

[90] L. Reimer. *Scanning Electron Microscopy: Physics of Image Formation and Microanalysis.* Springer-Verlag Berlin, Germany, 2008.

[91] L.B. Valdes. *Proceed. of the IRE*, 42:420, 1954.

[92] R. Rymaszewski. *J. Sci. Instrum. (J. Phys. E)*, 2:170, 1969.

[93] K. Scherpinski *et al. International Symposium on Advanced Packaging Material*, page 178, 1999.

[94] W.R. Weidner, J.J. Hsia, , and B. Adams. *In: Hdb. der Radiologie, Vol. VI.*, 2:209, 1934.

[95] D.J. Gardiner. *Practical Raman spectroscopy.* Springer-Verlag Berlin, Germany, 1989.

[96] D-Z. Jin *et al. Vacuum*, 83:451, 2009.

[97] D. Gall *et al.* . *Vac. Sci. Technol. A*, 14:374, 1996.

[98] M. Wisse *et al. Rev. Sci. Instrum.*, 83:013509, 2012.

[99] A.F Bardamid *et al. Surf. Coatings. Technol.*, 1003-1004:365, 1998.

[100] D.V. Orlinski, V.S. Voitsenya, and K.Y. Vukolov. *Plasma Devices Ops.*, 15:33, 2007.

[101] I. Petrov *et al. J. Vac. Sci. Technol. A*, 21:S117, 2003.

[102] C.V. Thompson. *Annu. Rev. Mater. Sci.*, 20:245, 1990.

[103] G. Dirks and H.J. Leamy. *Thin Solid Films*, 47:219, 1977.

[104] J.A. Thornton. *Ann. Rev. Mater. Sci.*, 7:239, 1977.

[105] J.A. Thornton. *J. vac. Sci. Technol. A*, 4:3059, 1986.

[106] P.B. Barna and M. Adamik. *Thin Solid Films*, 317:27, 1998.

[107] G. De Temmerman et al. *J. Nucl. Mater.*, 337-339:956, 2005.

[108] P. Reinke and P. Oelhafen. *Diam. Relat. Mater.*, 8:15, 1999.

[109] J A. Thornton. *J. Vac. Sci. Technol.*, 11:666, 1974.

[110] J. E. Nestell, Jr. and R. W. Christy. *J. Vac. Sci. Technol.*, 15(2):366, 1978.

[111] G. W. Brindley and G. Brown. *Crystal Structures of Clay Minerals and their X-ray Identification*. Mineralogical Society, London, UK, 1980. p. 131.

[112] Joint Committee on Powder Diffraction Standards. Powder diffraction file, card no. 42-1120, 1953.

[113] L. Marot *et al. Thin Solid Films*, 516:7604, 2008.

[114] D.W. Hoffman. *Thin Solid Films*, 107:353, 1983.

[115] D.W. Hoffman. *J. Vac. Sci. Technol. A*, 12:953, 1994.

[116] Joint Committee on Powder Diffraction Standards. Powder diffraction file, card no. 05-0685, 1953.

[117] M. Joanny et al. *Rev. Sci. Instrum*, 81:10E108, 2010.

[118] J. Nagano. *Thin Solid Films*, 67:1, 1980.

[119] A.F. Mayadas, M. Shatzkes, and J.F. Janak. *Appl. Phys. Let.*, 14:345, 1969.

[120] S. Marsillac *et al. Phys. Stat. Sol. c*, 5:1244, 2008.

[121] J.D. Walker *et al. Appl.d Phys. Lett.*, 94:141908, 2009.

[122] W.D. Nix and B.M. Clemens. *J. Mater. Research*, 14:3467, 1999.

[123] X.H. Yana, J.W. Ding, and Q.B. Yang. *Eur. Phys. J. B*, 20:157, 2001.

[124] S.Gangopadhyay and A.K. Sen. *Phys. Rev. B*, 46:4020, 1992.

[125] V.S. Voitsenya *et al. J. Nucl. Mater.*, 290-293:336, 2001.

[126] J.F. Ziegler. Srim-2006 computer code, online: http://www.srim.org. 2006.

[127] T. Hoechbauer. On the mechanisms of hydrogen implantation induced silicon surface layer cleavage. *Ph.D. thesis Philipps-Universitaet Marburg*, 2001.

[128] R. Behrisch. *Sputtering by Particle Bombardment II*. Springer-Verlag Berlin, 1983.

[129] V. Kotov *et al. Fusion Eng. Des.*, 86:1583, 2011.

[130] W. Steinhoegl *et al. Phys. Rev. B*, 66:075414, 2002.

[131] J.M. Camacho and A.I. Oliva. *Thin Solid Films*, 515:1881, 2006.

[132] J. Torres *et al. Phys. Stat. Sol. (c)*, 10:3726, 2005.

[133] J-G. Choi and L.T. Thompson. *Appl. Surf. Sci.*, 93:143, 1996.

[134] E.V. Pettrovich *et al. Zh. Eksp. Teor. Fiz.*, 61:1756, 1971.

[135] E.V. Pettrovich *et al. Sov. Phys. JETP*, 34:935, 1972.

[136] M. Gupta and B. Schlapbach. *Hydrogen in Intermetallic Compounds I, ed. by B. Schlapbach, Topics Appl. Phys., Vol. 63*. Springer Verlag Berlin Heidelberg, Germany, 1988.

[137] Y.C. Lu and C.R. Clayton. *Corrosion Science*, 29:927, 1989.

[138] J.C. Green. *Ann. Rev. Phys. Chem.*, 28:161, 1977.

[139] P. Mikusik *et al. Chech. J. Phys. B*, 31:1165, 1981.

[140] S. Sinha *et al. J. Phys. F: Met. Phy.*, 16:L229, 1986.

[141] H. Hixson and P.M.A. Sherwood. *J. Chem. Soc. Faraday Trans.*, 91:3593, 1995.

[142] L. Marot *et al. Surf. Coat. Tech.*, 202:2837, 2008.

[143] Yu.R. Kolobov. *Grain Boundary Diffusion and Properties of Nanostructured Materials*. Cambridge Int. Publishing Cambridge, UK, 2007.

[144] I. Kaur, Y. Mishin, and W. Gust. *Fundamentals of Grain and Interphase Boundary Diffusion*. John Wiley & Sons New York, USA, 1995.

[145] J.M.E. Harper R.M. Bradley. *J. Vac. Sci. Technol. A*, 6:2390, 1988.

[146] U. Valbusa, C. Boragno, and F. Buatier de Mongeot. *J. Phys.: Condens. Matter*, 14:8153, 2002.

[147] S. Rusponi *et al. Appl. Phys. Lett.*, 75:3318, 1999.

[148] M.V.R Murty *et al. Phys. Rev. B*, 60:16956, 1999.

[149] S. Park *et al. Phys. Rev. Lett.*, 83:3486, 1999.

[150] Y. Kuramoto and T. Tsuzuki. *Prog. Theor. Phys.*, 55:356, 1977.

[151] G.I. Sivashinsky. *Acta Astronaut.*, 6:569, 1979.

[152] R. Cuerno and A.L. Barabási. *Phys. Rev. Lett.*, 74:4746, 1995.

[153] M. Castro *et al. Phys. Rev. Lett.*, 94:016102, 2005.

[154] W.L. Chan and E. Chason. *J. Appl. Phys.*, 101:121301, 2007.

[155] R.M. Bradley. *Phys. Rev. B*, 83:075404, 2011.

[156] S.-J. Kahng, B.-Y. Choi, and Y. Kuk. *Appl. Surf. Sci.*, 183:76, 2001.

[157] D. Nguyen-manh, V. Vitek, and A. Horsfield. *Prog. in Mater. Sci.*, 52:255, 2007.

[158] R. Behrisch *et al. J. Nucl. Mater.*, 313-6:388, 2003.

[159] J.N. Brooks and J.P. Allain. *Nucl. Fusion*, 48:045003, 2008.

[160] D.K. Kogut, N.N. Trifonov, and V.A. Kurnaev. *J. Nucl. Mat.*, 438:S731, 2013.

[161] T. Sugie *et al.* Energy distribution of he-flux on first mirror calculated by a. s. kukushkin. *11th ITPA Diagnostic Meeting, Sendai, Japan*, 2006.

[162] L. Marot *et al.* Plasma exposure of rhodium mirrors. *14th ITPA Diagnostic Meeting, Lausanne, Switzerland*, 2008.

[163] J.T. Yates, P.A. Thiel, and W.H. Weinberg. *Surf. Sci.*, 82:45, 1979.

[164] G.A. Mills and F.W. Steffgen. *Catal. Rev.*, 8:159, 1974.

[165] G. C. Bond. *Catalysis by Metals*. Academic, London, UK, 1962.

[166] O. Beeck. *Discuss. Faraday Soc.*, 8:118, 1950.

[167] C. Kemball. *Proc. R. Soc. Lond. A*, 214:413, 1952.

[168] J.R. Anderson and C. Kemball. *Proc. R. Soc. Lond. A*, 223:361, 1954.

[169] J.V. Mimeault and R.S. Hansen. *J. Chem. Phys.*, 45:2240, 1966.

[170] M.G. Wells, N.W. Cant, and R.G. Greenler. *Surf. Sci.*, 67:541, 1977.

[171] S.M. Edwards *et al. Surf. Sci.*, 72:213, 1978.

[172] D.G. Castner, B.A. Sexton, and G.A. Somorjai. *Surf. Sci.*, 71:519, 1978.

[173] K. Christmann *et al. Chem. Phys. Lett.*, 131:192, 1986.

[174] H. Conrad, W. Stenzel, and M.E. Kordesch. *Fifth Intern. Conf. on Vibration at Surfaces, Grainau Germany*, page 1, 1987.

[175] W. Nichtl *et al. Surf. Sci.*, 188:L635, 1987.

[176] E. Ehsasi and K. Christmann. *Surf. Sci.*, 194:172, 1988.

[177] W. Oed *et al. Solid State Phys.*, 21:237, 1988.

[178] K. Christmann. *Mol. Phys.*, 66:1, 1989.

[179] J.T. Yates, P.A. Thiel, and W.H. Weinberg. *Surf. Sci.*, 84:427, 1979.

[180] R. Duś, E. Nowicka, and R. Nowakowski. *Appl. Surf. Sci.*, 254:4286, 2008.

[181] R.B. McLellan and W.A. Oates. *Acta Metall.*, 21:181, 1973.

[182] M. Tkacz. *J. Chem. Phys.*, 108:2084, 1998.

[183] B. Li *et al. PNAS*, 108:18618, 2011.

[184] F.A. Lewis. *Pure & Appl. Chem.*, 62:2091, 1990.

[185] J.I. Avila *et al. J. Appl. Phys.*, 107:023504, 2010.

[186] A. Othonos, K. Kalli, and D.P. Tsai. *App. Sur. Sci.*, 161:54, 2000.

[187] V.E. Antonov *et al. Platinum Metals Rev.*, 28:158, 1984.

[188] E. Nowicka. *Vacuum*, 48:199, 1997.

[189] J. Koshy. *J. Phys. D: Appl. Phys.*, 13:1339, 1980.

[190] L. Marot *et al. Surf. Sci.*, 602:3375, 2008.

[191] Y. Abe *et al. Jpn. J. Appl. Phys.*, 39:245, 2000.

[192] *Handbook of Chemistry and Physics*. CRC Press, Cleveland, USA, 57 edition, 1976.

[193] M.G. Helander *et al. Appl. Surf. Sci.*, 255:9553, 2009.

[194] L. Marot *et al. Nanotechnology*, 21:365706, 2010.

[195] L. Marot *et al. Nanotechnology*, 21:365707, 2010.

[196] V.N. Smith *et al. Phys. Rev. B*, 110:3197, 1974.

[197] G.S. Tripathi, N.E. Brener, and J. Callaway. *Phys. Rev. B*, 38:10454, 1988.

[198] V.V. Bannikov, I.R. Shein, and A.L. Ivanovskii. *J. of Structural Chem.*, 51:956, 2010.

[199] G. Fortunato, A. Bearzotti, and C. Calibndo. *Sensors and Actuators*, 16:43, 1989.

[200] R.A. Pitts *et al.* A full tungsten divertor for iter: physics issues and design status. *20th PSI conference, Aachen Germany*, 2012.

[201] L. Marot *et al. Fus. Eng. Des.*, "Accepted, 2013.

[202] M. Reinelt *et al. New J. Phys.*, 11:053023, 2009.

[203] M. Joanny *et al. IEEE Trans. Plasma Sci.*, 40:692, 2012.

[204] A. Litnovsky *et al. Fus. Eng. & Design*, 86:1780, 2011.

[205] Ch. Linsmeier and J. Wanne. *Surf. Sci.*, 454-456:305, 2000.

[206] Ch. Linsmeier, M. Reinelt, and K. Schmid. *J. Nucl. Mater.*, 415:S212, 2011.

[207] G. De Temmerman *et al. J. Appl. Phys.*, 102:083302, 2007.

[208] L. Marot *et al.* Performances of rh and mo mirrors under jet exposure. *20th PSI conference, Aachen Germany*, 2012.

[209] M.E. Day, M. Delfino, and S. Salimian. *J. Appl. Phys.*, 72:5467, 1992.

[210] L. Moser. Development of a concept design for a plasma sputtering cleaning system for ITER fiagnostic first mirrors. Master's thesis, University of Basel, 2013.

[211] M. Wisse *et al. Fusion Eng. Des.*, Accepted, doi:10.1016/j.fusengdes.2013.03.077, 2013.

[212] R. Abermann. *Vacuum*, 41:1279, 1990.

[213] R. Koch. *J. Phys.: Candens. Matter*, 6:9519, 1994.

[214] R.W. Hoffman. *Thin Solid FIlms*, 34:185, 1976.

[215] W.D. Nix and B.M. Clemens. *J. Mater. Res.*, 14:3467, 1999.

[216] S.C. Seel *et al. J. Appl. Phys.*, 88:7079, 2000.

[217] L.B. Freund and E. Chason. *J. Appl. Phys.*, 89:4866, 2001.

[218] F. Spaepen. *Acta. Mater.*, 48:31, 2000.

[219] R.C. Cammarata, T. M. Trimble, and D.J. Srolovitz. *J. Mater. Res.*, 15:2468, 2000.

[220] E. Chason *et al. Phys. Rev. Lett.*, 88:156103, 2002.

[221] C. Friesen and C.V. Thompson. *Phys. Rev. Lett.*, 93:056104, 2004.

[222] R. Koch, D. Hu, and A.K. Das. *Phys. Rev. Lett.*, 94:146101, 2005.

[223] J. Leib and C.V. Thompson. *Phys. Rev. B*, 82:121402, 2010.

[224] J.A. Thornton and D.W. Hoffman. *J. Vac. Sci. Tech. A*, 3:576, 1985.

[225] J.W. Hutchinson, M.D. Thouless, and E.G. Liniger. *Acta Metall. Mater.*, 40:295, 1992.

[226] E.A. Jagla. *Phys. Rev. B*, 75:085405, 2007.

[227] J. Colin, C. Coupeau, and J. Grilhé. *Phys. Rev. Lett.*, 99:046101, 2007.

[228] B. Audoly. *Phys. Rev. Lett.*, 83:4124, 1999.

[229] P. Peyla. *Phys. Rev. E*, 62:R1501, 2000.

[230] P. Goudeau *et al. Appl. Phys. Lett.*, 83:51, 2003.

[231] J. Colin *et al. European Phys. Lett.*, 86:54002, 2009.

[232] A.Y. Usenko and A.G. Ulyashin. *Japan. J. Appl. Phys.*, 41:5021, 2002.

[233] P. Chen *et al. Appl. Phys. Lett.*, 86:031904, 2005.

[234] Y. Ma *et al. Appl. Phys. Lett.*, 86:252109, 2005.

[235] W.C. Oliver and G.M. Pharr. *J. Mater. Res.*, 7:1564, 1992.

[236] V. Hauk. *Structural and Residual Stress Analysis by Non-destructive Methods: Evaluation, Application, Assessment.* Elsevier, Amsterdam, The Netherlands, 1997.

[237] D. Faurie *et al. Act. Mater.*, 58:4998, 2010.

[238] B. Hammer and J.K. Norskov. *Nature*, 276:238, 1995.

[239] M.K. Small and W.D. Nix. *J. Mater. Res.*, 7:1553, 1992.

[240] W. Sauter. Thin film mechanics bulging and streching. *Ph.D. thesis University of Vermont*, 2000.

[241] N.N. Nikitenkov *et al. J. Surf. Invesig. X-ray, Synchro.*, 4:534, 2010.

[242] R. Hull. *Properties of crystalline silicon.* The Institution of Electrical Engineers London, UK, 1999.

[243] D.F. Johnson and E.A. Carter. *J. Mater. Res.*, 25:315, 2010.

[244] M. Bruel. *Nucl. Instrum. Methods Phys. Res. B*, 108:313, 1996.

[245] A.K. Singh and B. I. Yakobson. *Nano Letters*, 9:1540, 2009.

[246] Y.G. Zhou *el al. J. Appl. Phys.*, 105:014309, 2009.

[247] J. Bohdansky, J. Roth, and H.L. Bay. *J. Appl. Phys.*, 51:2861, 1980.

[248] A.C. Dillon *et al. Nature*, 386:377, 1997.

[249] A. Züttel *et al. Int. J. Hydrogen Energy*, 27:203, 2002.

[250] F.L. Darkrim, P. Malbrunot, and G.P. Tartaglia. *Int. J. Hydrogen Energy*, 27:193, 2002.

[251] T. Yildirim, O. Gulseren, and S. Ciraci. *Phys. Rev. B*, 64:075404, 2001.

[252] B.N. Khare *et al. Nano Letters*, 2:73, 2002.

[253] P. Ruffieux *et al. Phys. Rev. B*, 66:245416, 2002.

[254] D. Neumann *et al. App. Phys. A*, 55:489, 1992.

[255] A. Nikitin *et al. Phys. Rev. Lett.*, 95:225507, 2006.

[256] L. Hornekær *et al. Phys. Rev. Lett.*, 96:156104, 2006.

[257] M. Wojtaszek *et al. J. Appl. Phys.*, 110:063715, 2011.

[258] B. Rousseau *et al. Appl. Phys. A*, 77:591, 2003.

[259] R. Yang *et al. Adv. Mater.*, 22:4014, 2010.

[260] M. Allen *et al. Adv. Mater.*, 21:2098, 2009.

[261] F. Tuinstra and J.L. Koenig. *J. of Chem. Phys.*, 53:1126, 1970.

[262] A.C. Ferrari and J. Robertson. *Phys. Rev. B*, 61:14095, 2000.

[263] A.C. Ferrari *et al. Phys. Rev. Lett.*, 97:187401, 2006.

[264] A.C. Ferrari. *Solid State Com.*, 143:47, 2007.

[265] M. Neek-Amal and F.M. Peeters. *Phys. Rev. B*, 83:235437, 2011.

[266] J. Jones *et al. Carbon*, 48:2335, 2010.

[267] Y. Zhang *et al. ACS Nano*, 6:126, 2012.

[268] C. Herrero *et al. J. Phys. D: Appl. Phys.*, 43:255402, 2010.

[269] Z. Waqar. *J. Mater. Sci.*, 42:1169, 2007.

[270] D. Ugolini, J. Eitle, and P. Oelhafen. *Appl. Phys. A*, 54:57, 1992.

[271] J.C. Lascovich, V. Rosato, and A. Santoni. *Surf. Sci.*, 467:139, 2000.

[272] A. Allouche and Y. Ferro. *Phys. Rev B.*, 74:235426, 2006.

[273] T. Takahashi, H. Tokailin, and T. Sagawa. *Phys. Rev. B*, 32:8317, 1985.

[274] L. Diederich *et al. Surf. Sci.*, 349:176, 1996.

[275] I. Batra *et al. Surf. Sci.*, 181:126, 1987.

[276] Y. Kobayashi *et al. Phys. Rev. B*, 71:193406, 2005.

[277] P. Ruffieux *et al. Phys. Rev. B*, 71:153403, 2005.

[278] Y. Niimi *et al. Phys. Rev. B*, 73:085421, 2006.

[279] R. Décker *et al. Nano Lett.*, 11:2291, 2011.

[280] S.L. Wong *et al. MRS Bulletin*, 37:1195, 2012.

[281] M. Klintenberg *et al. Phys. Rev. B*, 81:085433, 2010.

[282] H. Şahin, C. Ataca, and S. Ciraci. *Phys. Rev. B*, 81:205417, 2010.

[283] O. Leenaerts *et al.* *Phys. Rev. B*, 82:195436, 2010.

[284] B. Gharekhanlou and S. Khorasani. *IEEE T. Electron. Dev.*, 57:209, 2010.

[285] X. Li *et al.* *Science*, 324:1312, 2009.

[286] W. Fu *et al.* *Nano Letters*, 11:3597, 2011.

[287] A. Das *et al.* *Nature Nanotech.*, 3:210, 2008.

[288] X. Peng, F. Tang, and A. Copple. *J. Phys.: Condens. Matter*, 24:075501, 2012.

[289] A. Kikukawa, S. Hosaka, and R. Imura. *Rev. Sci. Instrum.*, 67:1463, 1996.

[290] Ch. Sommerhalter *et al.* *Appl. Phys. Lett.*, 75:286, 1999.

[291] S. Sadewasser *et al.* *Appl. Phys. Lett.*, 80:2979, 2002.

[292] D. Ziegler *et al.* *Phys. Rev. B*, 83:235434, 2011.

[293] H. E. Romero *et al.* *ACS Nano*, 2:2037, 2008.

[294] Y.-J. Yu *et al.* *Nano letters*, 9:3430, 2009.

[295] G. Elias *et al.* *Beilstein J. Nanotech.*, 2:252, 2011.

[296] R. H. Miwa et al. *Appl. Phys. Lett.*, 99:163108, 2011.

List of Symbols and Abbreviations

Symbols

A_0: Oscillation amplitude when $f=f_{1^{st}}$
A_{osc}: Free oscillation amplitude
A_{sp}: Set point amplitude
c: Chord length of blisters
D: Surface diffusion contast
$dE/d\Omega$: Photoelectron cross section
E: Energy
E: Young's modulus
E_f: Fermi level
E_r: Reduced Young's modulus
ϵ: Complex permittivity / dielectric constant
ϵ_i: Ion impact energy
f: Caltilever resonance frequency
$f_{n^{th}}$: n^{th} cantilever resonance frequency
Φ: Phase (AFM)
ϕ: Angle of incidence
h: Interface separation of a blister
$h\nu$: Photon energy
I: Intensity
Λ_e: Inelastic mean free path
λ: Wavelength
ν: Surface tension coefficient
R: Reflectivity (at $0°$, unless otherwise stated)
R_p: Parallel component of R
R_s: Perpendicular component of R
$R_\square$: Electrical sheet resistance
$\check{R}$: Relative reflectivity
$\mathfrak{R}$: Grain/crystallite boundary reflection
ρ: Specific electrical resistivity
ρ_{ref}: Complex reflectance ratio
r_a: Average roughness
r_{rms}: Root mean square roughness
S(E): Stopping power
σ: Uniform biaxial stress
σ_c: Critical stress for buckling

T: Temperature
T_e: Electron temperature
T_i: Ion temperature
t: Film thickness
τ_D: Intraband relaxation time
V_f: Fermi velocity
v: Velocity
θ: Glancing (grazing) angle (90-ϕ)
Ω_E: Spectrometer acceptance angle
ω: Angular frequency
z: Distance to surface normal

Elements and other materials

Al: Aluminum
Au: Gold
Be: Beryllium
C: Carbon
D: Deuterium
H: Protium
HOPG: Highly oriented pyrolytic graphite
Mg: Magnesium
Mo: Molybdenum
O: Oxygen
PTFE: Polytetrafluoroethylene
Pt/Ir: Platinum iridium alloy
Rh: Rhodium
SS316L: Stainless steel 316L
W: Tungsten

Methods

AFM: Atomic force microscopy
KPFM: Kelvin probe force microscopy
SEM: Scanning electron microscopy

M

STM: Scanning tunneling microscopy
STS: Scanning tunneling spectroscopy
UPS: Ultraviolet photoelectron spectroscopy
XPS: X-ray photoelectron spectroscopy
XRD: X-ray diffrectometry

HV: High vacuum
LTP: Low temperature plasma
RF: Radio frequency
RT: Room temperature
UV/VIS/NIR: Ultraviolet/visible/near-infrared
UHV: Ultra-high vacuum
WF: Work function

Units

°: Degrees
°C: Degrees Celcius
Å: Ångströms
eV: Electron volts
Hz: Hertz
K: Kelvin
N: Newtons
Pa: Pascal
g: Grams
h: Hours
m: Meters
min, ': Minutes
s: Seconds
V: Volts
W: Watts
Ω: Ohms

Fusion reactors

JET: Joint European Torus in Culham, England
ITER: World's largest tokamak project in Cadarache, France
TEXTOR: Tokamak Experiment for Technology-Oriented Research in Jülich, Germany

Others

bcc: Body centered cubic
B.E.: Binding energy
DOS: Density of states
EM: Electromagnetic
fcc: Face centered cubic
FMs: First mirrors

Acknowledgements

List of Publications and Communications

Peer-reviewed Journal Publications

- L. Moser, **B. Eren**, M. Wisse, R. Steiner, D. Mathys, R. Reichle, F. Leipold, L. Marot, and E. Meyer. Towards plasma cleaning of ITER first mirrors. in preparation, 2013.

- G. Fessler, **B. Eren**, U. Gysin, Th. Glatzel, and E. Meyer. Friction force microscopy studies of pristine and hydrogenated graphene on SiO_2. in preparation, 2013.

- **B. Eren**, L. Marot, G. Günzburger, P.-O. Renault, Th. Glatzel, R. Steiner, and E. Meyer. Hydrogen induced buckling of gold films. submitted for publication, 2013.

- **B. Eren**, L. Marot, I.V. Ryzhkov, S. Lindig, A. Houben, M. Wisse, O.O. Skoryk, M. Oberkofler, V.S. Voitsenya, C. Linsmeier, and E. Meyer. Roughening and reflection performance of molybdenum coatings exposed to high flux deuterium plasma. *Nuclear Fusion*, 53:113013, 2013.

- M. Wisse, L. Marot, **B. Eren**, R. Steiner, D. Mathys, and E. Meyer. Laser damage thresholds of ITER mirror materials and first results on in situ laser cleaning of stainless steel mirrors. *Fusion Engineering and Design*, 88:388, 2013.

- L. Marot, Ch. Linsmeier, **B. Eren**, L. Moser, R. Steiner, and E. Meyer. Can aluminum or magnesium be a surrogate for beryllium: A critical investigation of their chemistry. *Fusion Engineering and Design*, 88:1718, 2013.

- **B. Eren**, Th. Glatzel, M. Kisiel, W. Fu, R. Pawlak, U. Gysin, C. Nef, L. Marot, M. Calame, Ch. Schönenberger, and E. Meyer. Hydrogen plasma microlithography of graphene supported on Si/SiO_2 substrate. *Applied Physics Letters*, 102:071602, 2013.

- **B. Eren**, L. Marot, M. Wisse, D. Mathys, M. Joanny, J-M. Travère, R. Steiner, and E. Meyer. In situ evaluation of the reflectivity of molybdenum and rhodium coatings in an ITER-like mixed environment. *Journal of Nuclear Materials*, 438:S852, 2013.

- **B. Eren**, M. Wisse, L. Marot, R. Steiner, and E. Meyer. Deuterium plasma exposure on rhodium: Reflectivity monitoring and evidence of subsurface deuteride formation. *Applied Surface Science*, 273:94, 2013.

- **B. Eren**, D. Hug, L. Marot, R. Pawlak, M. Kisiel, R. Steiner, D. M. Zumbühl, and E. Meyer Pure Hydrogen Low Temperature Plasma Exposure of HOPG: Graphane Formation? *Beilstein Journal of Nanotechnology*, 3:851, 2013.

- M. Wisse, **B. Eren**, L. Marot, R. Steiner, and E. Meyer. Spectroscopic reflectometry of mirror surfaces during plasma exposure. *Review of Scientific Instruments*, 83:013509, 2012.

- **B. Eren**, L. Marot, M. Langer, R. Steiner, M. Wisse, D. Mathys, and E. Meyer. The effect of low temperature deuterium plasma on molybdenum reflectivity. *Nuclear Fusion*, 51:103025, 2011.

- **B. Eren**, L. Marot, A. Litnovsky, M. Matveeva, R. Steiner, V. Emberger, M. Wisse, D. Mathys, G. Covarel, and E. Meyer. Reflective metallic coatings for first mirrors on ITER. *Fusion Engineering and Design*, 86:2593, 2011.

Scientific Communications

Due to the excess number, the list is limited to the presentations, in which B. Eren is either the presenter or the corresponding person.

- **B. Eren**, L. Marot, G. Günzburger et al. Hydrogen induced buckling of gold films, 1-5 July 2013 Poitiers France.

- **B. Eren**, M. Kisiel, R. Pawlak et al. Characterizations of HOPG and graphene treated with low temperature hydrogen plasma. Materials Research Society Spring Meeting, 1-5 April 2013 San Francisco USA.

- **B. Eren**, L. Marot, M. Wisse et al. Changes in the electronic structure of deuterium implanted molybdenum and rhodium. German Physical Society Annual Meeting, 10-15 March 2013 Regensburg Germany.

- **B. Eren**, M. Kisiel, Th. Glatzel et al. Kelvin probe force microscopy on graphene and HOPG hydrogenated with spatial periodicity with low temperature hydrogen plasma. Advanced atomic force microscopy techniques, 4-5 March 2013, Karlsruhe Germany.

- **B. Eren**, D. Hug, L. Marot et al. Graphane formation by pure hydrogen low temperature plasma exposure. Swiss Physical Society Annual Meeting, 21-22 June 2012 Zurich Switzerland.

- **B. Eren**, L. Marot, M. Wisse et al. In situ reflectance performance of molybdenum and rhodium in an ITER-like mixed environment. 20th International Conference on Plasma Surface Interactions, 21-25 May 2012 Aachen Germany.

- **B. Eren**, L. Marot, M.Wisse et al. Degradation of optical constants of metallic mirrors upon deuterium plasma exposures. 20th Meeting of the ITPA Topical Group on Diagnostics, 26-26 May 2011, Noordwijk aan See The Netherlands.

- **B. Eren**, L. Marot, M. Langer et al. The effect of low temperature deuterium plasma on molybdenum reflectivity. Swiss Physical Society Annual Meeting, 15-17 June 2011 Lausanne Switzerland.

- **B. Eren**, L. Marot, M. Langer et al. The effect of low temperature deuterium plasma on molybdenum reflectivity. 13th International workshop on plasma-facing materials and components for fusion applications / 1st International Conference on Fusion Energy Materials Science, 9-13 May 2011 Rosenheim Germany.

- **B. Eren**, L. Marot, A. Litnovsky et al. Reflective metallic coatings for first mirrors in ITER, 26th Symposium on Fusion Technology. 27 September - 1 October, Porto Portugal.

- **B. Eren**, L. Marot, R. Steiner, and E. Meyer. Deposition and characterization of first mirror candidates for ITER. Swiss Physical Society Annual Meeting, 21-22 June 2010 Basel Switzerland.

Curriculum Vitae

12. April 1985	Born in Bursa (Rep. of Turkey), Son of Ercan and Nüket Eren.
1991-1996	Primary school in Bursa and Istanbul (Rep. of Turkey).
1996-2000	Junior high school, American Robert College in Istanbul.
1990-2003	High school, American Robert College in Istanbul.
2003-2007	B.Sc. in Mechanical Engineering, Bosphorus University in Istanbul.
2007-2009	M.Sc. in Micro and Nanosystems, ETH Zurich in Zurich. Group of Prof. Dr. Heinz Jäckel
2009-2013	Ph.D. thesis in Physics, University of Basel in Basel. Group of Prof. Dr. Ernst Meyer Examination committee: Dr. Laurent Marot (thesis advisor) Prof. Dr. Martino Poggio (co-referee) Prof. Dr. Ernst Meyer (faculty representative) Dr. Gregory de Temmerman (expert) Prof. Dr. Christian Linsmeier (expert)